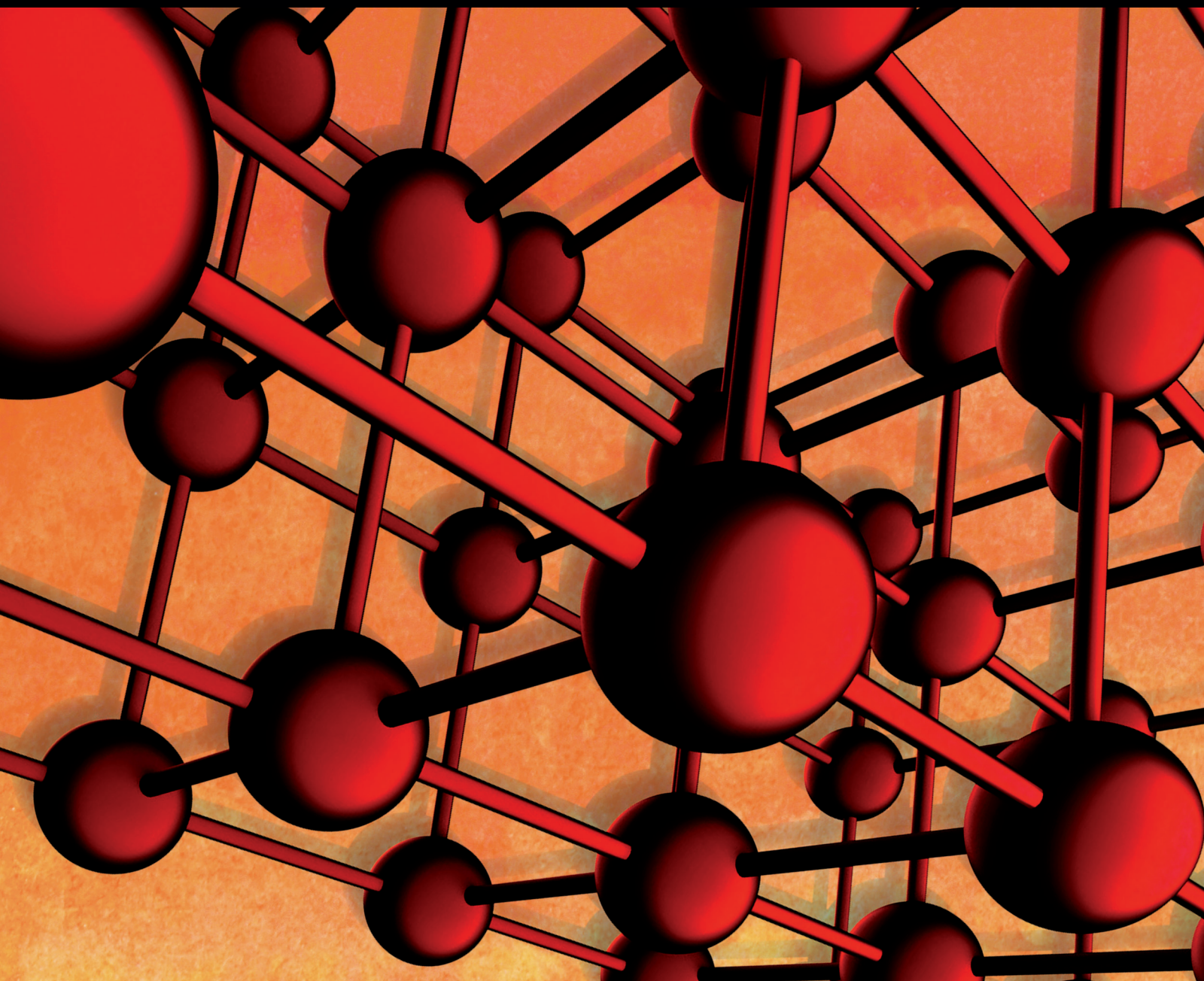


Advances in Materials Science and Engineering

Biomass-Based Materials and Technologies for Energy

Guest Editors: Jingxin Wang, Xinfeng Xie, David B. DeVallance, Jianchun Jiang, Lixin Huang, and Levente Dénes





Biomass-Based Materials and Technologies for Energy

Advances in Materials Science and Engineering

Biomass-Based Materials and Technologies for Energy

Guest Editors: Jingxin Wang, Xinfeng Xie,
David B. DeVallance, Jianchun Jiang, Lixin Huang,
and Levente Dénes



Copyright © 2015 Hindawi Publishing Corporation. All rights reserved.

This is a special issue published in “Advances in Materials Science and Engineering.” All articles are open access articles distributed under the Creative Commons Attribution License, which permits unrestricted use, distribution, and reproduction in any medium, provided the original work is properly cited.

Editorial Board

Dimitrios G. Aggelis, Belgium
Jarir Aktaa, Germany
K. G. Anthymidis, Greece
Amit Bandyopadhyay, USA
Arun Bansil, USA
Massimiliano Barletta, Italy
Jozef Bednarcik, Germany
Avi Bendavid, Australia
Jamal Berakdar, Germany
Giovanni Berselli, Italy
Alessandra Bianco, Italy
Susmita Bose, USA
Heinz-Günter Brokmeier, Germany
Steve Bull, UK
Peter Chang, Canada
Daolun Chen, Canada
Gabriel Cuello, France
Narendra B. Dahotre, USA
João P. Davim, Portugal
Francesco Delogu, Italy
Seshu B. Desu, USA
Yong Ding, USA
Aziz Dinia, France
Kaveh Edalati, Japan
Gilbert Fantozzi, France
Massimo Fresta, Italy
Eric Freysz, France
Sergi Gallego, Spain
Santiago Garcia-Granda, Spain
Filippo Giannazzo, Italy
Daniel Guay, Canada
Hiroki Habazaki, Japan
Joke Hadermann, Belgium
Satoshi Horikoshi, Japan
Rui Huang, USA

Jacques Huot, Canada
Michele Iafisco, Italy
Katsuyuki Kida, Japan
Jae-Ho Kim, Korea
Akihiko Kimura, Japan
Takayuki Kitamura, Japan
Hongchao Kou, China
Prashant Kumta, USA
Luciano Lamberti, Italy
Heinrich Lang, Germany
Pavel Lejcek, Czech Republic
Cristina Leonelli, Italy
Markku Leskela, Finland
Ying Li, USA
Wei Liu, France
Yunqi Liu, China
Meilin Liu, Georgia
Ying Liu, USA
Jun Liu, China
Fernando Lusquiños, Spain
Peter Majewski, Australia
Philippe Miele, France
Hossein Moayedi, Malaysia
Paul Munroe, Australia
Rufino M. Navarro, Spain
Luigi Nicolais, Italy
Hiroshi Noguchi, Japan
Chérif Nouar, France
José L. Ocaña, Spain
Tsutomu Ohzuku, Japan
Olanrewaju Ojo, Canada
Xiaoqing Pan, USA
Anna Paradowska, Australia
Gianluca Percoco, Italy
Jean-Francois Pierson, France

Simon C. Potter, Canada
Manijeh Razeghi, USA
Anna Richelli, Italy
Antonio Riveiro, Spain
Pascal Roussel, France
Timo Sajavaara, Finland
Antti Salminen, Finland
F.H. Samuel, Canada
Carlo Santulli, Italy
Franz-Josef Schmitt, Germany
Jainagesh A. Sekhar, USA
Fridon Shubitidze, USA
Charles C. Sorrell, Australia
Costas M. Soukoulis, USA
Sam-Shajing Sun, USA
Kohji Tashiro, Japan
Somchai Thongtem, Thailand
Achim Trampert, Germany
Filip Tuomisto, Finland
Stuart Turner, Belgium
Krystyn Van Vliet, USA
Rui Vilar, Portugal
Rui Wang, China
Qiang Wang, China
Rong Wang, USA
Lu Wei, China
Jörg M. K. Wiezorek, USA
Wei Wu, USA
Hemmige S. Yathirajan, India
Wenbin Yi, China
Belal F. Yousif, Australia
Jinghuai Zhang, China
Li Zhang, China
Ming-Xing Zhang, Australia
Wei Zhou, China

Contents

Biomass-Based Materials and Technologies for Energy, Jingxin Wang, Xinfeng Xie, David B. DeVallance, Jianchun Jiang, Lixin Huang, and Levente Dénes
Volume 2015, Article ID 393619, 2 pages

Texture Feature Extraction and Classification of SEM Images of Wheat Straw/Polypropylene Composites in Accelerated Aging Test, Huan Zhang, Chunxia He, Min Yu, and Jingjing Fu
Volume 2015, Article ID 397845, 10 pages

Mechanic and Acoustic Properties of the Sound-Absorbing Material Made from Natural Fiber and Polyester, Limin Peng, Boqi Song, Junfeng Wang, and Dong Wang
Volume 2015, Article ID 274913, 5 pages

Reduced-Pressure Boiling Extraction of Oleuropein Coupled with Ultrasonication from Olive Leaves (*Olea europaea* L.), Pu-jun Xie, Li-xin Huang, Cai-hong Zhang, Feng You, Cheng-zhang Wang, and Hao Zhou
Volume 2015, Article ID 719485, 8 pages

Microwave Assisted Hydrolysis of Holocellulose Catalyzed with Sulfonated Char Derived from Lignin-Rich Residue, Kui Wang, Xinfeng Xie, Zhan Si, Jianchun Jiang, and Jingxin Wang
Volume 2015, Article ID 106137, 5 pages

Effect of Heating at Oven-Dry State on Steam Treated Bamboo Powder Thermal Fluidity, S. Kajikawa and T. Iizuka
Volume 2015, Article ID 579659, 7 pages

Effects of Screen Size on Biochemical Conversion of Big Bluestem Biomass for Biofuel Production, Xiaoxu Song, Meng Zhang, Ke Zhang, Z. J. Pei, and Donghai Wang
Volume 2015, Article ID 947350, 9 pages

Editorial

Biomass-Based Materials and Technologies for Energy

**Jingxin Wang,¹ Xinfeng Xie,¹ David B. DeVallance,¹ Jianchun Jiang,²
Lixin Huang,² and Levente Dénes³**

¹*Division of Forestry and Natural Resources, West Virginia University, Morgantown, WV 26505, USA*

²*Institute of Chemical Industry of Forest Products, Chinese Academy of Forestry, Nanjing 210042, China*

³*Institute of Product Design and Manufacturing Technologies, University of West Hungary, Bajcsy-Zsilinszky Utca 4, Sopron 9400, Hungary*

Correspondence should be addressed to Jingxin Wang; jxwang@wvu.edu

Received 17 August 2015; Accepted 17 August 2015

Copyright © 2015 Jingxin Wang et al. This is an open access article distributed under the Creative Commons Attribution License, which permits unrestricted use, distribution, and reproduction in any medium, provided the original work is properly cited.

With the development of global industrialization, the world is facing an energy uncertainty and increasing environmental concerns resulting from fossil energy use. Biomass-based materials are known to have lower greenhouse gas emissions than those from nonrenewable resources, such as petroleum and coal. In recent years, biomass-based materials and technologies have become one of the most important components of sustainable systems due to biomass abundance and renewability. Biomass-based materials and technologies have drawn much attention from governments, academia, and industry, having become one of the most active research fields.

This special issue included some of the best contributions from the researchers in the field. Through a thorough and professional process, the best manuscripts were selected for publication in this special issue. The papers in this special issue present the state-of-the-art perspective on the wide spectrum of biomass-based materials and technologies ranging from high value chemicals extraction, materials handling, and chemical conversion to biomass-based composites for various engineering applications.

Understanding and improving the biomass material properties for hot molding processes are critical for effective utilization of biomass for composites. The article by S. Kajikawa and T. Iizuka found that steam or short-time dry heat treatments could improve the fluidity of bamboo particles. The study by L. Peng et al. showed a great potential of wood fiber for manufacturing high quality composites for acoustic applications. The article entitled “Texture Feature

Extraction and Classification of SEM Images of Wheat Straw/Polypropylene Composites in Accelerated Aging Test” enlightens the readers with a novel and effective approach of combining image analysis and artificial intelligence to classify the aging status of biomass fiber/polymer composites.

Biomass is also a cost-effective resource for high value chemicals with pharmacological properties. By combining reduced pressure and ultrasonication, the study by P. Xie et al. made an impressive progress on effectively extracting oleuropein from olive leaves. The method not only reduced the energy consumption for extracting chemicals but also achieved higher yield than traditional methods.

In addition to applications in materials and chemicals, biomass feedstocks play an important role in energy applications. The study by X. Song et al. revealed that larger particle sizes of biomass could be more beneficial in terms of saving milling energy and obtaining higher cellulose recovery and total sugar yield. The article entitled “Microwave Assisted Hydrolysis of Holocellulose Catalyzed with Sulfonated Char Derived from Lignin-Rich Residue” by K. Wang et al. introduced an efficient method (83% w.t. conversion within 60 minutes) to break the carbohydrate polymer in woody biomass using the lignin-derived char as the catalyst.

Acknowledgments

We thank the authors for their original contributions and the reviewers for the insightful suggestions which have helped ensure the quality of the papers. We hope this special

issue will stimulate the continuing efforts on research and technology development of biomass-based materials and technologies for energy-related applications.

Jingxin Wang
Xinfeng Xie
David B. DeVallance
Jianchun Jiang
Lixin Huang
Levente Dénes

Research Article

Texture Feature Extraction and Classification of SEM Images of Wheat Straw/Polypropylene Composites in Accelerated Aging Test

Huan Zhang,^{1,2,3} Chunxia He,¹ Min Yu,¹ and Jingjing Fu¹

¹College of Engineering, Jiangsu Key Laboratory for Intelligent Agricultural Equipment, Nanjing Agricultural University, Nanjing 210031, China

²College of Mechanical and Electronic Engineering, Qingdao Agricultural University, Qingdao 266109, China

³Jiangsu Key Laboratory of Large Engineering Equipment Detection and Control, Xuzhou Institute of Technology, Xuzhou 221111, China

Correspondence should be addressed to Chunxia He; chunxiahe@tom.com

Received 24 September 2014; Revised 17 April 2015; Accepted 20 April 2015

Academic Editor: Xinfeng Xie

Copyright © 2015 Huan Zhang et al. This is an open access article distributed under the Creative Commons Attribution License, which permits unrestricted use, distribution, and reproduction in any medium, provided the original work is properly cited.

Wheat straw/polypropylene composites are green recycled and biomass-based material. After accelerated aging test of the composite was done, practical and effective methods for characterization and extraction of texture feature of microscopic Scanning Electron Microscopy (SEM) images of composites were investigated in this paper, and involved data compression and classification recognition were studied as well. Through Angle Measure Technique (AMT) method, the complexity spectra, MA spectra, of the preprocessed SEM images of the composites were derived and then the first four principal components of MA spectra using Principal Component Analysis (PCA) were extracted accordingly. Two kinds of classifiers based on Extreme Learning Machine (ELM) and Support Vector Machine (SVM) were introduced to classify the SEM images into five different aging periods in this paper. The research results indicate that AMT method is a very novel and effective approach in texture feature characterization and analysis of SEM images of composites and high classification accuracy of SEM images in different aging periods by using intelligent recognition can be reached.

1. Introduction

Wheat straw/polypropylene composites are a new biomass-based material substituting for the traditional wood/plastics composites (WPCs) in many fields, which can be prepared by using plastic or rubber as matrix and wheat straw plant fiber, a usual agricultural residue, as filler. Compared with the crude wood, these kinds of wood/plastics composites have many advantages, such as better water resistance and anti-corrosive property. Although the composites are green, recycled, environmentally friendly material, they would exhibit aging phenomenon unavoidably [1–3]. If the microscopic SEM images of composites are effectively characterized and correctly classified in different aging periods, it is easy to accurately identify the aging stage of the material and to determine the dynamic development of its aging process.

The topics of quantitative characterization and intelligent modeling of microscopic surface topography and internal structure of composite material have been of great importance in recent years; for example, digital image processing of SEM was proposed to study relationship between cracks shape and wearing loss in the preparation of carbon fabric-epoxy composite [4]; SEM image processing and analysis was introduced in structural characteristics analysis of anodic porous alumina [5]; SEM microstructure characterization and modeling were researched on the numerical study on internal frost damage of digital cement paste samples with cohesive zone; and so forth [6].

Angle Measure Technique (AMT) method, first proposed by Andrlé in 1994, was used for quantitative characterization of curve complexity of geomorphic line [7]. This technique can be considered as a characterization tool of

TABLE 1: Raw materials of the experiment.

Main raw material	Trade name	Origin or manufacturer
Polypropylene (film)	—	Jiangyin Oriental Plastic Packaging Co., Ltd., China
Wheat straw	—	Tanghuang, Jiangyin, Jiangsu, China
Silane coupling agent	KH550	Shanghai Yaohua Glass Co., Ltd., China
Zinc stearate	Industrial grade	Shanghai Yan'an Grease Chemical Plant, China

signal complexity through scale domain transform and then was improved and introduced into many fields by some researcher. For instance, Huang and Esbensen used AMT and multivariate data analysis to characterize many types of powders, such as sand, pellet, and rapeseed [8]. Indahl and Næs characterized and built modeling of different sizes of oil droplets in mayonnaise by using AMT and PCR [9]. Kucheryavski investigated discrimination and classification of medical images by PLS-discrimination analysis after using AMT and wavelet transformation to construct feature vectors [10]. Fongaro and Kvaal studied surface texture characterization and multivariate feature extraction of texture images of Italian pasta by means of Heterogeneity (HTG), gray level cooccurrence matrix (GLCM), AMT, and so forth [11].

In the accelerated aging test, SEM images of the composites in 5 different aging periods were shot, and then AMT spectra of texture feature of microscopic SEM images of composites were derived by AMT method and low-dimension reduced spectra data were extracted by PCA. According to the extracted feature matrix, the microscopic SEM images of composites in different aging periods were recognized and classified based on two kinds of intelligent classifier, Extreme Learning Machine (ELM) and Support Vector Machine (SVM). Our investigation can provide a new way for quantitative characterization and depiction of microscopic surface topography of SEM images of composite material in its aging test and precisely determine the composites' aging stage and indirectly reflect corresponding mechanical, physical, and chemical properties accordingly by using intelligent recognition and classification.

2. Experimental

2.1. Materials. Raw materials of sample preparation of wheat straw/polypropylene composites were shown in Table 1.

2.2. Material Specimen Preparation and Its Accelerated Aging Test. Wheat straw/polypropylene composites were prepared by mixing molding method first; mass fraction of wheat straw powder, zinc stearate, and polypropylene was 50%, 1.5%, and 48.5%, respectively. Then, the specimen of wheat straw/polypropylene composites was made by hot press molding with the size of 120 mm \times 100 mm \times 15 mm. According to the Chinese National Standard GB/T16422.3-1997 UV accelerated aging test for wheat straw/polypropylene composites was conducted. In the aging test, UV-A340 xenon lamp was used, and the temperature of blackboard and condensation was set to 60°C and 50°C, respectively. One aging cycle is 12 h (including illumination, 8 h, and

condensation, 4 h), and every 20 cycles were sampled once totaling 100 cycles (i.e., 1200 h). The 5 different aging periods, respectively, correspond to the 20th, 40th, 60th, 80th, and 100th aging period [12].

2.3. SEM Images Shoot. Before shooting SEM pictures of composites sample, we need to spray gold on them first. SEM photos of microscopic surface topography of the sample bars were acquired using JSW-6300 Scanning Electron Microscope with accelerating voltage 20 kV, and photo magnification is 50x, 100x, and 200x, respectively. Then, after carefully observing the typical region of interest, we carefully chose and took four SEM photos of the microscopic surface topography of specimen of composites in five different aging periods with the original size of 1232 \times 912 pixels for each magnification.

3. Methodology

3.1. Image Preprocessing and Its Subsamples Preparation. After microscopic SEM photos of the composites were shot in five different aging periods, ROI (region of interest) images or image subsamples at the same size (400 \times 400 pixels) were selected from the SEM raw images at the magnification of 100x for the following textural feature extraction and analysis based on AMT method. For each aging stage, 16 preprocessed subsamples of the SEM images (400 \times 400 pixels) of material specimens were chosen out elaborately for classification prediction (i.e., totally 80 subsamples in five different aging periods).

For the entire samples, cross validation was introduced to help construct predictive models and then to validate the models in this work, through which we can assess how the results of the predictive models will generalize to a separate test dataset subsequently (to keep the classification models from overfitting).

3.2. AMT Method. The calculating procedure of AMT method is described below: for a 1D measurement series or 1D digital curve (2D measurement series should be converted to 1D ones first), in each scale factor s , one point from a number of random sampling points (usually 500 points for 1D data series and above 2~5% of the total number of pixels for the unfolded imagery) is chosen as the starting point first and also as the center of the circle with the radius s (i.e., the present scale). The circle intersects the 1D digital curve at 2 points which form an angle with the starting point, taking its supplementary angle into consideration. The calculating angle will change with the location move of the random

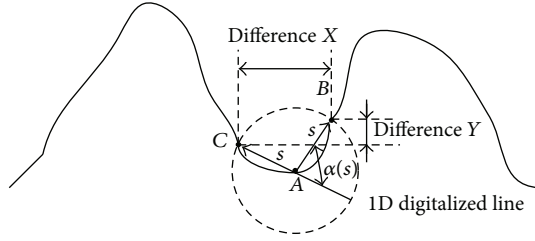


FIGURE 1: Schematic diagram of AMT method.

sampling point in the digital curve at the present scale factor s ; thereby, a series of angle measuring values will be generated and then averaged into one angle, which is called Mean Angle (MA) or $\alpha(s)$ as the function of the scale factor s [8] (see Figure 1). With continuous increase of the scale factor s , the Mean Angle is changing also. The calculating formula of Mean Angle or $\alpha(s)$ according to AMT method is defined as follows:

$$MA = \frac{k}{N} \sum_{i=1}^N (\alpha_i)_s, \quad (1)$$

where $(\alpha_i)_s$ is the i th measuring angle at the present scale s and MA or $\alpha(s)$ is the average of N measurement angles; k is a adjusting factor ranged from 0 to 1 which can enlarge the variation in the unfolded 1D image pixels and it is set to constant 1 in our work.

The production of AMT spectra of SEM images of composites in different aging periods was evaluated using the software ImageJ (NIH, USA, Version 1.46) with AMT plugin script (http://arken.umb.no/~kkvaal/eamtexplorer/imagej_plugins.html) written by Professor Knut Kvaal, Norwegian University of Life Sciences (NMBU). The main selected parameters of AMT spectra of SEM photos of straw/polypropylene composites were as follows:

- (1) Mean Angle measuring is done using AMT linear method.
- (2) Minimum scale radius is 1 pixel, maximum scale radius is 500 pixels, and scale increment is 1 pixel.
- (3) Total number of random sampling points is 5000 points.
- (4) Unfolded type adopts "spiral" (outside to inside way) converting 2D images to 1D digitalized curve.
- (5) Number of sample pixels to unfold selects all.
- (6) Correction option is considered and used to digitize the line, and more information about this choice can be found in [13].

3.3. MA Spectra Extraction Using PCA. AMT spectra (refer to MA spectra commonly used) of SEM images of wheat straw/polypropylene composites in different aging periods have distinct texture features with the extension of material aging cycles (Figure 5), so it is possible to extract the texture characteristics by using AMT method. As the references

reported, MA data is a function depending on continuous factor scale s , and therefore the exported measuring angles $\alpha(s)$ are high-dimensional data and it is possible that multicollinearity of MA spectra might exist in some cases. Raw AMT spectra seemed to be directly employed into the classifier after simply selecting some scale range, but this job was completed by naked eyes of observer resulting in subjective differences and randomness to some extent and possible time-consuming process sometimes. In addition, scale number in the interval(s) of MA spectra might be relatively large compared to the input of some classifier; for instance, the input number of Artificial Neural Network is a few or a dozen usually. It is important to eliminate possible strong collinearity and at the same time to realize data compression. As a matter of fact, the collinearity existed indeed in the MA spectra by observation intuitively (Figure 6). In consideration of these facts first four principal components (PC1~PC4) were extracted from MA spectra by PCA quickly and automatically in this work. After dimensional reduction the compressed MA spectra data was loaded to input matrix of the two following classifiers for the following analysis.

3.4. Classification Prediction Using ELM and SVM

3.4.1. ELM Classification Prediction. ELM is superior to the traditional feed forward neural network in many aspects, such as classification, regression, and artificial intelligence [14, 15]. As a novel single hidden layer of Artificial Neural Network, it can obtain a unique optimal solution finally by randomly generating connection weights between the input layers and hidden layers and thresholds of hidden layer neurons. The weights of the output layer are calculated according to the following formula:

$$\hat{\beta} = H^+ T', \quad (2)$$

where H^+ is Moore-Penrose generalized inverse matrix.

The input of ELM neural network is the first four principal components of MA spectra of the SEM image of composites extracted by PCA. Programming of ELM classification prediction of five different aging stages was realized in MATLAB (MathWorks, USA, Version R2010a), and the program of classification includes two main functions, that is, ELM training function and ELM prediction one [16, 17]. Flow chart of ELM algorithm on predicting classification is shown in Figure 2.

3.4.2. SVM Classification Prediction. SVM is a new data mining technology which is very suitable for small sample statistical analysis and can change the nonlinear classification problem into linear classification one by high-dimensional space transformation [18]. Because the aging period classification of wheat straw/polypropylene composites in aging test is a multiclass classification problem, multiclass SVM classification was utilized here. Algorithm programming of SVM classification prediction of SEM images was realized by using Libsvm software package (Libsvm, Version 3.1) developed by Professor Lin Chih-Jen, National Taiwan University, providing interface with SVM MATLAB toolbox.

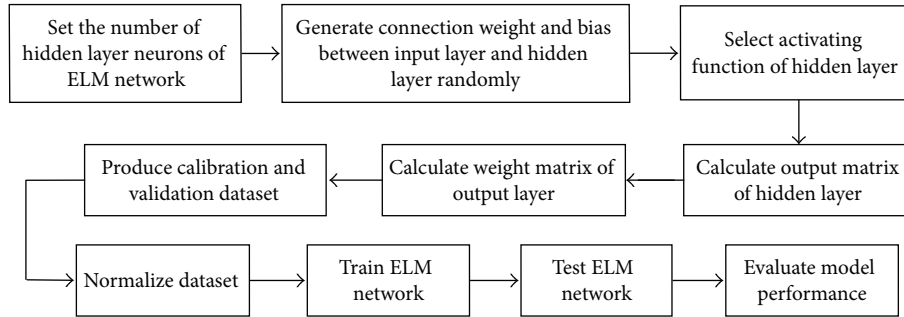


FIGURE 2: Flow chart of ELM algorithm on predicting classification.

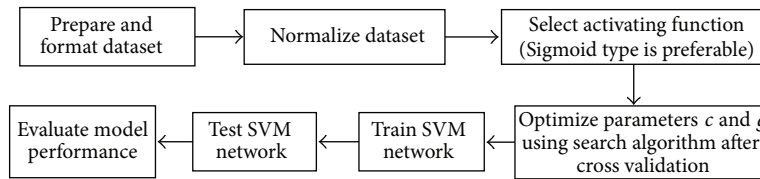


FIGURE 3: Flow chart of SVM algorithm on predicting classification.

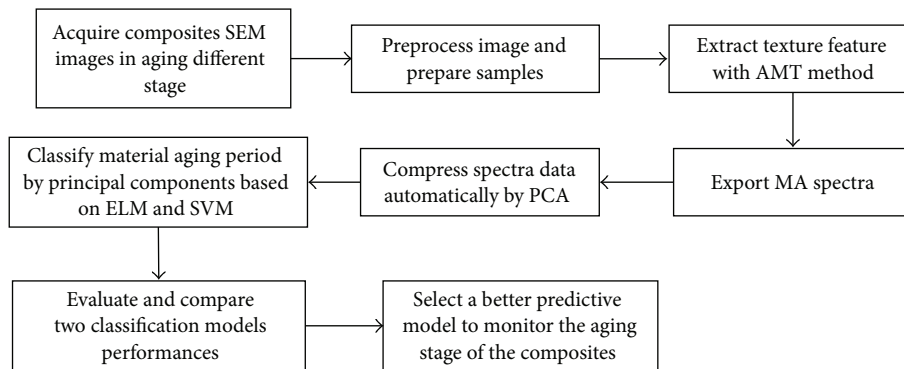


FIGURE 4: System overall diagram of texture feature extraction and classification of SEM images of the composites.

Function SVMcgForClass should be called first when running the program. Using the optimal parameters returned by SVMcgForClass function the classifier model was built and trained through svmtrain function with cross validation procedure; finally svmpredict function with the optimal parameters estimated by the svmtrain function would predict classification results [18, 19]. Flow chart of SVM algorithm on predicting classification is shown in Figure 3.

System overall diagram of texture feature extraction and classification of SEM images of the composites was given in Figure 4.

4. Results and Discussion

4.1. Results

4.1.1. Export and Analysis of AMT Spectra of the Composites SEM Images. For each of the five different aging periods, one image sample which has relatively typical characteristics of aging was picked out and illustrated. SEM image samples of

the composites in five different aging periods are shown in Figure 5.

From Figure 5, it can be easily found that, with the growth of aging time of straw/polypropylene composites, the aging cracks on the surface of the composites gradually appeared, showing that their length, width, and depth were more and more long, more and more large, and more and more deep. At the end of the aging period, the material's surface was severely eroded, resulting in shedding in a huge area. It is obvious that rather distinct texture features are presented by the development and change of those aging cracks in SEM pictures; in other words, the complexity of SEM images of different aging periods is higher and higher. Mean MA spectra of typical SEM image samples of the composites in five different aging periods are shown in Figure 6.

From Figure 6, it is clearly the case where MA spectra of the five SEM images of the composites lay orderly from bottom to top in most of the range of sale domain according to the extension of aging period; that is, spectrum for 20th aging period is at the bottom, the one for 100th aging period is at

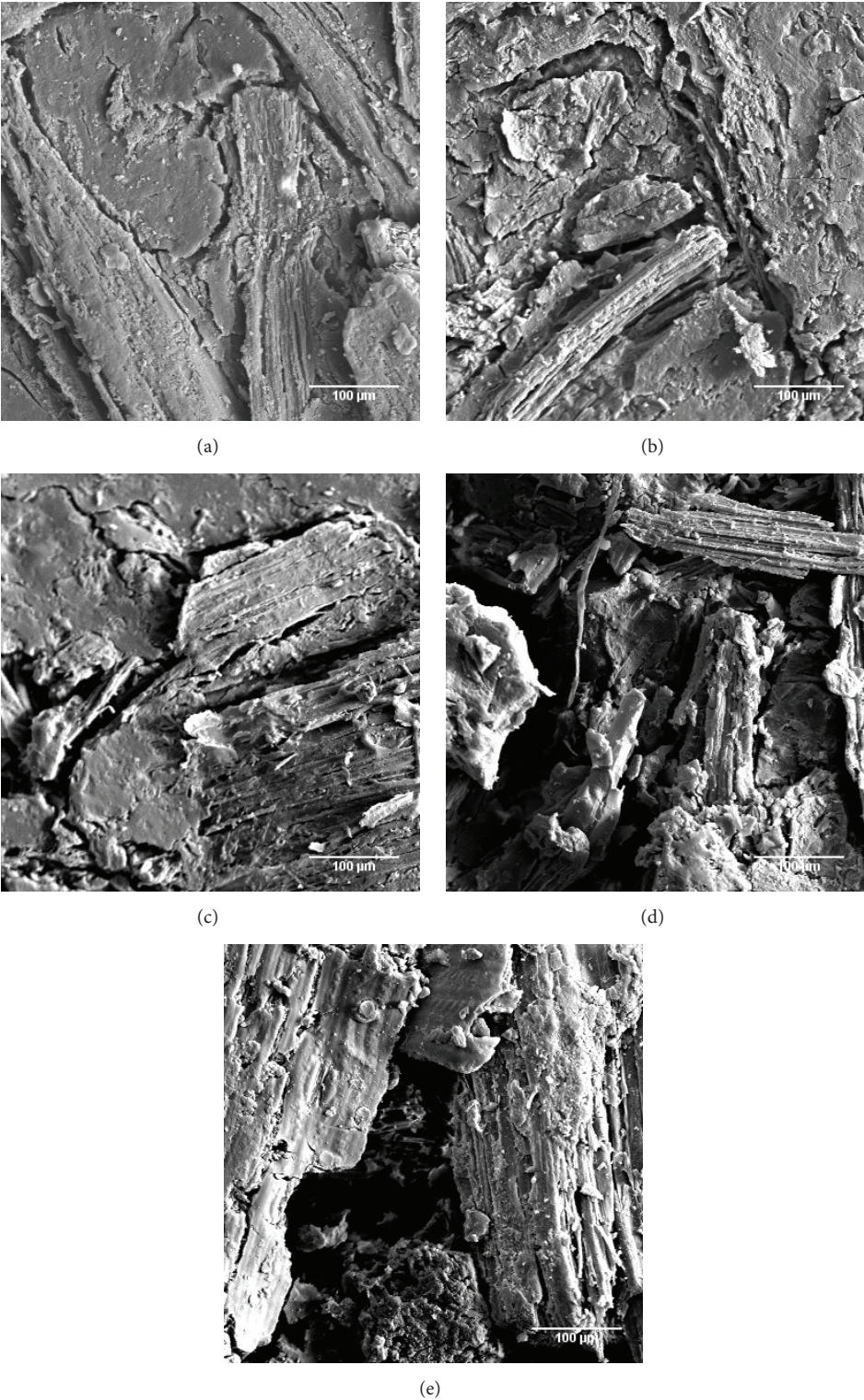


FIGURE 5: SEM image samples of the composites in 5 different aging periods: (a) in 20th aging period; (b) in 40th aging period; (c) in 60th aging period; (d) in 80th aging period; and (e) in 100th aging period.

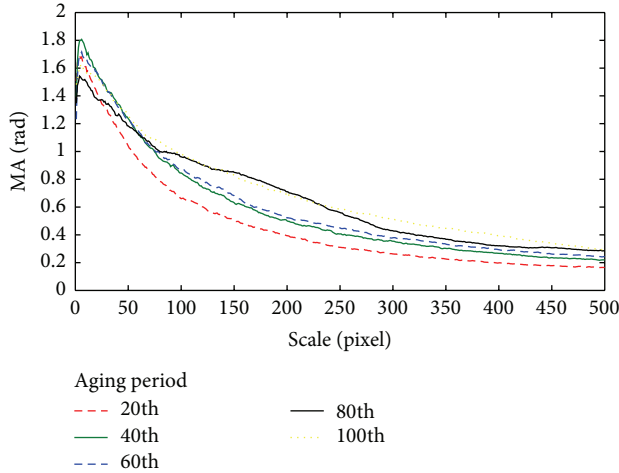


FIGURE 6: MA spectra of SEM image samples of the composites in 5 different aging periods.

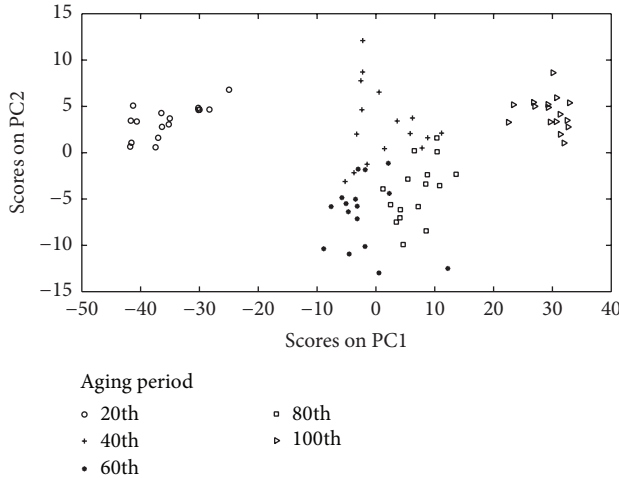


FIGURE 7: PCA scores plot of AMT spectra of SEM image samples of the composites in five different aging periods.

the top, and those for 40th, 60th, and 100th aging period are in the middle, which means that spectrum of 20th aging period has the lowest complexity, while spectrum of 100th aging period has the highest complexity. The spectra correctly characterize and represent the texture complexity of SEM images of the composites in different aging periods. Therefore, it is indicated that AMT spectra have very excellent ability of characterization and discrimination of texture feature of microscopic SEM images of composites in different aging stage. Besides, it can be observed that the collinearity existing among the spectra data ranged approximately from scale 130 to 200 and scale 275 to 500 as those curves in Figure 6 were almost parallel to each other in these two intervals.

PCA analysis was applied to the exported MA spectra of all SEM image subsamples of the composite, and the first two principal components are good enough to explain 97.4% variance of the samples ($PC1 = 86.5\%$, $PC2 = 10.9\%$). Figure 7 displayed PCA scores plot of the whole 80 SEM image

TABLE 2: Sensitivity and 1 – specificity values of classification model using ELM.

Image sample	Sensitivity		1 – specificity	
	Calibration	Cross validation	Calibration	Cross validation
Class 1	1.000	1.000	0	0
Class 2	0.938	0.688	0	0.016
Class 3	0.938	0.813	0.016	0.031
Class 4	0.938	0.875	0.016	0.109
Class 5	1.000	0.938	0	0

subsamples of the composites in five different aging periods. It is possible to see that image samples of the composites in 20th, 80th, and 100th aging cycles are separated distinctly from each other; although the ones in 40th and 60th aging cycles are a little closer to each other, the observers can still easily identify them by scores on PC2 causing a bit bigger difference between the two neighbor groups.

4.1.2. ELM Classification Results. The main parameters of program implementation of ELM classification were as follows: (1) Application type of training function is set to classification recognition; (2) “train_label” takes values from “1” to “5” (corresponding to the five different aging periods; namely, train label of 20th aging period of material SEM images is labeled “class1”, train label of 40th aging period of material SEM images is labeled “class 2,” and so on); (3) type of hidden layer activation function chooses “sig” (Sigmoid function); (4) neurons number of hidden layer was set by cross validation approach after program repetitive running. From repetitive running classification accuracy results of classifiers based on ELM neural network can reach relatively high value when the number of hidden layer neurons approached 17 finally. In order to verify every category classification precision, ROC (Receiver Operating Characteristic) curves of ELM predictive model were used here to evaluate the sensitivity and 1 – specificity values of the predictive model, and the curves of five different categories (corresponding to the five different aging stages) using this model are demonstrated in Figure 8.

Sensitivity and 1 – specificity values of predictive classification model using ELM (with optimal neuron number 17) were reported in Table 2.

4.1.3. SVM Classification Results. The important input parameters of SVM class function were set as follows: (1) “train_label” takes five different values just like the ones in the training function of ELM; (2) $c_{\min} = g_{\min} = -10$, $c_{\max} = g_{\max} = 10$; (3) ν (ν -fold cross validation) = 5; (4) c step = g step = 0.5. Optimal parameters of SVM classification model, that is, c (penalty factor) and g (kernel parameter), are determined by cross validation as well. Parameters optimization of this model was realized by using grid search method after running the function SVMcgForClass. According to the found optimal parameters c and g , that is, $c = 1$, $g = 0.011$, sensitivity and 1 – specificity

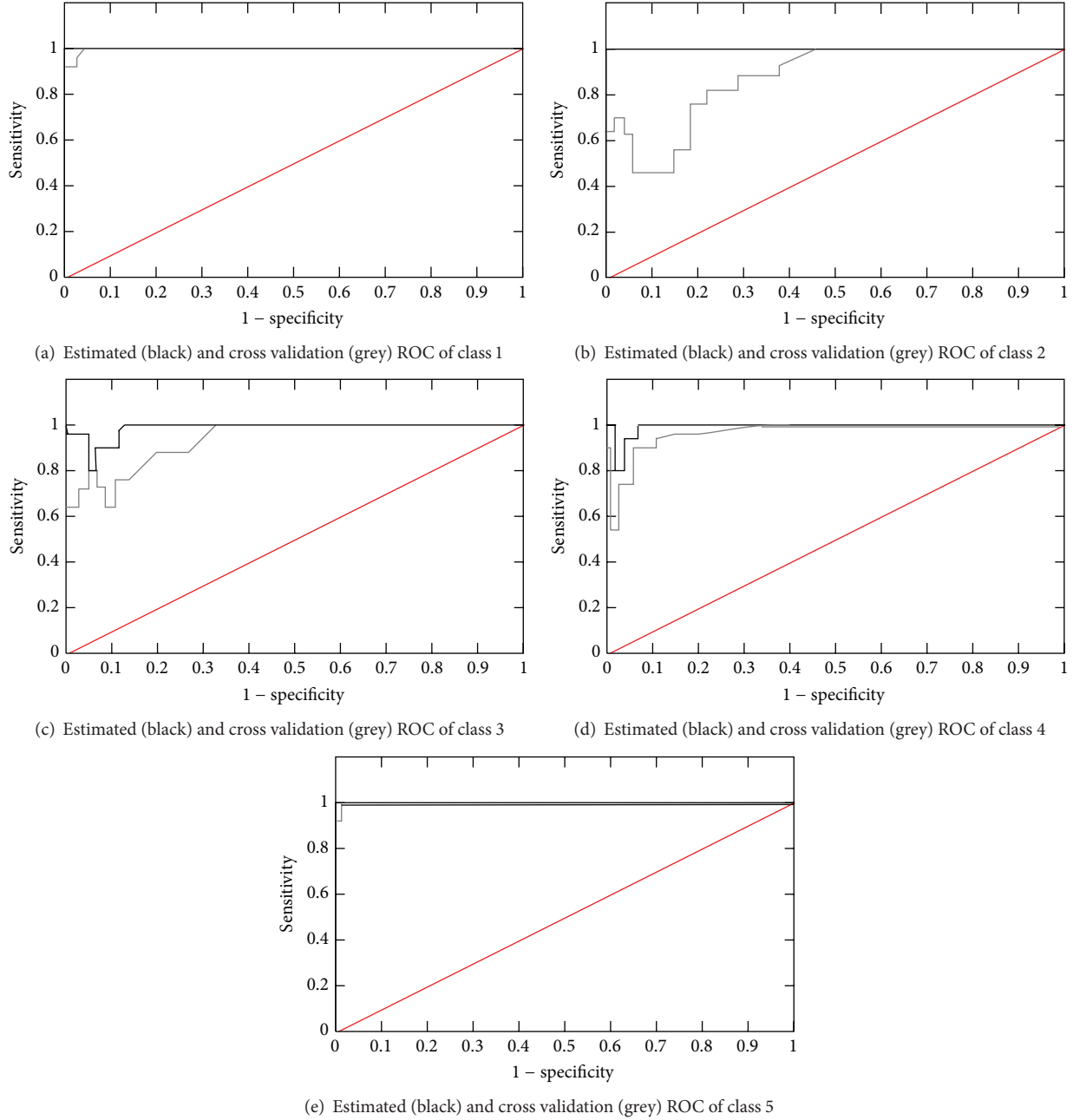


FIGURE 8: ROC curves of ELM classification model of SEM image samples of the composites in five different aging periods.

values (c changed with fixed constant g) and their ROC curves of the second predictive model to predict the five different classes are displayed in Figure 9.

Sensitivity and 1 - specificity values of predictive classification model using SVM (with optimal parameters c and g) were reported in Table 3.

In order to evaluate and compare the predictive ability and performance of two classification models as a whole, statistics results of overall classification accuracy of model using ELM and SVM are reported in Table 4. Due to the randomness of the weight matrix values, the results of ELM class prediction were a little different every time after

program running, so the averaged five preferable running results were taken into account.

4.2. Discussion. From Tables 2 and 3, it is obviously seen that sensitivity values of SVM prediction model were always higher than those of ELM model with respect to the five different classes. For example, sensitivity values of class 2, class 3, and class 4 using SVM model were 0.813, 0.876, and 1.000, respectively, while the values of those three classes using ELM model were only 0.688, 0.813, and 0.875. Meanwhile, 1 - specificity values of the SVM model were commonly lower than that of ELM model; for instance, 1 - specificity values of

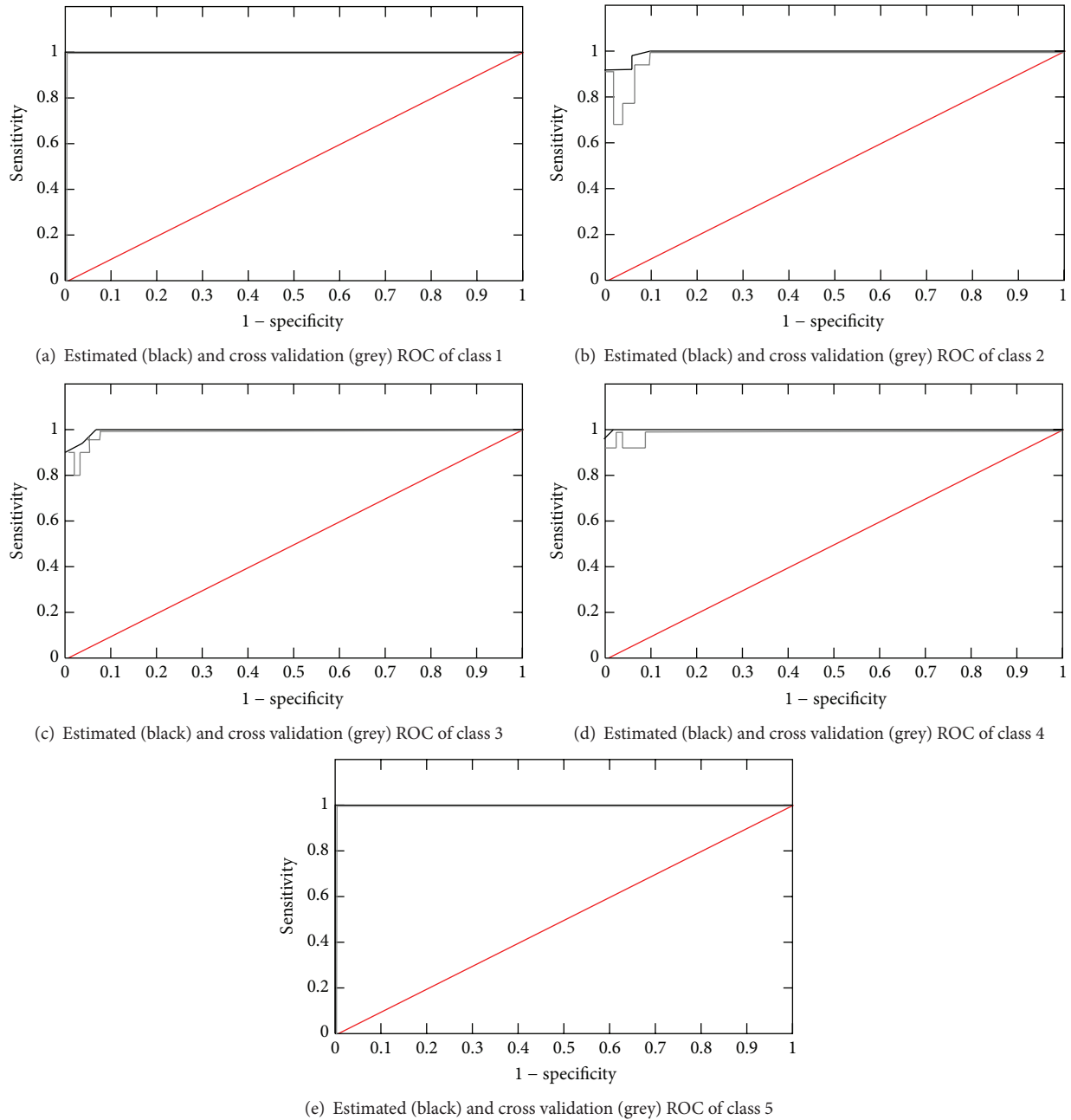


FIGURE 9: ROC curves of SVM classification model of SEM image samples of the composites in five different aging periods.

the three middle classes using SVM model were only 0.016, 0.047, and 0.016, respectively, and nevertheless the values of the same three categories using ELM reached 0.016, 0.031, and 0.109. It was the true case that predictive classification performance of SVM model is better than that of ELM model for each class to be identified. Among the five different classes especially the middle three classes, that is, class 2, class 3, and class 4, it was often the case that, by using SVM model, there is only one adjacent aging period gap between the true categories and estimated ones. For example, the true category of the sample image was “class 2,” while predictive category of it was “class 3.”

Relating to the overall classification results, reported in Table 4, it can be obtained that averaged classification accuracy of calibration dataset using ELM can be 91.5%, and that of validation dataset was 86.3%. Classification accuracy of the classifier using SVM was relatively higher than that of ELM; its averaged classification accuracy of calibration dataset was 93.8%, and that of validation dataset reached 92.5%.

With regard to the first classifier, from the program running results of the classification using ELM neural network, it can be known that this classifier can achieve acceptable classification accuracy. In ELM neural network classification,

TABLE 3: Sensitivity and 1 – specificity values of classification model using SVM.

Image sample	Sensitivity		1 – specificity	
	Calibration	Cross validation	Calibration	Cross validation
Class 1	1.000	1.000	0	0
Class 2	0.942	0.813	0	0.016
Class 3	0.961	0.875	0	0.047
Class 4	1.000	1.000	0	0.016
Class 5	1.000	1.000	0	0

TABLE 4: Statistics results of overall classification accuracy of model using ELM and SVM.

Classifier type	Calibration dataset		Validation dataset	
	Standard deviation	Average	Standard deviation	Average
ELM	6.3%	91.5%	7.2%	86.3%
SVM	4.7%	93.8%	5.6%	92.5%

the number of hidden layer neurons of training function is a very important parameter, and with regard to ELM classifier this parameter value mentioned above has a very significant impact. It showed that through training function repeatedly running as the number of the hidden layer neurons was close to 17 relatively high classification accuracy can be achieved. However, continuing to increase the number of the hidden layer neurons, classification prediction accuracy of test set samples would not increase significantly consequently. As for the second classifier, from the program running results of the classifier using SVM, it can be seen that the classifier can obtain higher classification accuracy than the former. In other words, the number of misjudged samples by using SVM model was a little lower than that of ELM. In view of the classification prediction accuracy, accuracy of ELM was slightly lower than that of SVM actually, and for the goal of getting a higher classification accuracy determination of the number of hidden layer neurons using ELM classifier needs to run program repetitively, and it may take a very long time. However, the number of called function and optimal parameters of ELM classifier were much less than that of SVM, so its parameter setting process was relatively simpler and faster.

5. Conclusions

In summary, research results in this paper indicate that AMT method can well describe the textural feature of SEM images of microscopic surface topography of the composite. AMT method is capable of expressing discriminating and quantitative characterizations of texture complexity of SEM images. The feasibility and effectiveness of textural feature extraction using AMT method has been proved. According to extracted AMT spectra of SEM images of wheat straw/polypropylene composites in five different aging periods, two classifiers based on ELM and SVM were applied to identify those

different aging stages. For the two models SVM model performed better than ELM model in general according to the sensitivity and 1 – specificity values and ROC curves and the overall classification accuracy. Classification approach of SEM images by using AMT spectra and classifier based on this complexity scale data has been verified. It can be expected that growing applications based on AMT method, including research and development of new type composite material, will be increasingly and intensively investigated in more and more aspects.

Conflict of Interests

The authors declare that there is no conflict of interests regarding the publication of this paper.

Acknowledgments

This work was supported by the Funded Projects of “Twelfth Five-Year” National Science and Technology Support Plan (Grant no. 2011BAD20B03-02), Basic Scientific Research Special Funds for the Central Universities (no. KYZ200921), and Open Project of Jiangsu Key Laboratory of Large Engineering Equipment Detection and Control (no. JSKLEDC201204). Particularly, sincere and deep thanks are due to Professor K. Kvaal who gave the authors so much guidance and inspiration continually, and it has never been changing that his help finds the authors well and timely always.

References

- [1] R. Selden, B. Nystrom, and R. Langstrom, “UV aging of polypropylene/wood-fiber composites,” *Polymer Composites*, vol. 25, no. 5, pp. 543–553, 2004.
- [2] J. S. Fabiyi, A. G. McDonald, M. P. Wolcott, and P. R. Griffiths, “Wood plastic composites weathering: visual appearance and chemical changes,” *Polymer Degradation and Stability*, vol. 93, no. 8, pp. 1405–1414, 2008.
- [3] N. M. Stark and L. M. Matuana, “Characterization of weathered wood-plastic composite surfaces using FTIR spectroscopy, contact angle, and XPS,” *Polymer Degradation and Stability*, vol. 92, no. 10, pp. 1883–1890, 2007.
- [4] Y. X. Zhou, F. Pervin, S. Jeelani, and P. K. Mallick, “Improvement in mechanical properties of carbon fabric-epoxy composite using carbon nanofibers,” *Journal of Materials Processing Technology*, vol. 198, no. 1–3, pp. 445–453, 2008.
- [5] D. S. Raimundo, P. B. Caliope, D. R. Huanca, and W. J. Salcedo, “Anodic porous alumina structural characteristics study based on SEM image processing and analysis,” *Microelectronics Journal*, vol. 40, no. 4–5, pp. 844–847, 2009.
- [6] J. A. Galloway, M. D. Montminy, and C. W. Macosko, “Image analysis for interfacial area and cocontinuity detection in polymer blends,” *Polymer*, vol. 43, no. 17, pp. 4715–4722, 2002.
- [7] R. Andrieu, “The angle measure technique: a new method for characterizing the complexity of geomorphic lines,” *Mathematical Geology*, vol. 26, no. 1, pp. 83–97, 1994.
- [8] J. Huang and K. H. Esbensen, “Applications of angle measure technique (AMT) in image analysis: part I. A new methodology for in situ powder characterization,” *Chemometrics and Intelligent Laboratory Systems*, vol. 54, no. 1, pp. 1–19, 2000.

- [9] U. G. Indahl and T. Næs, "Evaluation of alternative spectral feature extraction methods of textural images for multivariate modeling," *Journal of Chemometrics*, vol. 12, no. 4, pp. 261–278, 1998.
- [10] S. Kucheryavski, "Using hard and soft models for classification of medical images," *Chemometrics and Intelligent Laboratory Systems*, vol. 88, no. 1, pp. 100–106, 2007.
- [11] L. Fongaro and K. Kvaal, "Surface texture characterization of an Italian pasta by means of univariate and multivariate feature extraction from their texture images," *Food Research International*, vol. 51, no. 2, pp. 693–705, 2013.
- [12] R. L. Hou, C. X. He, J. Xie, Y. Min, and D. Chuanchuan, "UV accelerated aging properties of wheat straw/PP wood plastic composite," *Acta Materiae Compositae Sinica*, vol. 30, no. 5, pp. 86–93, 2013.
- [13] S. V. Kucheryavski, K. Kvaal, M. Halstensen et al., "Optimal corrections for digitization and quantification effects in angle measure technique (AMT) texture analysis," *Journal of Chemometrics*, vol. 22, no. 11-12, pp. 722–737, 2008.
- [14] J. Luo, C.-M. Vong, and P.-K. Wong, "Sparse bayesian extreme learning machine for multi-classification," *IEEE Transactions on Neural Networks and Learning Systems*, vol. 25, no. 4, pp. 836–843, 2014.
- [15] X. Lu, H. Zou, H. Zhou, and L. Xie, "Robust extreme learning machine with its application to indoor positioning," *IEEE Transaction on Cybernetics*, 2015.
- [16] G.-B. Huang, Q.-Y. Zhu, and C.-K. Siew, "Extreme learning machine: theory and applications," *Neurocomputing*, vol. 70, no. 1–3, pp. 489–501, 2006.
- [17] G. Feng, G.-B. Huang, Q. P. Lin, and R. Gay, "Error minimized extreme learning machine with growth of hidden nodes and incremental learning," *IEEE Transactions on Neural Networks*, vol. 20, no. 8, pp. 1352–1357, 2009.
- [18] V. Cherkassky and Y. Q. Ma, "Practical selection of SVM parameters and noise estimation for SVM regression," *Neural Networks*, vol. 17, no. 1, pp. 113–126, 2004.
- [19] J. Ma, J. Theiler, and S. Perkins, "Accurate on-line support vector regression," *Neural Computation*, vol. 15, no. 11, pp. 2683–2703, 2003.

Research Article

Mechanic and Acoustic Properties of the Sound-Absorbing Material Made from Natural Fiber and Polyester

Limin Peng,¹ Boqi Song,¹ Junfeng Wang,² and Dong Wang¹

¹Research Institute of Wood Industry, Chinese Academy of Forestry, Beijing 100091, China

²GuangXi Zhuang Autonomous Region Forestry Research Institute, Nanning 530002, China

Correspondence should be addressed to Limin Peng; penglm@caf.ac.cn

Received 16 October 2014; Accepted 31 December 2014

Academic Editor: Xinfeng Xie

Copyright © 2015 Limin Peng et al. This is an open access article distributed under the Creative Commons Attribution License, which permits unrestricted use, distribution, and reproduction in any medium, provided the original work is properly cited.

A sound-absorbing composite material made of wood fiber and polyester fiber was produced using polyester foam technology and wood-based composite technology. This study investigated the physical and mechanical properties and the effects of the airflow resistivity of the materials and the depth of the cavities behind on sound-absorbing performance of the composite material. The results showed that the composite of best physical and mechanical properties and sound absorption was made with a 150°C hot-pressing temperature, 10 min hot-press time, 3:1 the ratio of wood fiber to polyester fiber, foaming agent content of 8%, and the nominal density of 0.2 g/cm³; the composite material yielded superior sound absorption property with the airflow resistivity of 1.98×10^5 Pa·s/m²; the acoustic absorption peak moved to lower frequencies when length of the cavities was increased.

1. Introduction

Noise has become one of the four major pollution types in the world. Constant exposure to noises can cause all kinds of health problems, such as hearing loss, cardiovascular disease, and sleep disorder [1]. It is imperative to produce cost-effective and environmental-friendly materials that can reduce noise pollution.

Natural fibers have been extensively used to produce environmentally friendly composite materials. Natural fibers, such as wood, hemp, and coconut shells, hold great potential for substituting the expensive synthetic fibers in manufacturing acoustic absorption boards due to their abundance, low cost to process, and the natural cellular structure, which can effectively absorb acoustic energy.

Porous materials are important sound-absorbing materials. Studies on the sound absorption properties of various porous materials have been done since 1970s. Delany and Bazley's study on glass fiber and mineral wool found that the absorption coefficient of cellular sound-absorbing materials was lower in low frequency, and it kept an upward tendency as the frequency went up. They established an empirical model of acoustic absorption coefficient with airflow resistivity [2].

However, this method was valid only for limited types of materials with specific characteristics. Luo and Li proposed that natural fiber reinforced composites had better acoustic properties than their synthetic counterparts but still failed to meet the requirements for acoustic materials [3]. The study by Ersoy and Küçük indicated that the absorption peak moved from 6300 Hz to 4000 Hz when the thickness of the tea-fiber materials was doubled [4]. Zulkifli et al. worked on coconut fiber and found that the absorption coefficient could reach 0.70 to 0.80 in the frequency range of 1000–1800 Hz [5]. Narang studied the influence of the surface density, fiber morphology, and bonding fiber content on the sound absorption property of polyester fiberboard and found that the absorption coefficient increases with increasing surface density at low and medium frequencies. The best absorption property was obtained when the bonding fiber content was 35% [6]. Küçük and Korkmaz's study on the mix of natural fiber and nonwoven materials showed that the physical properties of the blending materials had a great influence on the sound absorption property of the mixed material. The results showed that as the thickness of the materials increased, the air permeability decreased and the flow resistance was improved, leading to sound absorption enhancement [7].

TABLE 1: The physical and chemical properties of the composite materials.

Text item	Density (g/cm ³)	MC (%)	2 h thickness expansion rate of water absorbing (%)	MOR (MPa)	IB (MPa)	Formaldehyde emission content (mg/100 g)
Standard (functions)	$\rho < 0.35$	4–12	≤ 12	≥ 2.0	—	9
Text value	0.20	3.7	5.9	2.6	0.42	0

Sound absorption mechanisms of the composite were the following three aspects: (1) when acoustic waves propagated into the fibrous material, the air in the fiber pores vibrated and rubbed against cell walls. The generated viscous resistance turned the acoustic energy into thermal energy attenuation. (2) The air in the pores was heated when compressed and it cooled when expanded. The thermal conduction in the materials made acoustic energy transform into thermal energy gradually and it was irreversible. (3) The vibration of fiber itself could also cause the dissipation of acoustic energy. These three aspects cooperated and worked together on the acoustic waves so that the acoustic energy was transferred [8–10].

Polyester fiber is widely used and the polyester fiber board shows the characteristics of good sound absorption property, while the chemically synthesized polyester fiber has the problem of high environmental pollution and high cost. Under the premise in sound absorption, wood fiber was used to substitute parts of the polyester fiber, which could reduce the pollution and lower the cost. In this research, a series of tests were conducted to determine the optimum process parameters for wood fiber/polyester fiber composite sound-absorbing material. The physical and mechanical properties of the material were measured based on the relevant standards. The porous microstructure of the materials was observed with scanning electron microscopy to analyze the mechanism of sound absorption. The sound absorption coefficients under different conditions were tested in transfer function method with impedance tubes. The relationships between the sound absorption properties of composite materials and airflow resistance as well as the thickness of the cavities were obtained after comparison and analysis.

2. Material and Methods

2.1. Materials. Poplar wood fiber was obtained from the research forest of Chinese Academy of Forestry. The wood fiber was dried to the moisture content of 2%–5%. Polyester fiber was purchased from Shandong Taian plastic factory (PET, solid fiber, with circular cross section and diameter is 30 μm , length is 6 mm, and specific gravity is 1.36). Under laboratory conditions the wood fiber and polyester fiber were artificially premixed in a ratio of 3:1 and then mixed uniformly through wind conveyer. Air-lay web technology was used to get the isotropic structure of the composites. Polyester fiber was fed into the air-laid web-forming machine for opening and mechanical beat and tear to loose fiber bundle and then went through carding machine for combing. Wood fiber was added and the hybrid went through the opener again. Then the mixed fiber was formed under centrifugal force and suction airflow. Isocyanate adhesive

(100% solid content, tech grade) for binding fibers was purchased from Huntsman Polyurethanes Shanghai, Ltd. The resin content was 12%. The dried hybrid fiber was rolling in the blender while adhesive was sized in the form of spray. Then 8% foaming agent (modified foamer ADC, purchased from Shanghai Fine Raw Chemicals Co., Ltd., tech grade) was added to improve the porosity. ADC released nitrogen, carbon monoxide, and ammonia when heated. ADC was an exothermic foaming agent which might release uncontrollable heat and decreased the viscosity of melt. This would generate a lot of bubbles and coupled together to form a larger aperture, the material constituting the porous internal structure of the voids increased. The decomposition temperature of pure ADC was 190 to 210°C, while it was 135 to 145°C for modified ADC, which was consistent with the curing temperature of adhesive.

The preformed fiber was preloaded and then hot pressed for 10 min under the hot press (produced by Shanghai wood-based panel mechanical factory, Model QD) at 150°C. The target density of composite fiber board was 0.2 g/cm³, and the finish size was 400 mm \times 400 mm \times 10 mm. These panels were then cut into test samples fitting the relevant standard for the following tests.

2.2. Methods

2.2.1. Sound Absorption Measurement. According to the relevant testing standard [11], using impedance tubes (model number: UA-1630, Bruel & Kjar Co., Ltd., Demark), the experiment was conducted in a semianechoic room at 20.0°C and 50% relative humidity (RH). For each variable 1500 separate data points in the frequency range of 50–6400 Hz were obtained every 4 Hz.

2.2.2. Airflow Resistance Measurement. According to the relevant testing standard [12], the airflow resistivity was measured with the test system of flow resistance instrument adopting water tank method (Figure 1) in direct current (DC) method. The differential pressure levels above and beneath the specimen surface were measured by controlling the transmit time of one-way flow through the cylindrical tube.

3. Results and Analysis

3.1. Physical and Mechanical Properties of Composite Material. The properties of the composite material are listed in Table 1. The standard values of the properties required by the Chinese Industry Standard LY/T 1718-2007 light fiberboard [13] are listed as well for comparison. The composite material samples were manufactured using the following parameters: hot-pressing temperature, 150°C; composite time, 10 min; wood

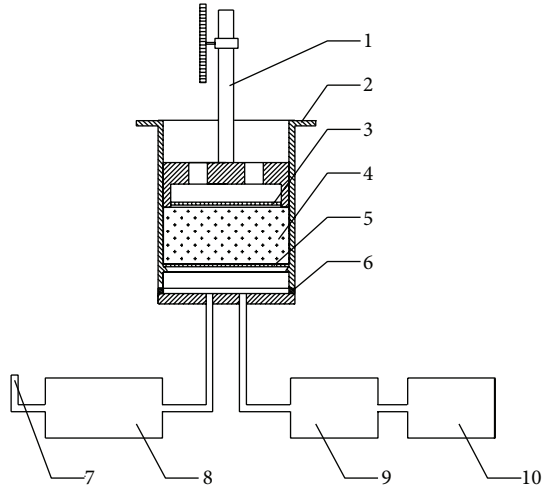


FIGURE 1: Measurement equipment in cross section by DC method. 1: piston with thickness indicator. 2: measure specimen cylinder barrel. 3: grid or perforation plate. 4: specimen. 5: grid or perforation plate for supporting the specimen. 6: seal ring. 7: opening to the atmosphere. 8: differential pressure measuring equipment. 9: flow meter. 10: air supply.

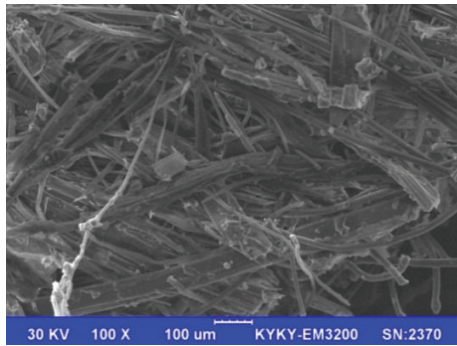


FIGURE 2: SEM of composite material at 100x.

fiber to polyester ratio, 3 : 1; foaming agent content, 8%; and the target density, 0.2 g/cm³.

As shown in Table 1, the moisture content (MC) of the composite material was lower than the standard requirement. This was due to the low hygroscopicity of polyester fiber (MC < 0.5%) and the low moisture content of dried wood fiber (2–5%). The 2-hour thickness expansion rate of water absorption and the MOR of the composite material exceeded the standard requirements. The IB of the composite material was 0.42 MPa, indicating that the material was strong enough to survive regular handling and installation.

3.2. Acoustic Properties of the Composite Material. Figures 2 and 3 show the structures of the material under different magnifications.

As shown in Figure 2, the material contained irregular pore structures composed of interlaced fibers. Figure 3 showed the holes formed from solidified adhesive under the effect of foaming agent. These SEM images showed that

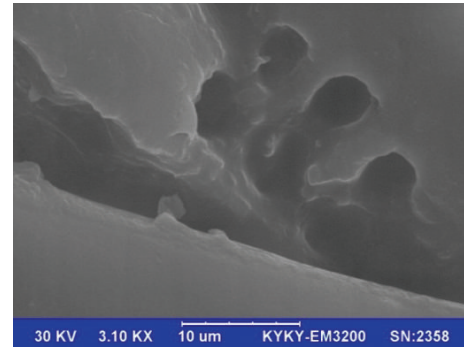


FIGURE 3: SEM of foaming structure of the composite at 3.10kx.

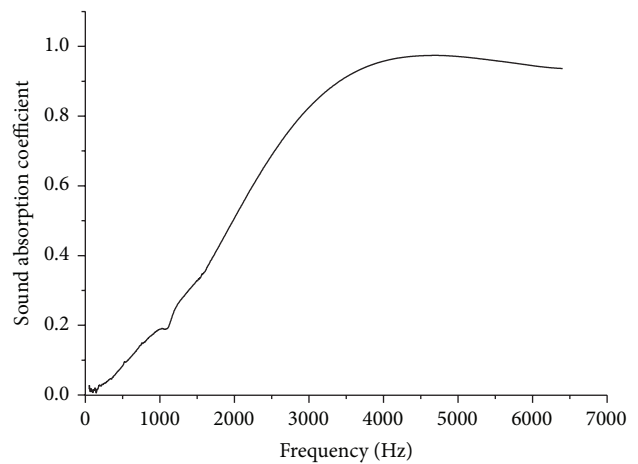


FIGURE 4: The absorption coefficient of wood fiber/polyester fiber composite materials.

the composite pores were made of the voids between the fibers and those formed by the foaming agent.

The sound absorption coefficient of the wood fiber and polyester fiber composite material is shown in Figure 4. The composite material had higher sound absorption coefficients at high frequency range. The absorption coefficient was more than 0.8 in the frequency range of 2892–6500 Hz, and the highest absorption coefficient was 0.97 at 4660 Hz. The wood fiber/polyester fiber composite materials were fibrous porous composite materials where interlaced wood fiber and polyester fiber constituted similar pore structures inside and outside; thus it created the conditions for the entrance to the materials for acoustic waves.

3.3. Factors Affecting the Acoustic Properties of the Composite Material

3.3.1. The Influence of Airflow. The air permeability of the materials can be characterized in terms of airflow resistance, which is measured by the ratio of static differential pressure between both sides of the specimen to the airflow velocity when air flows through the materials. Flow resistivity is the flow resistance per unit thickness of the tested material. The flow resistivities of 3 samples with different densities

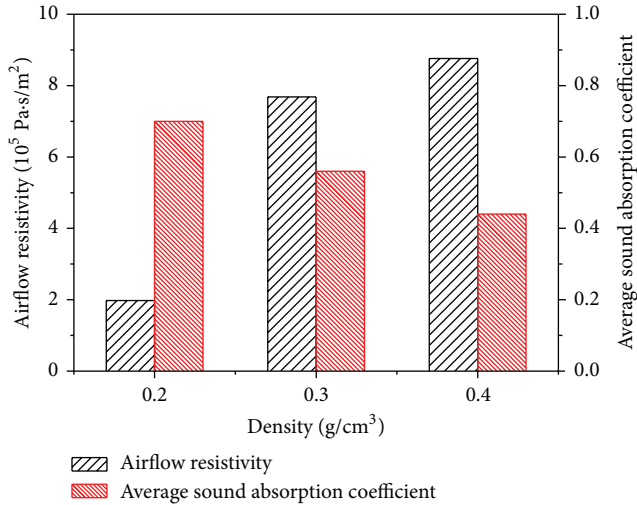


FIGURE 5: The relationship between the average sound absorption coefficient and airflow resistivity of the composites of different densities.

were measured. The average absorption coefficient was the arithmetic mean of 6 sound absorption coefficient values at the central frequencies of 1 octave band width range 125~4000 Hz. Figure 5 showed the relationship between the average absorption coefficient and airflow resistivity of the composite.

The average absorption coefficients of each sample were 0.70, 0.56, and 0.44, respectively. As shown in Figure 5, the sound absorption coefficient decreased sharply as the flow resistivity went up. And there was a strong correlation between airflow resistivity and density.

Actually, as the density and airflow resistivity increased, the average sound absorption coefficient was firstly increased and then decreased. In a certain range of the thickness of the materials, the larger density means the denser structure. The resistance of air particle through the material was increased, and the average sound absorption coefficient was decreased. There was a best airflow resistivity δ_0 and corresponding density ρ_0 for certain composite fibrous material. When the composite density was less than ρ_0 , there was more and larger voids inside the material and less acoustic wave reflection and refraction. So it was easy for acoustic waves to propagate through the material. Moreover, the internal surface area was small; the friction and viscous resistance between the vibrating air particle and fiber was low. Hence the sound absorption property was poor. In addition, when the density was larger than ρ_0 and the flow resistivity was too high, most of the acoustic energy was reflected at the surface rather than transmission so that the absorption properties were decreased. According to Hong's research, as the flow resistivity went higher, the absorption coefficient was reduced at almost all frequencies [14]. However, the flow resistivity had only a small effect on the peak location of the absorption coefficient. The above observation of the decrease of absorption coefficient was reasonable as a high flow resistivity tended to reflect the incoming acoustic wave rather than absorbing the sound wave. The sound absorption

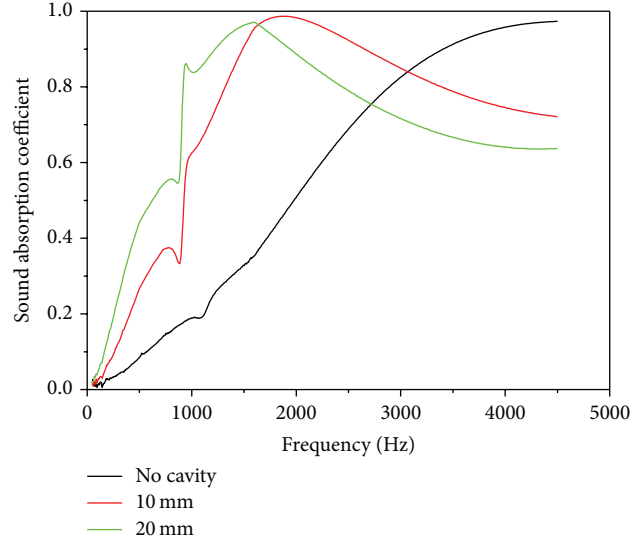


FIGURE 6: The sound absorption coefficient of the composites under different thickness of the cavity.

properties of the materials could be adjusted by controlling the flow resistance. The best airflow resistivity for wood fiber/polyester fiber composite sound-absorbing materials was $1.98 \times 10^5 \text{ Pa}\cdot\text{s}/\text{m}^2$.

3.3.2. The Influence of the Depth of the Cavity. As shown in Figure 6, the absorption coefficient of material with a cavity of 10 mm thickness between the composites and rigid back was higher than that of materials without cavities behind at the frequency range of 0 to 3000 Hz, and it was increased significantly at the frequency range of 50 to 1500 Hz. When the thickness of the cavity between the composites and rigid back was increased up to 20 mm, the absorption coefficient was higher than that of cavity thickness of 10 mm at the frequency range of 0 to 1500 Hz, while it decreased quickly at the frequencies from 1500 Hz. Consequently, it could largely enhance the sound absorption property of the composite materials at low and medium frequency ranges by setting cavities of a certain thickness behind them, whereas the enhancement became less obvious when the thickness increased up to a certain value; meanwhile the absorption coefficient was decreased obviously at high frequency. In a practical application, there is usually a certain depth of cavity between material and rigid back to enhance the sound absorption property in low frequency, which can be seen as enlarging the thickness of the materials. In conformity to the acoustic principle, when the thickness of the rear air layer equaled odd-numbered quarter wavelength, the sound absorption coefficient increased to the maximum. It is because the sound pressure 1/4 far from rigid backing was zero and the air particle vibration velocity was maximum so that the sound energy loss caused by friction damping was maximum. In other words, the acoustic energy was utmost absorbed by the composite material, while the sound pressure which was integer times of 1/2 wavelength far from the rigid

backing was maximum and the particle vibration velocity was zero. Accordingly, the sound absorption coefficient was minimum at the relevant frequency. This character is often used for material savings in construction.

4. Conclusions

Results obtained from this study led to the following conclusions.

- (1) The composite materials yield superior physical and mechanism properties in the conditions in which the hot-pressing temperature was 150°C, composite time was 10 min, the ratio of wood fiber to polyester was 3 : 1, the resin content was 12%, foaming agent content was 8%, and the density was 0.2 g/cm³.
- (2) The sound absorption property of the wood fiber/polyester fiber composite was related to the airflow resistivity. The sound absorption coefficient of the material increased as the airflow resistance values decreased. When the airflow resistivity continued to reduce and exceeded the optimum value, the sound absorption coefficient of the materials showed a trend of decrease. The optimum airflow resistivity value of the composite materials was 1.98×10^5 Pa·s/m².
- (3) When there were cavities behind the composite material, the sound-absorbing peak value moved to lower frequencies. As the thickness of the cavities increased, the increase of the sound absorption coefficient in the low frequency range became less obvious.

Conflict of Interests

The authors declare that there is no conflict of interests regarding the publication of this paper.

Acknowledgments

The authors would like to thank Chinese Academy of Forestry for the financial and technical support through The State Bureau of Forestry 948 Project Introduction of international advanced forestry science and technology plan “Manufacturing technology recommendation of high performance wood based composite sound absorbing materials” (2013-4-15).

References

- [1] L. L. Shi, *Labotary study of the noise annoyance of the low frequency noise [Ph.D. thesis]*, Zhejiang University, 2004.
- [2] M. E. Delany and E. N. Bazley, “Acoustical properties of fibrous absorbent materials,” *Applied Acoustics*, vol. 3, no. 2, pp. 105–116, 1970.
- [3] Y. Luo and Y. Li, “Acoustical studies of natural fiber reinforced composites,” *Journal of Materials Engineering*, no. 4, pp. 51–54, 2010.
- [4] S. Ersoy and H. Küçük, “Investigation of industrial tea-leaf-fibre waste material for its sound absorption properties,” *Applied Acoustics*, vol. 70, no. 1, pp. 215–220, 2009.
- [5] R. Zulkifli, M. J. Mohd Nor, M. F. Mat Tahir, A. R. Ismail, and M. Z. Nuawi, “Acoustic properties of multi-layer coir fibres sound absorption panel,” *Journal of Applied Sciences*, vol. 8, no. 20, pp. 3709–3714, 2008.
- [6] P. P. Narang, “Material parameter selection in polyester fibre insulation for sound transmission and absorption,” *Applied Acoustics*, vol. 45, no. 4, pp. 335–358, 1995.
- [7] M. Küçük and Y. Korkmaz, “The effect of physical parameters on sound absorption properties of natural fiber mixed nonwoven composites,” *Textile Research Journal*, vol. 82, no. 20, pp. 2043–2053, 2012.
- [8] W. D. Yang and Y. Li, “Sound absorption performance of natural fibers and their composites,” *Science China Technological Sciences*, vol. 55, no. 8, pp. 2278–2283, 2012.
- [9] J. F. Allard, *Propagation of Sound in Porous Media: Modelling Sound Absorbing Materials*, John Wiley & Sons, London, UK, 2009.
- [10] X. Z. Zhong, *The Construction Materials for Sound Absorption and Insulation*, Chemical Industry Press, Beijing, China, 2012.
- [11] ISO, “Acoustics—determination of sound absorption coefficient and impedance in impedance tubes—part 2: transfer function method,” ISO 10534-2, International Organization for Standardization, 1998.
- [12] ISO 9053: 1991, *Acoustics—Materials for Acoustical Applications—Determination of Airflow Resistance*, 1991.
- [13] LY/T 1718-2007, “Light fiberboard,” 2007.
- [14] K. W. Hong, *Acoustical estimation of macroscopic properties of poroelastic materials [Ph.D. thesis]*, Purdue University, West Lafayette, Ind, USA, 2009.

Research Article

Reduced-Pressure Boiling Extraction of Oleuropein Coupled with Ultrasonication from Olive Leaves (*Olea europaea* L.)

**Pu-jun Xie,^{1,2,3,4,5} Li-xin Huang,^{1,2,3,4,5} Cai-hong Zhang,^{1,2,3,4,5}
Feng You,^{1,2,3,4} Cheng-zhang Wang,^{1,2,3,4,5} and Hao Zhou^{1,2,3,4,5}**

¹Institute of Chemical Industry of Forest Products, CAF, Nanjing, Jiangsu 210042, China

²National Engineering Laboratory for Biomass Chemical Utilization, Nanjing, Jiangsu 210042, China

³Key and Open Laboratory on Forest Chemical Engineering, SFA, Nanjing, Jiangsu 210042, China

⁴Key Laboratory of Biomass Energy and Material, Nanjing, Jiangsu 210042, China

⁵Institute of New Technology of Forestry, CAF, Beijing 100091, China

Correspondence should be addressed to Li-xin Huang; l.x.huang@163.com

Received 28 September 2014; Accepted 15 December 2014

Academic Editor: Xinfeng Xie

Copyright © 2015 Pu-jun Xie et al. This is an open access article distributed under the Creative Commons Attribution License, which permits unrestricted use, distribution, and reproduction in any medium, provided the original work is properly cited.

Oleuropein was extracted from *Frantoio* olive leaves using reduced-pressure boiling extraction coupled with ultrasound-assist (URPE). Four important factors, extraction temperature, ultrasonic power, ethanol concentration, and the ratio of solid to liquid, were selected to carry out the response surface methodology (RSM) for seeking optimal conditions on high oleuropein extraction yield at different levels. Box-Behnken design was employed to investigate the effects of the four factors on it. The results showed that the ratio of solid to liquid was the most significant factor of all on oleuropein yield. The optimal operation conditions were obtained as follows: ethanol concentration 75% (v/v), extraction temperature 53°C, ultrasonic power 600 W, and the ratio of solid to liquid 1:31. Under these optimal conditions, oleuropein extraction yield was 7.08%, which was close to the predicted value 7.121%. The scanning electron microscope (SEM) images of olive leaves after extraction were provided as well. It was seen that, compared with the untreated leaves, URPE could effectively break cells within the olive leaves.

1. Introduction

The olive trees (*Olea europaea*, Oleaceae) are widely distributed in China, Spain, Italy, Greece, and so forth [1]. The fruits of the trees could be squeezed into olive oil for edibility. It was considered as the main resource of dietary fat in Mediterranean countries and the most popular edible oil in the world [2]. However, full advantages of the leaves from the olive trees were not taken in the oil extraction process from olive fruit in most of oil mills. Olive leaves were burned or directly thrown away from the mills as environmentally detrimental waste products. In fact, it was discovered that olive leaves could be used as a folk remedy to treat fever and other diseases, such as malaria [3]. Beside olive oil, recent studies showed that many bioactive components such as oleuropein, hydroxytyrosol, verbascoside, rutin, and olive biophenols (OBPs), were found in oil leaves [4]. For

OBPs indicated a few of pharmacology properties for healthy benefits, that is, antioxidant [5–10], anti-inflammatory [11], antimicrobial [12–16], antitumor [17], anticancer [18], protection of cardiovascular disease [9, 19], and antidiabetics [20]. Nowadays, bioactive components, that is, oleuropein, have also been seen in cosmetics and pharmaceuticals field. The chemical structure of oleuropein was shown in Figure 1 [21, 22]. Moreover, it was observed that oleuropein content in olive leaves was greater than that in olive oil, and also the highest of all the different parts of the same olive tree, that is, olive fruit, bud and bark [23]. Therefore, it was very important for the researcher to find a highly effective and timely extraction method with the low cost in the processing of olive leaves.

It is known that, in the plant extraction field, conventional solvent extraction (CSE) was at a disadvantage of being time consuming, with a low extraction yield [24]. Ultrasonication

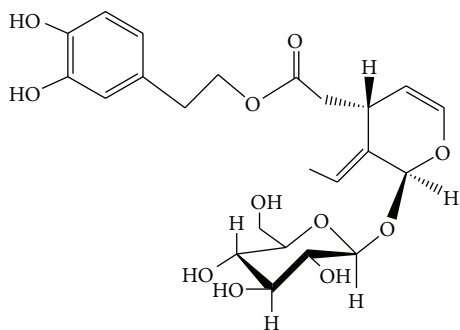


FIGURE 1: Chemical structure of oleuropein.

assisted extraction (UAE) could significantly improve the process due to oscillating and acoustic cavitation [25–27]. Additionally, reduced-pressure boiling extraction (RBE) was regarded as a relatively new extraction method, with process advantages of relatively low temperature requirements and high extraction effectiveness. Therefore, a combination of RBE and UAE (ultrasound-assisted extraction) was coupled for the extraction of oleuropein. To the best of our knowledge, ultrasound-assisted boiling extraction at reduced pressures (URPE) is being proposed for the first time and has not been investigated in the extraction of oleuropein from olive leaves.

In this paper, four important parameters, solvent, temperature, power, and the ratio of solid to liquid, were selected for optimization using response surface methodology (RSM) on the basis of a Box-Behnken design. In addition, visual evidence of the disruption of the cell wall by URPE was provided by SEM images obtained by a scanning electron microscope.

2. Materials and Methods

2.1. Materials. Olive leaves (*Frantoio*) were purchased from Wudu County, Gansu, China, and dried in their natural condition without sunlight. They were milled (40–60 mesh) by high-speed drug crusher and stored in the dry and dark location at room temperature. All chemical reagents were purchased by Nanjing Chemical Reagents Co., Ltd., in China. A 1200 W, 20 kHz ultrasonic generator (model FS-1200N, Shanghai Sonxi Co., Ltd., China) assembled with a probe transducer and a flat tip of 13.0 mm was used in the URPE experiments.

The HPLC equipment of Shimadzu Prominence LC-20A (Japan) was purchased from Shanghai Shimadzu Co., Ltd., in China. The HPLC system included a LC-20AT Solvent Delivery Unit, LC-20AT pump, 0–10 mL/min, a SPD-20A UV-VIS Detector, CBM-20Alite System Controller, LCsolution Single, Ver1.24 Workstation, and a 7725i Manual Sample Injector (Position Sensing Switch Incorporated) with a 20 μ L sample loop, Hamilton 702SNR (100 μ L). SEM was used to view surface structure of samples (model S-3400N, Hitachi High Technologies Corporation, Japan).

2.2. Methods

2.2.1. Reduced-Pressure Boiling Extraction Oleuropein Coupled with Ultrasound-Assist. In URPE experiments, a standard

ultrasonic probe with a flat tip of 13.0 mm in diameter was directly inserted into the mixture of olive leaves powder and extraction solvent and used as an ultrasonic source. The distance from flat top to flask bottom was controlled to about 3–5 mm. A small fraction of artificial zeolite was put into a three-mouth flask with the samples and solvent. The specimens were boiled and irradiated under a vacuum degree at 75 kPa and continuous ultrasonic waves for 3 min at a frequency of 20 kHz with different levels (0–1200 W) of output power. Meanwhile, the temperature was varied by the experiment and was controlled within $\pm 1^\circ\text{C}$. The treatment of the extract on oleuropein content was detected by HPLC.

2.2.2. Extraction Yield Equation. Consider

$$\text{Yield (\%)} = \frac{W_o}{W_t} \times 100\%, \quad (1)$$

where W_o is the content of oleuropein obtained from one extraction trial and W_t is the weight of the total raw mass of olive leaves.

2.2.3. HPLC Analysis. The HPLC conditions were set on the basis of Xie's method for the determination of oleuropein [28]. Isocratic elution was implemented with methanol-water solution of 40:60 (v/v) at a flow rate of 1 mL/min and the runs could be achieved in 15 min under 232 nm detection. The retention time for oleuropein was about 11.5 min. The method was precise, sensitive, and reproducible. Calibration for oleuropein was determined using the range from 1.06 to 10.6 μg in six intervals; and the equation developed was linear and could be expressed by the following formula:

$$Y = 163365 + 1305700X \quad (R^2 = 0.9992), \quad (2)$$

where X is the amount of standard used in calibration experiments and Y is the relevant peak area in HPLC chromatographs. R^2 is very close to 1, which means that there is a linear relationship between Y and X , and the equation is adequate for quantitative analysis.

2.2.4. SEM Imaging. Samples particles treated by URBE were placed into a silicon wafer special in SEM equipment and subsequently analyzed with the microscope. The samples were first sputtered and then coated with a thin layer of conductive gold at a thickness of 50–100 nm. The shape and surface characteristics of the samples were observed and digitally recorded.

2.2.5. Trials of RSM. Optimization trials of extracting oleuropein from olive leaves were carried out using RSM, which is used as a method of optimization incorporating interaction effect between factors. For this purpose, a four-factor and three-level Box-Behnken design consisting of 29 experimental runs was employed including 5 center point replicates [29]. Four independent variables of the design were temperature (X_1 , $^\circ\text{C}$), ultrasonic power (X_2 , W), ethanol concentration (X_3 , % (v/v, ethanol/water)), and the ratio of solid to liquid (X_4 , g/mL), and the response variable was the oleuropein extraction yield. In addition, the levels of the select factors

TABLE 1: Design of factors and levels coded table.

Independent variables	Units	Symbol	Coded levels		
			-1	0	1
Temperature	°C	X_1	40	50	60
Ultrasonic power	W	X_2	480	600	720
Ethanol concentration	% (v/v)	X_3	65	75	85
Ratio of solid to liquid	g/mL	X_4	1:20	1:30	1:40

TABLE 2: Design and results of the RSM.

Number	X_1 Extraction temperature	X_2 Ultrasonic power	X_3 Ethanol concentration	X_4 Ratio of solid to liquid	Yield/%
1	-1	-1	0	0	6.71
2	1	-1	0	0	6.77
3	-1	1	0	0	6.64
4	1	1	0	0	6.79
5	0	0	-1	-1	6.03
6	0	0	1	-1	5.95
7	0	0	-1	1	6.46
8	0	0	1	1	5.93
9	-1	0	0	-1	6.29
10	1	0	0	-1	6.39
11	-1	0	0	1	6.55
12	1	0	0	1	6.68
13	0	-1	-1	0	6.65
14	0	1	-1	0	6.81
15	0	-1	1	0	6.59
16	0	1	1	0	6.63
17	-1	0	-1	0	6.61
18	1	0	-1	0	6.59
19	-1	0	1	0	6.88
20	1	0	1	0	6.93
21	0	-1	0	-1	6.01
22	0	1	0	-1	5.91
23	0	-1	0	1	6.59
24	0	1	0	1	6.39
25	0	0	0	0	7.09
26	0	0	0	0	7.13
27	0	0	0	0	7.22
28	0	0	0	0	6.99
29	0	0	0	0	7.08

and the coding results were shown in Table 1. The design arrangement and the experimental results of the optimization design were displayed in Table 2. A second-order polynomial equation was used to fit the experimental data given in Table 2. The generalized model proposed for the response was given in the following equation:

$$Y_i = \beta_0 + \beta_1 X_1 + \beta_2 X_2 + \beta_3 X_3 + \beta_4 X_4 + \beta_{11} X_1^2 + \beta_{22} X_2^2 + \beta_{33} X_3^2 + \beta_{44} X_4^2$$

$$+ \beta_{12} X_1 X_2 + \beta_{13} X_1 X_3 + \beta_{14} X_1 X_4 + \beta_{23} X_2 X_3 + \beta_{24} X_2 X_4 + \beta_{34} X_3 X_4,$$

(3)

where Y_i is considered as predicted response value, β_0 is the value of fitting response at the center point of the design, β_i 's are the linear coefficients, β_i^2 's are the quadratic coefficients, and β_{ij} 's are the interaction coefficients, respectively. The

TABLE 3: The variance analysis and significance test table of regression coefficient of response surface design.

Source of variation	Degree of freedom	Sum of squares	Mean squares	F-test	P value
X_1	1	0.018	0.018	0.60	0.45
X_2	1	0.0019	0.0019	0.062	0.81
X_3	1	0.0048	0.0048	0.16	0.70
X_4	1	0.34	0.34	11.16	0.0049**
X_1X_2	1	0.0020	0.0020	0.066	0.80
X_1X_3	1	0.0012	0.0012	0.040	0.84
X_1X_4	1	0.0002	0.0002	0.0074	0.93
X_2X_3	1	0.0036	0.0036	0.12	0.74
X_2X_4	1	0.0025	0.0025	0.082	0.78
X_3X_4	1	0.051	0.051	1.66	0.22
X_1^2	1	0.026	0.026	0.85	0.37
X_2^2	1	0.34	0.34	11.32	0.0046**
X_3^2	1	0.52	0.52	17.21	0.0010**
X_4^2	1	2.69	2.69	88.36	<0.0001**
Model	14	3.41	0.24	7.99	0.0002**
Residual	14	0.43	0.03		
Lack of fit significant	10	0.40	5.72	0.053	0.0537
Pure error	4	0.028	0.0070		
Corrected total	28	3.83			

**Significant at 0.01.

computational software for this study was Design-Expert, version: 8.0.5.0, by Stat-Ease, Inc.

2.2.6. *Verification of the Optimal Conditions.* To check the validity of the model, the predicted value of the oleuropein yield was compared with the practical value under the optimal conditions, obtained by the second-order polynomial model of RSM.

3. Results and Discussion

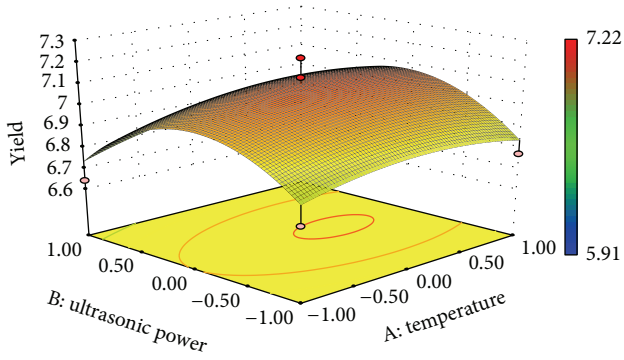
3.1. *Design and Results of RSM Experiments.* Four important factors, temperature, ultrasound power, ethanol concentration, and the ratio of solid to liquid, as well as the ranges of these four factors were selected to take the experiments of RSM to simulate a mathematic relationship about the four factors and oleuropein yield. The different variances of regression and significance were shown in Table 3. As it was shown in Table 3, X_4 , X_2^2 , X_3^2 , and X_4^2 were significant at level $P_{0.01}$, and the $F_{0.05}$ value for lack of fit indicated that the lack of fit was not significant. The model itself was significant at level $P_{0.01}$, which implied that the model was dependable. Thus, the fitted model was appropriate for describing the response surface. According to Table 3, a second-order polynomial equation for extraction yield of oleuropein was obtained for the factors coded as shown in the following equation:

$$Y = 7.10 + 0.039 X_1 - 0.012 X_2 - 0.020 X_3 + 0.17 X_4 + 0.022 X_1X_2 + 0.018X_1X_3 + 0.0075 X_1X_4 - 0.03 X_2X_3 - 0.025 X_2X_4 - 0.11$$

$$X_3X_4 - 0.063 X_1^2 - 0.23 X_2^2 - 0.28 X_3^2 - 0.64 X_4^2 \quad (R^2 = 0.89). \quad (4)$$

By means of F -test and P value, as it was shown in Table 3, it was seen that the quadratic term of the ratio of solid to liquid (X_4^2) had the most significant effect on the extraction yield of oleuropein, followed by the quadratic term of ethanol concentration (X_3^2), the quadratic term of ultrasonic power (X_2^2), and the ratio of solid to liquid (X_4).

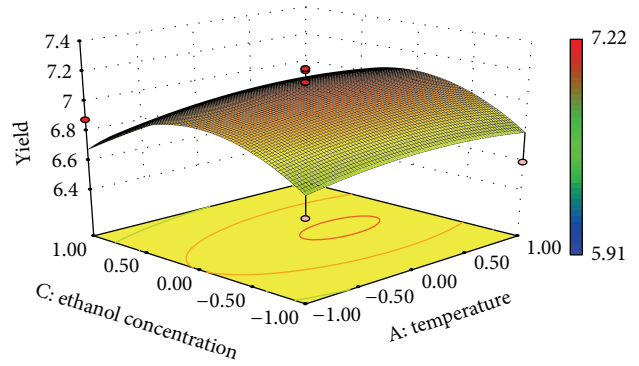
3.2. *Analysis of RSM Experiments.* As it was shown in Figure 2, six group graphs from the four factors were depicted by three-dimensional plots in order to illustrate the RSM problem. Two factors changed, while the other two were kept constant at zero, also called the central point. Figure 2(a) showed that the interactive effect between temperature and ultrasonic power was not significant and extraction yield increased when the temperature increased for all ultrasonic powers, while this law was not the same as ultrasonic power for all the temperatures. Optimal ultrasonic power 600 W could be the best of extraction yield for all the temperatures. Figure 2(b) displayed the interactive effects of temperature and ethanol concentration, and they also were not significant. When temperature was constant, extraction yield obtained 7.1% when ethanol concentration was 75%. The relationship of extraction temperature and the ratio of solid to liquid with extraction yield of oleuropein was shown in Figure 2(c). The results showed that extraction yield increased with the



Design-Expert? software
 Factor coding: coded
 Yield
 ● Design points above predicted value
 ○ Design points below predicted value

$X_1 = A$: temperature
 $X_2 = B$: ultrasonic power
 Coded factors
 C : ethanol concentration = 0.000
 D : ratio of solid to liquid = 0.000

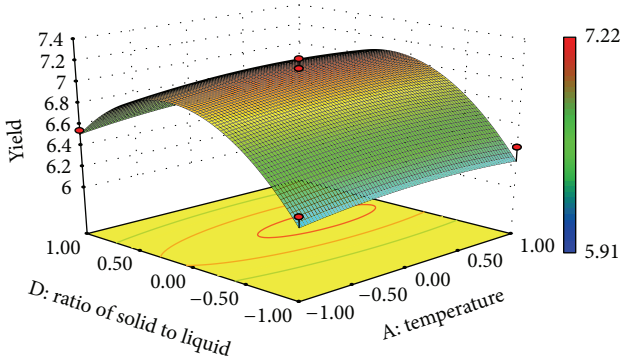
(a) Response surface showing effect of ultrasonic power and temperature



Design-Expert? software
 Factor coding: coded
 Yield
 ● Design points above predicted value
 ○ Design points below predicted value

$X_1 = A$: temperature
 $X_3 = C$: ethanol concentration
 Coded factors
 B : ultrasonic power = 0.000
 D : ratio of solid to liquid = 0.000

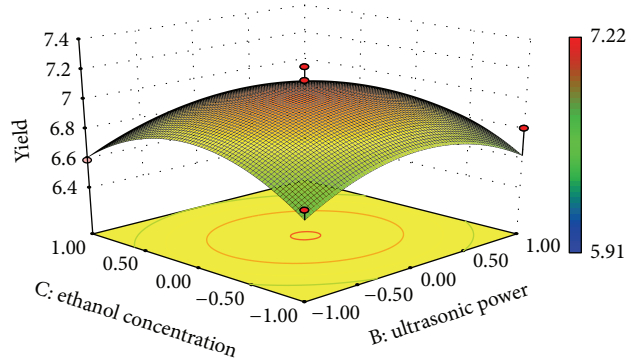
(b) Response surface showing effect of ethanol concentration and temperature



Design-Expert? software
 Factor coding: coded
 Yield
 ● Design points above predicted value
 ○ Design points below predicted value

$X_1 = A$: temperature
 $X_4 = D$: ratio of solid to liquid
 Coded factors
 B : ultrasonic power = 0.000
 C : ethanol concentration = 0.000

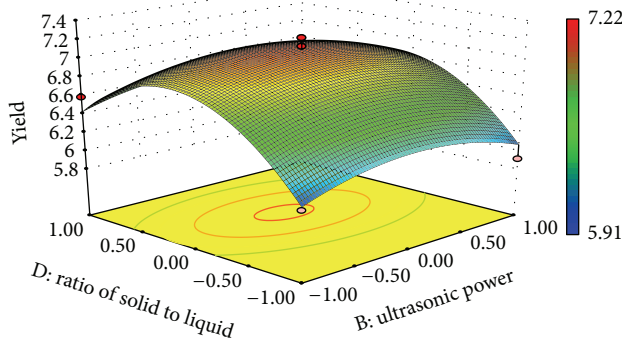
(c) Response surface showing effect of the ratio of solid to liquid and temperature



Design-Expert? software
 Factor coding: coded
 Yield
 ● Design points above predicted value
 ○ Design points below predicted value

$X_2 = B$: ultrasonic power
 $X_3 = C$: ethanol concentration
 Coded factors
 A : temperature = 0.000
 D : ratio of solid to liquid = 0.000

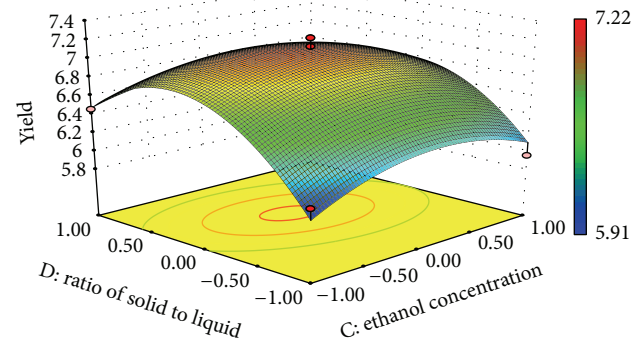
(d) Response surface showing effect of ethanol concentration and ultrasonic power



Design-Expert? software
 Factor coding: coded
 Yield
 ● Design points above predicted value
 ○ Design points below predicted value

$X_2 = B$: ultrasonic power
 $X_4 = D$: ratio of solid to liquid
 Coded factors
 A : temperature = 0.000
 C : ethanol concentration = 0.000

(e) Response surface showing effect of ultrasonic power and ratio of solid to liquid



Design-Expert? software
 Factor coding: coded
 Yield
 ● Design points above predicted value
 ○ Design points below predicted value

$X_3 = C$: ethanol concentration
 $X_4 = D$: ratio of solid to liquid
 Coded factors
 A : temperature = 0.000
 B : ultrasonic power = 0.000

(f) Response surface showing effect of ethanol concentration and ratio of solid to liquid

FIGURE 2: Response surface plot optimization of extraction yield between factors.

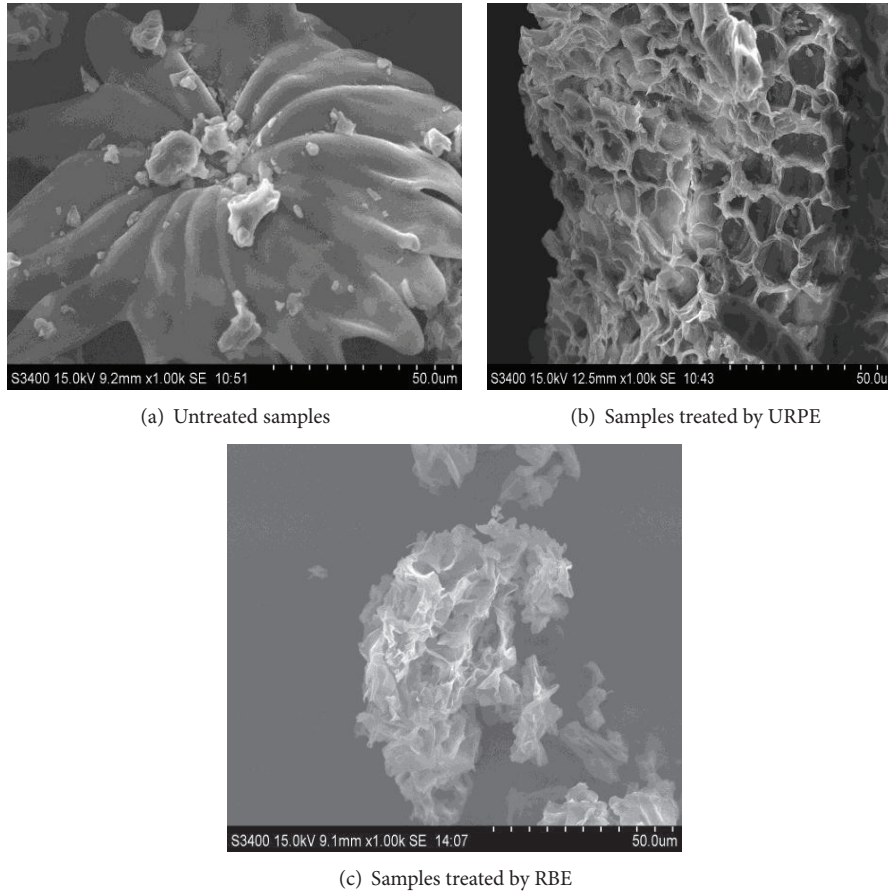


FIGURE 3: Displaying samples after being treated by URPE and RBE, compared with untreated ones.

increasing of the ratio up to 1:30, followed by decrease afterwards. From the graph it is also determined that the factor of the ratio of solid to liquid had a profound effect on the extraction yield. The interactive relationship between ultrasonic power and ethanol concentration was displayed in Figure 2(d). As the graph showed, extraction yield improved with the increase of ethanol concentration, followed by a slight decrease. The same situation was found with the ultrasonic power. Thus, ultrasonic power 600 W and 75% of ethanol concentration were optimal conditions for the extraction. Figure 2(e) showed the interactive relationship between ultrasonic power and the ratio of solid to liquid. The extraction yield almost formed a linear relationship with ultrasonic power and was not significant, while the yield displayed a quadratic relationship with the ratio of solid to liquid and was extremely significant. The relationship of ethanol concentration and the ratio of solid to liquid was shown in Figure 2(f). The effect of the ratio of solid to liquid was also significant as mentioned above and the ethanol concentration had an important influence on the extraction yield. From the graph, the optimal conditions were 75% ethanol concentration and a 1:30 solid to liquid ratio, respectively.

According to the calculation of software Design-Expert version 8.0.5.0, optimal conditions of extraction were obtained when temperature was at 53.1°C, ultrasonic power

599.8 W, ethanol concentration 74.5%, and the ratio of solid to liquid 1:31.4. Considering the practical operation, the final optimal conditions were revised to temperature: 53°C, ultrasonic power: 600 W, ethanol concentration: 75%, and the ratio of solid to liquid: 1:31.

3.3. Verification of the Results. Predicating optimal response values of the model for the suitability was tested by recommending the optimal conditions. The set of optimal conditions decided by RSM optimization method, together with the other two central points, extraction time 3 min, and vacuum degree 75 Kpa, were tested experimentally compared with the predicted value of extraction yield and with these optimal conditions, the predicted value of extraction yield of oleuropein was 7.121%, while the experimental value was 7.08% which was close to predicted value.

3.4. SEM of Olive Leaves after URPE. From the SEM, compared with Figure 3(a), the samples cell walls processed by URPE and RBE were broken, just as Figures 3(b) and 3(c) showed. The graphs obviously observed that the damage degree of the sample processed by URPE was stronger than that of RBE. One possible reason for the broken cell walls broken by URPE was that extraction solvent first infiltrated the cell wall and then produced boiling bubbles inside the cell when the outside conditions reached the boiling point of the

solvent. The continuous bubbling caused a cracking of cell walls. Also, UAE could create this physical effect in the cell wall, when coupled with the other extraction methods, where the samples were broken by the ceaseless shock.

4. Conclusions

In this paper, four important factors (i.e., extraction temperature, ultrasonic power, ethanol concentration, and the ratio of solid to liquid) were selected to carry out experimental optimization using Box-Behnken design. Based on the F -test analysis and P value results of RSM, the quadratic term of the ratio of solid to liquid (X_4^2) had the largest effect on oleuropein extraction yield. The optimization conditions were determined as follows: extraction temperature 53°C, ultrasonic power 600 W, ethanol concentration 75%, and the ratio of solid to liquid 1:31. With these optimized conditions, the experimental value of oleuropein extraction yield (7.08%) was very close to the predicted value of 7.121%. A second-order polynomial equation for extraction yield of oleuropein was obtained by expounding the following equation:

$$\begin{aligned}
 Y = & 7.10 + 0.039 X_1 - 0.012 X_2 - 0.020 \\
 & X_3 + 0.17 X_4 + 0.022 X_1 X_2 + 0.018 \\
 & X_1 X_3 + 0.0075 X_1 X_4 - 0.03 X_2 X_3 - 0.025 \\
 & X_2 X_4 - 0.11 X_3 X_4 - 0.063 X_1^2 - 0.23 \\
 & X_2^2 - 0.28 X_3^2 - 0.64 X_4^2 \\
 & (R^2 = 0.89)
 \end{aligned} \quad (5)$$

which fits the data well. In addition, the SEM images have provided excellent visual evidence of the effectiveness of URPE. Consequently, it is determined to be a feasible, efficient, and promising extraction technology for the extraction of bioactive ingredients from natural plants.

Conflict of Interests

The authors declare that there is no conflict of interests regarding the publication of this paper.

Acknowledgment

The authors acknowledge the financial support by funding project "948 items of introducing forestry special products using ultrasonic atomizing drying technology (2012-4-12)."

References

- [1] T. Huang, "Olive fruit production in the world," *World Agriculture*, vol. 3, pp. 29–30, 1998 (Chinese).
- [2] F. Kotti, E. Chiavaro, L. Cerretani, C. Barnaba, M. Gargouri, and A. Bendini, "Chemical and thermal characterization of Tunisian extra virgin olive oil from *Chetoui* and *Chemlali cultivars* and different geographical origin," *European Food Research and Technology*, vol. 228, no. 5, pp. 735–742, 2009.
- [3] O. Benavente-García, J. Castillo, J. Lorente, A. Ortuño, and J. A. del Rio, "Antioxidant activity of phenolics extracted from *Olea europaea* L. leaves," *Food Chemistry*, vol. 68, no. 4, pp. 457–462, 2000.
- [4] E. Altıok, D. Bayçın, O. Bayraktar, and S. Ülkü, "Isolation of polyphenols from the extracts of olive leaves (*Olea europaea* L.) by adsorption on silk fibroin," *Separation and Purification Technology*, vol. 62, no. 2, pp. 342–348, 2008.
- [5] F. Visioli, S. Bellosta, and C. Galli, "Oleuropein, the bitter principle of olives, enhances nitric oxide production by mouse macrophages," *Life Sciences*, vol. 62, no. 6, pp. 541–546, 1998.
- [6] F. Visioli and C. Galli, "Nikolaj Nikolajewitsch Anitschkow (1885–1964) established the cholesterol-fed rabbit as a model for atherosclerosis research," *Atherosclerosis*, vol. 135, no. 1, pp. 1–7, 1997.
- [7] N. K. Andrikopoulos, S. Antonopoulou, and A. C. Kaliora, "Oleuropein inhibits LDL oxidation induced by cooking oil frying by-products and platelet aggregation induced by platelet-activating factor," *Lebensmittel-Wissenschaft und-Technologie*, vol. 35, no. 6, pp. 479–484, 2002.
- [8] H. Jemai, M. Bouaziz, I. Feki, and S. Sayadi, "Hypolipidemic and antioxidant activities of oleuropein and its hydrolysis derivative-rich extracts from Chemlali olive leaves," *Chemico-Biological Interactions*, vol. 176, no. 2-3, pp. 88–98, 2008.
- [9] K. A. Nikolaos, A. Smaragdi, and C. K. Andriana, "Oleuropein inhibits LDL oxidation induced by cooking oil frying by-products and platelet aggregation induced by platelet-activating factor," *LWT-Food Science and Technology*, vol. 35, no. 6, pp. 479–484, 2002.
- [10] H. Jemai, M. Bouaziz, I. Feki, A. El Feki, and S. Sayadi, "Hypolipidemic and antioxidant activities of oleuropein and its hydrolysis derivative-rich extracts from Chemlali olive leaves," *Chemico-Biological Interactions*, vol. 176, no. 2-3, pp. 88–98, 2008.
- [11] I. Stupansa, M. Murrayb, A. Kirlicha, K. L. Tuck, and P. J. Hayball, "Inactivation of cytochrome P450 by the food-derived complex phenol oleuropein," *Food and Chemical Toxicology*, vol. 39, no. 11, pp. 1119–1124, 2001.
- [12] F. Visioli, G. Bellomo, G. Montedoro, and C. Galli, "Low density lipoprotein oxidation is inhibited in vitro by olive oil constituents," *Atherosclerosis*, vol. 117, no. 1, pp. 25–32, 1995.
- [13] S. Lee-Huang, L. Zhang, P. L. Huang, Y.-T. Chang, and P. L. Huang, "Anti-HIV activity of olive leaf extract (OLE) and modulation of host cell gene expression by HIV-1 infection and OLE treatment," *Biochemical and Biophysical Research Communications*, vol. 307, no. 4, pp. 1029–1037, 2003.
- [14] E. D. Clercq, "Chemotherapeutic approaches to the treatment of the acquired immune deficiency syndrome (AIDS)," *Journal of Medicinal Chemistry*, vol. 29, no. 9, pp. 1561–1569, 1986.
- [15] G. Q. Zhao, Z. F. Yin, and J. X. Dong, "Antiviral efficacy against hepatitis B virus replication of oleuropein isolated from *Jasminum officinale* L. var. *grandiflorum*," *Journal of Ethnopharmacology*, vol. 125, no. 2, pp. 265–268, 2009.
- [16] V. Micol, N. Caturla, L. Pérez-Fons, V. Más, L. Pérez, and A. Estepa, "The olive leaf extract exhibits antiviral activity against viral haemorrhagic septicaemia rhabdovirus (VHSV)," *Antiviral Research*, vol. 66, no. 2-3, pp. 129–136, 2005.
- [17] H. K. Hamdi and R. Castellon, "Oleuropein, a non-toxic olive iridoid, is an anti-tumor agent and cytoskeleton disruptor," *Biochemical and Biophysical Research Communications*, vol. 334, no. 3, pp. 769–778, 2005.

- [18] J. Han, N. Tallrete, P. Yamada, and H. Isoda, "Anti-proliferative and apoptotic effects of oleuropein and hydroxytyrosol on human breast cancer MCF-7 cells," *Cytotechnology*, vol. 59, no. 1, pp. 45–53, 2009.
- [19] I. Andreadou, M. Papaefthimiou, A. Zira et al., "Oleuropein restores the pathological metabolic pathways induced by doxorubicin's cardiotoxicity. An NMR based metabolomic study," *Journal of Molecular and Cellular Cardiology*, vol. 42, no. 6, supplement, pp. S168–S169, 2007.
- [20] H. F. Al-Azzawie and M. S. S. Alhamdani, "Hypoglycemic and antioxidant effect of oleuropein in alloxan-diabetic rabbits," *Life Sciences*, vol. 78, no. 12, pp. 1371–1377, 2006.
- [21] H. P. Fleming, W. M. Walter Jr., and J. L. Etchells, "Antimicrobial properties of oleuropein and products of its hydrolysis from green olives," *Applied and Environmental Microbiology*, vol. 26, no. 5, pp. 777–782, 1973.
- [22] L. M. Panizzi, J. M. Scarpatti, and E. G. Oriente, "The constitution of oleuropein, a bitter glucoside of the olive with hypotensive action," *Gazzetta Chimica Italiana*, vol. 90, pp. 1449–1485, 1960.
- [23] J. A. del Río, A. G. Báidez, J. M. Botía, and A. Ortuño, "Enhancement of phenolic compounds in olive plants (*Olea europaea* L.) and their influence on resistance against *Phytophthora* sp," *Food Chemistry*, vol. 83, no. 1, pp. 75–78, 2003.
- [24] E. Q. Xia, X. X. Ai, S. Y. Zang, T. T. Guan, X. R. Xu, and H. B. Li, "Ultrasound-assisted extraction of phillyrin from *Forsythia suspensa*," *Ultrasonics Sonochemistry*, vol. 18, no. 2, pp. 549–552, 2011.
- [25] F. Chemat and M. K. Khan, "Applications of ultrasound in food technology: processing, preservation and extraction," *Ultrasonics Sonochemistry*, vol. 18, no. 4, pp. 813–835, 2011.
- [26] N. Y. Yuhana, S. Ahmad, and A. R. Shamsul Bahri, "The effect of ultrasonic treatment on thermal stability of the cured epoxy/layered silicate nanocomposite," *Advances in Materials Science and Engineering*, vol. 2012, Article ID 789815, 5 pages, 2012.
- [27] T. Jerman, P. Trebše, and B. M. Vodopivec, "Ultrasound-assisted solid liquid extraction (USLE) of olive fruit (*Olea europaea*) phenolic compounds," *Food Chemistry*, vol. 123, no. 1, pp. 175–182, 2010.
- [28] P. J. Xie, L. X. Huang, C. H. Zhang, F. You, C. Z. Wang, and H. Zhou, "Optimization of ultrasound-assisted extraction of oleuropein from *Olea europaea* L. leaf using response surface methodology," *Natural Product Research and Development*, vol. 24, no. 7, 2012, (Chinese).
- [29] Z. X. Lin, H. M. Zhang, and J. P. Shi, "Characterization of ball milling pretreated corn stover and optimization enzymatic hydrolysis parameters," *Journal of Biobased Materials and Bioenergy*, vol. 7, no. 5, pp. 579–587, 2013.

Research Article

Microwave Assisted Hydrolysis of Holocellulose Catalyzed with Sulfonated Char Derived from Lignin-Rich Residue

Kui Wang,^{1,2,3} Xinfeng Xie,³ Zhan Si,¹ Jianchun Jiang,^{1,2} and Jingxin Wang³

¹*Institute of Chemical Industry of Forest Products, CAF, Nanjing 210042, China*

²*Research Institute for Forestry New Technology, CAF, Beijing 100091, China*

³*Division of Forestry and Natural Resources, West Virginia University, Morgantown, WV 26505, USA*

Correspondence should be addressed to Jianchun Jiang; bio-energy@163.com and Jingxin Wang; jxwang@wvu.edu

Received 26 September 2014; Revised 2 December 2014; Accepted 3 December 2014

Academic Editor: Jie Dai

Copyright © 2015 Kui Wang et al. This is an open access article distributed under the Creative Commons Attribution License, which permits unrestricted use, distribution, and reproduction in any medium, provided the original work is properly cited.

A microwave assisted green process has been developed for production of sugars through liquefying holocellulose catalyzed with sulfonated char derived from the lignin-rich residue produced during pretreatment of lignocellulose. Various reaction parameters including the hydrolysis temperature, hydrolysis time, catalyst content, and the ratio of water to feedstock were evaluated. The maximum sugars yield of 82.6% (based on the dry mass of holocellulose) was obtained under the optimum reaction conditions. The sulfonated char showed superior catalytic performance to that of dilute sulfuric acid in converting holocellulose into sugars under microwave irradiation.

1. Introduction

Hydrolysis of holocellulose (cellulose and hemicellulose) is a key technology to obtain the sugars which are pivotal platform compounds for a range of industrially important chemicals, such as ethanol, butanol, and hydrocarbon [1–3]. Substantial effort has been made to develop appropriate hydrolysis processes using liquid acids [4–6], enzymes [7, 8], supercritical water [9, 10], and solid catalysts [11–18] for hydrolysis of cellulose. Although liquid acid hydrolysis has received considerable attention and has been implemented on relatively large scales, the process is energy-inefficient, requiring separation, recycling, and treatment of the waste sulfuric acid. Enzymatic hydrolysis has been proven to be one of the most promising green hydrolysis technologies and operated in commercial applications. However, the high cost of enzymatic hydrolysis cannot be ignored. Supercritical water treatment for holocellulose hydrolysis has also received attention in recent years. The process, however, is carried out at extremely high temperatures and short residence time, causing partial degradation of the produced sugars [9, 10].

The move toward more environmentally benign processes has stimulated the development of solid acid catalysts, which

are nontoxic and easy in separation and have a high strength of acidity. Solid acid catalysts, including inorganic oxides [11], zeolites [12], cation-exchanged resins [13], polymers [14], and heteropolyacids [15], have been studied on the hydrolysis of cellulose. However, these heterogeneously catalytic processes show poor hydrolysis efficiency due to a mass transfer resistance between solid acids and the insoluble cellulose in water. Recently, Suganuma et al. [16], Wu et al. [17], and Gupta and Lee [18] have developed a carbonaceous solid acid bearing SO₃H, COOH, and phenolic hydroxyl (OH) groups in the framework of the amorphous carbon. This carbonaceous solid acid was proved to be an excellent candidate for the catalytic hydrolysis of cellulose. The amorphous carbon is a solid Bronsted acid catalyst consisting of flexible polycyclic carbon sheets with SO₃H, COOH, and phenolic hydroxyl (OH) groups in a three-dimensional network that can be readily prepared by partial carbonization of natural organic compounds, such as sugar, cellulose, and starch, followed by sulfonation of the resulting amorphous carbon [19].

In this study, we developed an environmentally benign hydrolysis approach for the saccharification of holocellulose. As shown in Figure 1, the green and effective hydrolysis process was catalyzed by a sulfonated char derived from

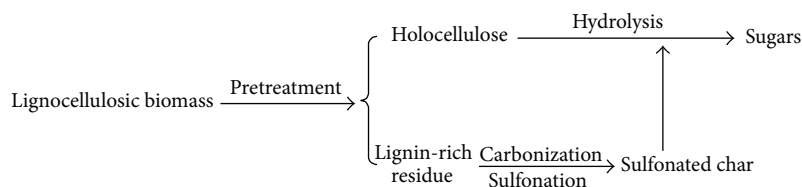


FIGURE 1: Schematic route of the holocellulose hydrolysis catalyzed by sulfonated char derived from lignin-rich pretreatment residues.

lignin-rich pretreatment residues with a small amount of water under microwave irradiation. After reaction, the catalyst can be easily separated from the products by filtration and effectively reused for further hydrolysis. This hydrolysis approach may also be employed as the guidance for efficient pretreatment and comprehensive utilization of lignocellulosic biomass.

2. Experimental

2.1. Materials. The hybrid poplar was collected from West Virginia University Experimental Forest. The holocellulose was separated from raw poplar particles and the composition of holocellulose was analyzed (mass percent: cellulose 63.2%, xylan 32.7%, and others 4.1%). Sulfuric acid and other chemicals (if applicable) were purchased from Sigma-Aldrich, Inc.

2.2. Preparation of Sulfonated Char. According to the typical procedure [18], the carbonaceous catalyst with SO_3H groups was prepared from the poplar (*Populus cathayana*) pretreatment residues (mass percent: lignin 65%, cellulose 25%, and others 10%). In a typical preparation procedure [19, 20], 30 g of the poplar pretreatment residue was heated for 5 h at 723 K under N_2 flow to produce a black solid, which was then ground into powder using universal high-speed smashing machine (QE-500, Zhejiang Yili Industry and Trade Co. Ltd.). 10 g of the powder was then boiled in fuming sulfuric acid (15 wt% SO_3) at 353 K under N_2 for 8 h. After cooling to room temperature, the suspension was filtered using cellulose filter paper (pore size of 30–50 μm) to yield a black precipitate that was washed repeatedly with hot distilled water (>353 K) until no sulfate ions could be detected. The washed precipitate was dried at 383 K for 12 h to obtain a sulfonated char bearing SO_3H , OH, and COOH groups.

2.3. Characterization of Sulfonated Char. The specific surface area of the sulfonated char was obtained by Brunauer Emmett Teller surface analyzer (BET, ASAP2020M, Micromeritics). Scanning electron microscopy (SEM) analysis was conducted on a Hitachi 3400-1 electronic microscope working at 30 kv. FTIR spectrum was recorded on a Fourier transform infrared spectroscopy (FTIR, I80, Nicolet) using the standard KBr disc method. The samples were scanned between 400 and 4000 cm^{-1} with a resolution of 0.4 cm^{-1} . X-ray diffraction (XRD) patterns were collected on a Bruker D8 Focus Advance diffractometer using Cu $\text{K}\alpha$ radiation (wavelength $\lambda = 1.5406 \text{ \AA}$). According to the FT-IR analysis result, the sulfonated char possesses three functional groups: SO_3H , COOH, and phenolic OH. The amount of groups

was estimated by elemental analysis (EA, Thermo Scientific Flash 2000 CHNS/O) and cation-exchange analysis [16]. The densities of SO_3H groups were estimated based on the sulfur content determined from sample compositions obtained by elemental analysis. The total $\text{SO}_3\text{H} + \text{COOH}$ and $\text{SO}_3\text{H} + \text{COOH} + \text{OH}$ contents were estimated from the exchange of Na^+ in aqueous NaCl and NaOH solutions, respectively.

2.4. Hydrolysis of Holocellulose and Analysis of the Produced Sugars. The holocellulose was separated from raw poplar (*Populus cathayana*) particles [18]. In a typical experimental run, 0.2 g oven-dried holocellulose powder and 0.2 g carbonaceous catalyst were mixed and milled for 10 minutes in an agate mortar and then placed into a Pyrex tube. Distilled water (3 mL) was then added to the powdered mixture before the Pyrex tube was sealed and placed in a microwave reactor (CEM, Discovers). The mixture was stirred by a magnetic stirrer during the reaction. After the desired reaction time, the reaction mixture was neutralized with 0.4 mol/L of NaOH solution (10 mL) and filtered with filter paper (pore size of 30–50 μm).

The aqueous filtrate was analyzed using the Dionex Capillary Ion Chromatography System (ICS5000 Thermo Fisher) with a pulsed amperometric detector and a CarboPac PA-10 (4 mm) column. NaOH (18 mM) aqueous solution was used as elution solvent at a flow rate of 1.0 mL min^{-1} . The yield of total sugars (based on the dry mass of holocellulose) was calculated using the following equation: Total sugars yield (%) = [amount (g) of oligose + amount (g) of monose]/amount (g) of holocellulose.

The catalytic performance of the sulfonated char was examined by the microwave assisted hydrolysis of holocellulose under various conditions. The experimental parameters were evaluated as follows: hydrolysis temperature from 373 K to 403 K, reaction time from 20 min to 100 min, catalyst/substrate (holocellulose) ratio from 0.25 to 1.5, and liquid/solid (catalyst + holocellulose) ratio from 2.5 to 12.5. The reusability of the sulfonated char was also studied and the respective catalytic performance was compared with that of dilute sulfuric acid.

3. Results and Discussion

3.1. Properties of the Sulfonated Char. The BET analysis showed that the specific surface area of sulfonated char was 2 $\text{m}^2 \text{g}^{-1}$, which is in the range of a typical lignin carbon processed at similar temperatures [21]. The SEM analysis (Figure 2(a)) showed that the sulfonated char particles exhibited an irregular morphology with the particle size

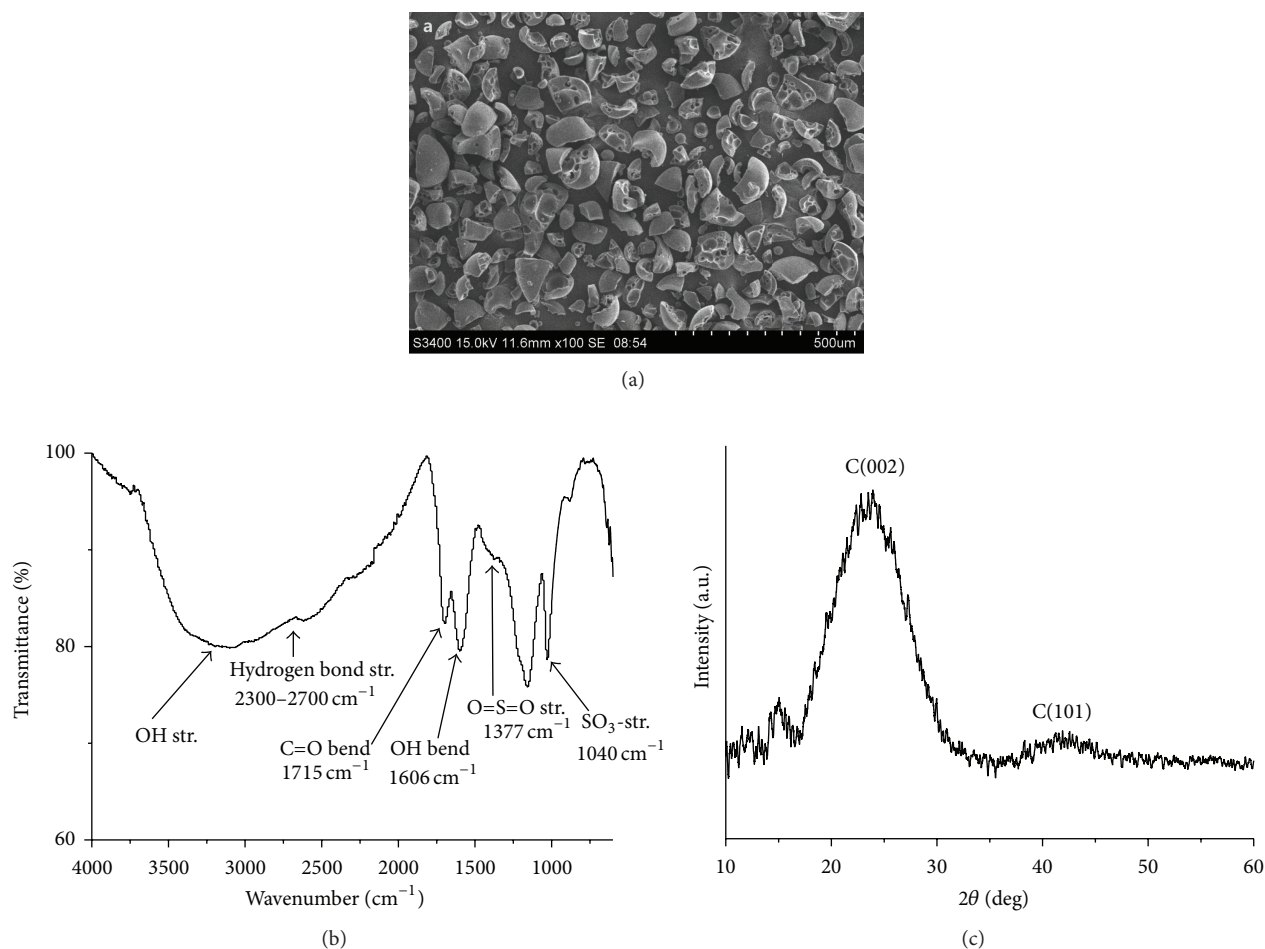


FIGURE 2: The SEM image (a), FTIR spectrum (b), and XRD pattern (c) for the prepared sulfonated char.

ranging from 30 to 100 μm . The FTIR spectrum (Figure 2(b)) showed two vibration bands at 1040 cm^{-1} (SO_3 -stretching) and 1377 cm^{-1} ($\text{O}=\text{S}=\text{O}$ stretching in SO_3H) which verified the existence of SO_3H groups. The vibration bands at 1606 cm^{-1} ($-\text{OH}$) and 1715 cm^{-1} ($\text{C}=\text{O}$) can be assigned to the $-\text{COOH}$ groups in the sulfonated char. The broadband at $2300\text{--}2700\text{ cm}^{-1}$ suggested an overtone (Fermi resonance) of the bending mode of strong hydrogen bond [16]. The XRD pattern (Figure 2(c)) of the sulfonated char exhibited two broad diffraction peaks at 22.5° and 42.0° of 2θ , which is typical for amorphous carbon composed of aromatic carbon sheets oriented in a considerably random pattern [22]. Elemental analysis results (C 53.745; H 3.389; O 37.868; S 4.998) and cation-exchange experiment revealed that the samples composition is $\text{CH}_{0.757}\text{O}_{0.528}\text{S}_{0.034}$ and that the amounts of SO_3H , COOH , and phenolic OH groups bonded to the char are 1.53, 0.30, and 1.69 mmol g^{-1} , respectively.

3.2. Hydrolysis of Holocellulose under Microwave Irradiation. As shown in Figure 3, the sugar yield of holocellulose increased with increasing reaction temperature in the first

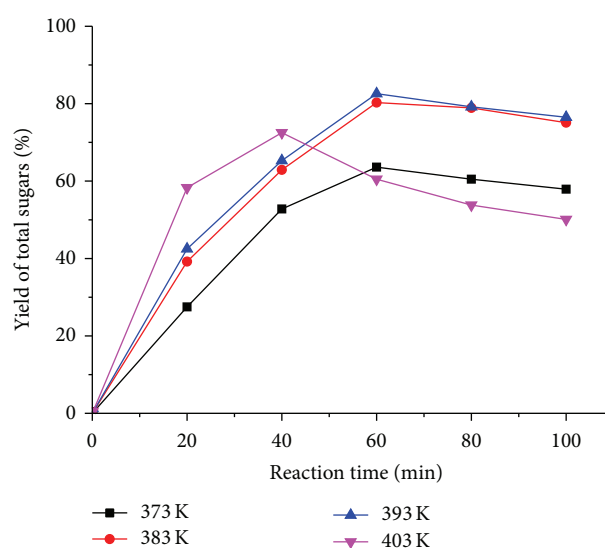


FIGURE 3: Effect of reaction temperature on the sulfonated char catalyzed hydrolysis of holocellulose. Reaction conditions: 0.2 g holocellulose, 0.2 g catalyst, 3 mL H_2O , and microwave irradiation (300 W) for 60 min.

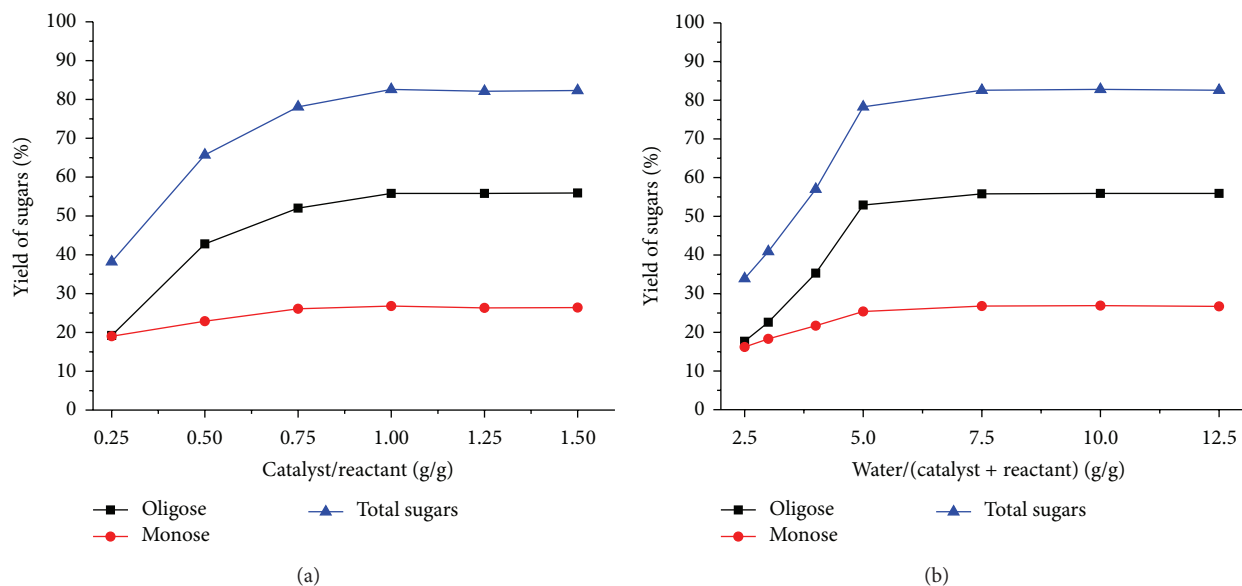


FIGURE 4: (a) Effect of catalyst/substrate ratio on the sulfonated char catalyzed hydrolysis of holocellulose. Reaction conditions: 0.2 g holocellulose, 3 mL H₂O, 393 K, and microwave irradiation (300 W) for 60 min. (b) Effect of liquid/solid ratio on the sulfonated char catalyzed hydrolysis of holocellulose. Reaction conditions: 0.2 g holocellulose, 0.2 g catalyst, 393 K, and microwave irradiation (300 W) for 60 min.

40 minutes of the reaction. However, it started to decrease with longer reaction time, indicating thermal degradation of monose at elevated temperature. The highest sugar yield of 82.6% was obtained when the holocellulose was treated at 393 K for 60 minutes. This optimum reaction temperature and reaction time were used in our studies on other reaction parameters. The results indicated that saccharification of the polysaccharides and thermal degradation of the produced monose and oligose were taking place synchronously in the reaction system.

The effects of catalyst/substrate (holocellulose) ratio and liquid/solid (catalyst + holocellulose) ratio were evaluated using the optimal reaction temperature and time. As shown in Figure 4(a), the yield of monose and oligose increased with increasing catalyst/substrate ratio up to 1.00. Increasing the liquid/solid ratio significantly increased the sugar yield when the ratio was lower than 5.0 as shown in Figure 4(b). No further increase in the sugar yield was apparent for liquid/solid ratios above 7.5.

To evaluate reusability, sulfonated char samples (reused up to three times) were investigated by reacting a mixture of 0.2 g catalyst, 0.2 g holocellulose, and 3 mL water under 300 W microwave irradiation for 60 min. The unreacted sulfonated char and those recovered once, twice, and 3 times were designated SC0, SC1, SC2, and SC3, respectively. Additionally, the catalytic performance of the sulfonated char was compared with that of dilute sulfuric acid. After the first run at 393 K for 60 min, the sulfonated char was recovered from the hydrolytic solution by filtration followed by washing with distilled water. The recovered catalyst was reused by directly mixing with fresh holocellulose and water. As shown in Table 1, the catalytic performance of the sulfonated char decreased with the recovery times, indicating reduced active sites on the surface of the sulfonated char. It is possible that

TABLE 1: Comparison of the catalytic performance of reused sulfonated char and dilute sulfuric acid.

Yield/%	SC0 ^a	SC1 ^a	SC2 ^a	SC3 ^a	H ₂ SO ₄ ^a	H ₂ SO ₄ ^b
Monose	26.8	23.9	20.4	16.1	12.2	4.9
Oligose	55.8	54.6	52.5	49.1	10.3	27.2
Sugars	82.6	78.5	72.9	65.2	22.5	31.7

^aReaction at 393 K; ^breaction at 423 K.

some active acid sites were blocked by the unreacted holocellulose residues left in aqueous solution [18, 23]. However, even after being recovered three times, the sulfonated char still has much higher catalytic ability than dilute sulfuric acid in hydrolysis of holocellulose. The poor performance of dilute sulfuric acid in hydrolysis of holocellulose was attributed to the low catalytic activity at 393 K and the degradation of produced sugars when high temperature (423 K or more) was employed.

4. Conclusions

An environmentally friendly hydrolysis process alternative to dilute sulfuric acid was developed to efficiently convert holocellulose into useful sugars under microwave irradiation. The catalyst, a sulfonated char, was produced from lignin-rich residues from pretreatment of lignocellulosic biomass. The catalyst showed excellent catalytic performance in hydrolysis of holocellulose and low toxicity for microbial activity, which is different from sulfuric acid. This approach may also be exploited for the direct hydrolysis of lignocellulosic biomass into sugars and other useful chemicals.

Conflict of Interests

The authors declare that there is no conflict of interests regarding the publication of this paper.

Acknowledgment

This work was supported by National Nonprofit Institute Research Grant of CAFINT2013C05.

References

- [1] A. J. Ragauskas, C. K. Williams, B. H. Davison et al., "The path forward for biofuels and biomaterials," *Science*, vol. 311, no. 5760, pp. 484–489, 2006.
- [2] J. N. Chheda, G. W. Huber, and J. A. Dumesic, "Liquid-phase catalytic processing of biomass-derived oxygenated hydrocarbons to fuels and chemicals," *Angewandte Chemie-International Edition*, vol. 46, no. 38, pp. 7164–7183, 2007.
- [3] Y.-B. Huang and Y. Fu, "Hydrolysis of cellulose to glucose by solid acid catalysts," *Green Chemistry*, vol. 15, no. 5, pp. 1095–1111, 2013.
- [4] G. Sanchez, L. Pilcher, C. Roslander, T. Modig, M. Galbe, and G. Liden, "Dilute-acid hydrolysis for fermentation of the Bolivian straw material Paja Brava," *Bioresource Technology*, vol. 93, no. 3, pp. 249–256, 2004.
- [5] P. Lenihan, A. Orozco, E. O'Neill, M. N. M. Ahmad, D. W. Rooney, and G. M. Walker, "Dilute acid hydrolysis of lignocellulosic biomass," *Chemical Engineering Journal*, vol. 156, no. 2, pp. 395–403, 2010.
- [6] A. S. Amarasekara and B. Wiredu, "Aryl sulfonic acid catalyzed hydrolysis of cellulose in water," *Applied Catalysis A: General*, vol. 417–418, pp. 259–262, 2012.
- [7] B. Yang, Z. Y. Dai, S. Y. Ding, and C. E. Wyman, "Enzymatic hydrolysis of cellulosic biomass," *Biofuels*, vol. 2, no. 4, pp. 421–450, 2011.
- [8] D. Kumar and G. S. Murthy, "Stochastic molecular model of enzymatic hydrolysis of cellulose for ethanol production," *Biotechnology for Biofuels*, vol. 6, no. 1, article no. 63, 2013.
- [9] M. Sasaki, Z. Fang, Y. Fukushima, T. Adschiri, and K. Arai, "Dissolution and hydrolysis of cellulose in subcritical and supercritical water," *Industrial and Engineering Chemistry Research*, vol. 39, no. 8, pp. 2883–2890, 2000.
- [10] K. Ehara and S. Saka, "A comparative study on chemical conversion of cellulose between the batch-type and flow-type systems in supercritical water," *Cellulose*, vol. 9, no. 3–4, pp. 301–311, 2002.
- [11] T. Zhang, N. Ji, M. Y. Zheng, and J. G. Chen, "Uses of aluminum oxides supported noble metal catalyst in cellulose hydrogenation hydrolyzation," CN Patent 101428214, 2007.
- [12] Z. H. Zhang and Z. B. Zhao, "Solid acid and microwave-assisted hydrolysis of cellulose in ionic liquid," *Carbohydrate Research*, vol. 344, no. 15, pp. 2069–2072, 2009.
- [13] R. Rinaldi, R. Palkovits, and F. Schuth, "Depolymerization of cellulose using solid catalysts in ionic liquids," *Angewandte Chemie International Edition*, vol. 47, no. 42, pp. 8047–8050, 2008.
- [14] G. Akiyama, R. Matsuda, H. Sato, M. Takata, and S. Kitagawa, "Cellulose hydrolysis by a new porous coordination polymer decorated with sulfonic acid functional groups," *Advanced Materials*, vol. 23, no. 29, pp. 3294–3297, 2011.
- [15] K.-I. Shimizu, H. Furukawa, N. Kobayashi, Y. Itaya, and A. Satsuma, "Effects of Brønsted and Lewis acidities on activity and selectivity of heteropolyacid-based catalysts for hydrolysis of cellobiose and cellulose," *Green Chemistry*, vol. 11, no. 10, pp. 1627–1632, 2009.
- [16] S. Suganuma, K. Nakajima, M. Kitano et al., "Hydrolysis of cellulose by amorphous carbon bearing SO₃H, COOH, and OH groups," *Journal of the American Chemical Society*, vol. 130, no. 38, pp. 12787–12793, 2008.
- [17] Y. Y. Wu, Z. H. Fu, Q. Xu, F. Liu, C. L. Lu, and L. Q. Mao, "Microwave-assisted hydrolysis of crystalline cellulose catalyzed by biomass char sulfonic acids," *Green Chemistry*, vol. 12, no. 4, pp. 696–700, 2010.
- [18] R. Gupta and Y. Y. Lee, "Pretreatment of hybrid poplar by aqueous ammonia," *Biotechnology Progress*, vol. 25, no. 2, pp. 357–364, 2009.
- [19] Y. Jiang, X. Li, X. Wang et al., "Effective saccharification of lignocellulosic biomass over hydrolysis residue derived solid acid under microwave irradiation," *Green Chemistry*, vol. 14, no. 8, pp. 2162–2167, 2012.
- [20] E. T. Lu and S. G. Love, "Gravitational tractor for towing asteroids," *Nature*, vol. 438, no. 7065, pp. 177–178, 2005.
- [21] X. Xie, B. Goodell, D. Zhang et al., "Characterization of carbons derived from cellulose and lignin and their oxidative behavior," *Bioresource Technology*, vol. 100, no. 5, pp. 1797–1802, 2009.
- [22] N. Tsubouchi, C. Xu, and Y. Ohtsuka, "Carbon crystallization during high-temperature pyrolysis of coals and the enhancement by calcium," *Energy and Fuels*, vol. 17, no. 5, pp. 1119–1125, 2003.
- [23] X. Tian, F. Su, and X. S. Zhao, "Sulfonated polypyrrole nanospheres as a solid acid catalyst," *Green Chemistry*, vol. 10, no. 9, pp. 951–956, 2008.

Research Article

Effect of Heating at Oven-Dry State on Steam Treated Bamboo Powder Thermal Fluidity

S. Kajikawa and T. Iizuka

Department of Mechanical and System Engineering, Kyoto Institute of Technology, Matsugasaki-goshokaido-cho, Sakyo-ku, Kyoto 606-8585, Japan

Correspondence should be addressed to S. Kajikawa; d3821003@edu.kit.ac.jp

Received 20 February 2015; Revised 8 June 2015; Accepted 30 July 2015

Academic Editor: Jiang Jianchun

Copyright © 2015 S. Kajikawa and T. Iizuka. This is an open access article distributed under the Creative Commons Attribution License, which permits unrestricted use, distribution, and reproduction in any medium, provided the original work is properly cited.

In hot molding processes of woody material, it is important to understand the effect of oven-dry heating on the property of woody biomass material, such as thermal fluidity. In this study, thermal flow tests of untreated and steam treated bamboo powder were conducted to investigate the effects of heating at an oven-dry state on thermal fluidity. The test temperature was set to 200°C. Before the thermal flow test, powder was dry-heated in a capillary rheometer at 200°C with a variable heating time. Thermogravimetry was conducted to understand the thermal changes of the powder during an increasing temperature and constant temperature. Fluidity of untreated powder was improved with a short dry-heating but decreased with a long dry-heating. In contrast, steam treated powder fluidity was high compared to untreated one, but its fluidity did not improve from dry-heating. From these thermogravimetry results, the chemical changes associated with component volatilization relate with the thermal fluidity. Therefore, the decrease in fluidity from dry-heating occurred because fluidity related components escape from the powder through volatilization.

1. Introduction

Effective use of woody biomass resources is environmentally friendly because woody biomass resources are carbon neutral and sustainable. However, applications for woody biomass materials are limited because of some inherent practicality issues. One issue is material workability. Woody biomass is generally processed through machining, bending, or compacting. However, processing complex shapes is difficult, and some problems, such as limited extraction rates and productivity, exist with these methods.

In order to resolve these problems, various research studies on woody material processing methods have been conducted. For example, wood plastic composites (WPC), which are made by mixing woody materials and plastics, can be processed with general plastic processing methods such as extrusion or injection molding [1–3]. Methods where petroleum-derived materials were not used have also been developed. It was reported that molding of only woody materials containing water was possible at 170–180°C because

woody materials have thermal fluidity and self-adhesiveness due to the hydrolysis of the material's chemical components [4–6]. In addition, it was reported that thermal fluidity and self-adhesiveness could be improved by steam treatment [7–10]. It is considered that these woody properties changes occur due to water soluble components increasing with the hydrolysis of the materials chemical components, such as hemicellulose, during steam treatment [11–13]. Injection molding is possible without water by using steam treated woody powder, and strength of injection molded product came up to that of polypropylene [14, 15]. This way, thermal fluidity of woody material can be controlled for the improvement of moldability by heating at the wet state, such as steaming.

Woody material properties are affected by heating not only during the wet state, such as steaming, but also during the dry state. For example, research about woody material dry-heating has shown that dynamic viscoelastic properties of dry wood change in relation to its heating temperature or time [16]. In addition, thermal changes to the physical

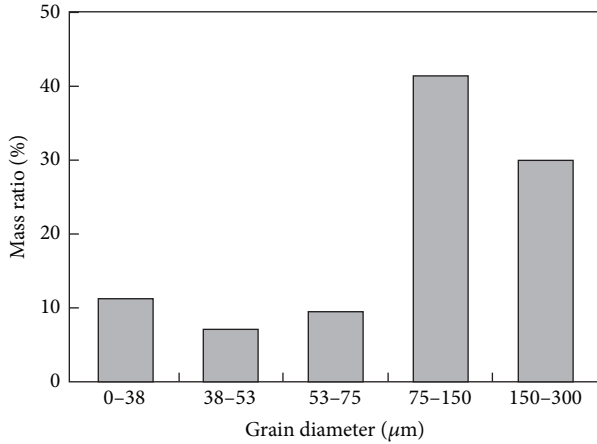


FIGURE 1: Particle size distribution of bamboo powder.

property, such as thermal softening, in the dry state are different from those in the wet state [10, 17]. Accordingly, it is possible that the thermal flowability of woody material is affected by dry-heating. However, the effect of dry-heating on the thermal fluidity of woody material is not fully understood. For actual hot molding processes for woody material, it is important to understand these effects.

In this study, a thermal flow test for woody materials dry-heated for different treating time was conducted using a capillary rheometer. Bamboo powder, which was untreated or steam treated, was studied because an effective use of the timber from bamboo thinning is desired in Japan [18]. In addition, it was reported that bamboo fluidity is high compared to other woody materials [19]. This reason is the fact that hemicellulose of bamboo is mainly xylan [20] and xylan having acetyl group produces acid which catalyzes hydrolysis [12]. Thermogravimetry for bamboo powder was conducted in order to investigate the thermal change effects during dry-heating. From these results, the relationship between thermal fluidity and chemical changes in bamboo powder during dry-heating is discussed.

2. Materials and Methods

2.1. Preparation of the Materials. Moso bamboo powder was used. To obtain the powder, a stem was shaved and shavings were then milled in a pin mill. The powder passed through a $\phi 300 \mu\text{m}$ screen during the milling stage. Figure 1 shows the powder particle size distribution, which was predominately in the range of 75–300 μm .

Figure 2 shows a schematic diagram of the bamboo powder steam treatment. The powder was treated with saturated water vapor at a high temperature by heating a small pressure vessel containing the powder and water. First, the vessel was heated to a target temperature of T_s ($^{\circ}\text{C}$). Next, the temperature T_s was held for a predefined time t_s (min). The vessel was then cooled to 100°C . The powder was tapped off from the vessel and air-dried at room temperature. Air-dried powder was dried additionally in an oven at constant 105°C to achieve an oven-dry state before the thermal flow test.

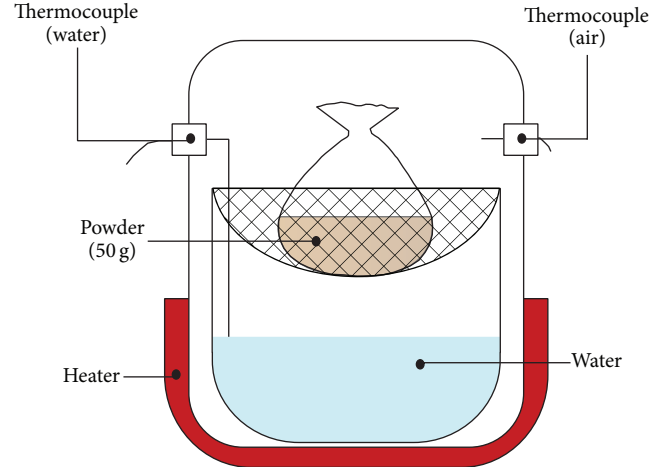


FIGURE 2: Schematic diagram of steam treatment.

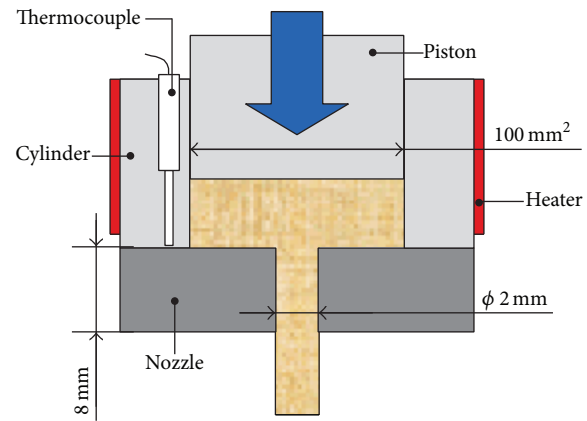


FIGURE 3: Schematic diagram of the capillary rheometer.

2.2. Thermal Flow Test. A capillary rheometer (CFT-500D, Shimadzu) was used to dry-heat the powder and for the thermal flow test. Figure 3 shows a schematic diagram of the capillary rheometer. First, the capillary rheometer was heated to a test temperature of 200°C because bamboo fluidity is activated at 200°C [4]. Powder with a mass of 1.5 g was placed in the cylinder followed by a piston. The powder was then heated for a predefined time t_h (min) in the cylinder. The piston was compressed at 49 MPa and material was extruded from the nozzle. The piston movement during the material extrusion was evaluated.

2.3. Thermogravimetry. Thermogravimetry was conducted with a thermogravimetry/differential thermal analyzer (TG/DTA 6200, Seiko Instruments Inc.). The air-dried bamboo powder was placed in an aluminum pan, and an empty aluminum pan was used as a reference. Figure 4 shows the temperature program. First, drying at 105°C for 30 min with a dry nitrogen gas purge was performed to ensure that moisture state of the powder was oven-dry in the device. The temperature was raised to 200°C at a constant rate of $10^{\circ}\text{C}/\text{min}$ and held for 60 min. Changes in mass loss rate

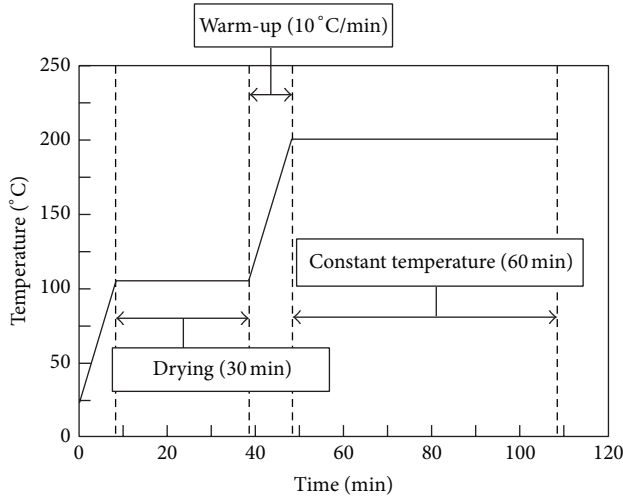


FIGURE 4: Thermogravimetry temperature schedule.

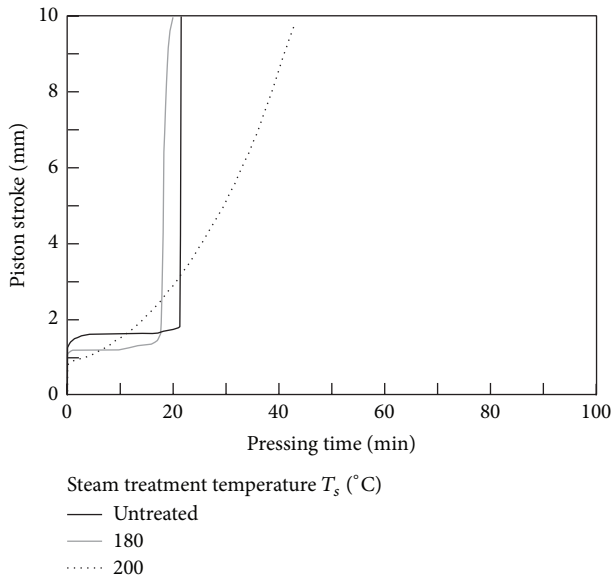


FIGURE 5: Effect of steam treatment temperature T_s on the thermal flow curve. ($t_s = 20$ min and $t_h = 5$ min).

(%/min) based on the oven-dry mass were evaluated during the warm-up period and the constant temperature period.

3. Results and Discussion

3.1. Thermal Flow Curve of Untreated and Steam Treated Bamboo Powder. Flow behavior of untreated and steam treated bamboo powder was investigated. Figure 5 shows the relationship between press time and piston stroke motion when the steam temperature T_s was changed. The steam treatment time t_s was set at 20 min and the heating time t_h was set at 5 min. It was considered that the powder temperature achieved 200 °C with a 5 min heating interval because we confirmed that the temperature of the powder near the surface was 200 °C after 3-4 min.

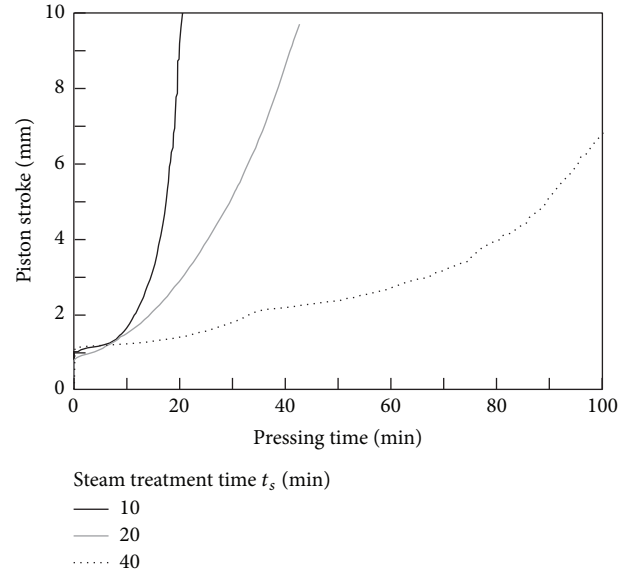


FIGURE 6: Effect of steam treatment time t_h on the thermal flow curve. ($T_s = 200$ °C and $t_h = 5$ min).

As shown in Figure 5, the untreated and $T_s = 180$ °C powder did not flow immediately but rapidly increased in rate when the pressing time reached about 20 min. It was determined that the fluidity was provided by thermal decomposition from heat caused by the piston pressure. Gas is exhausted during thermal decomposition of wood biomass material [21], but it is difficult for the gas to escape from the cylinder until the flow starts because the powder is in a high pressure state. Therefore, the material flowed drastically when the gas could escape once the flow started. In contrast, the $T_s = 200$ °C powder flowed immediately once pressed but at a slower flow rate. Accordingly, it was determined that powder fluidity is simple to increase because the powder has flow components produced by the preliminary steam treatment. In addition, a rapid flow rate increase could not have occurred because the gas was able to escape gradually with material flow.

Figure 6 shows the relationship between pressing time and piston stroke motion when the steaming time t_s was changed. In this experimental series, T_s was set at 200 °C because flow behavior changed largely with a steam treatment of 200 °C, as shown in Figure 5. The flow rate slows with an increase in t_s . This result suggests that a long steam treatment has a negative effect on thermal fluidity.

3.2. Effects of Dry-Heating Time on the Bamboo Powder Thermal Flow Curve. Figure 7 shows the thermal flow curve changes for each powder by dry-heating time t_h . The range of t_h tested was from 1 to 20 min. For untreated powder, flow started sooner when t_h increased from 1 to 5 min, but the start was delayed with a further increase in t_h over 5 min as shown in Figure 7(a). In contrast, for steam treated powder, the flow began soonest when t_h was 1 min, while the flow start was delayed with an increase in t_h as shown in Figures 7(b)–7(e). In particular, powder steam treated at 200 °C for 10 and 20 min had no flow when t_h was 20 min and that for 40 min had no

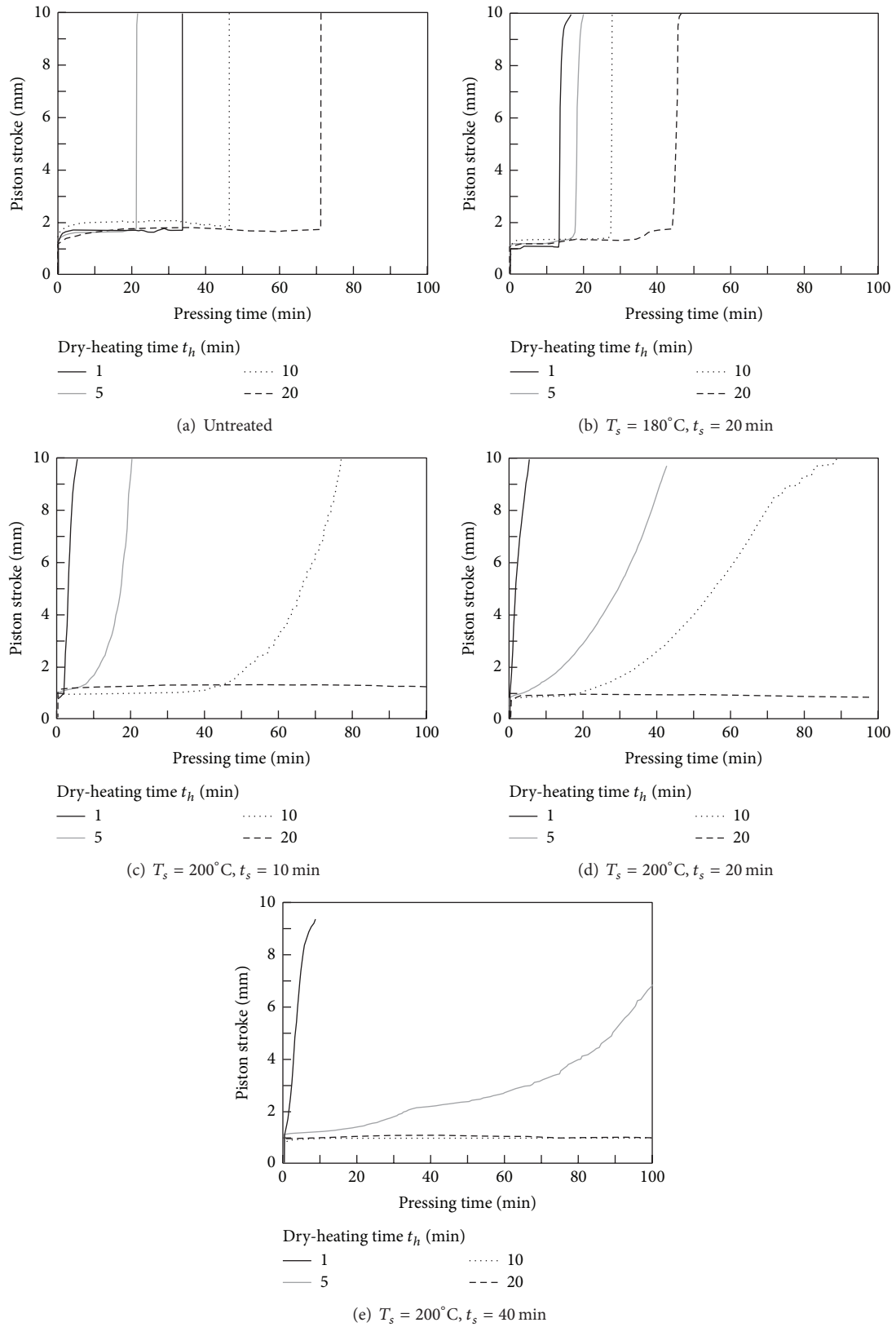


FIGURE 7: Effect of dry-heating time t_h on the thermal flow curve when the steam treatment temperature is changed.

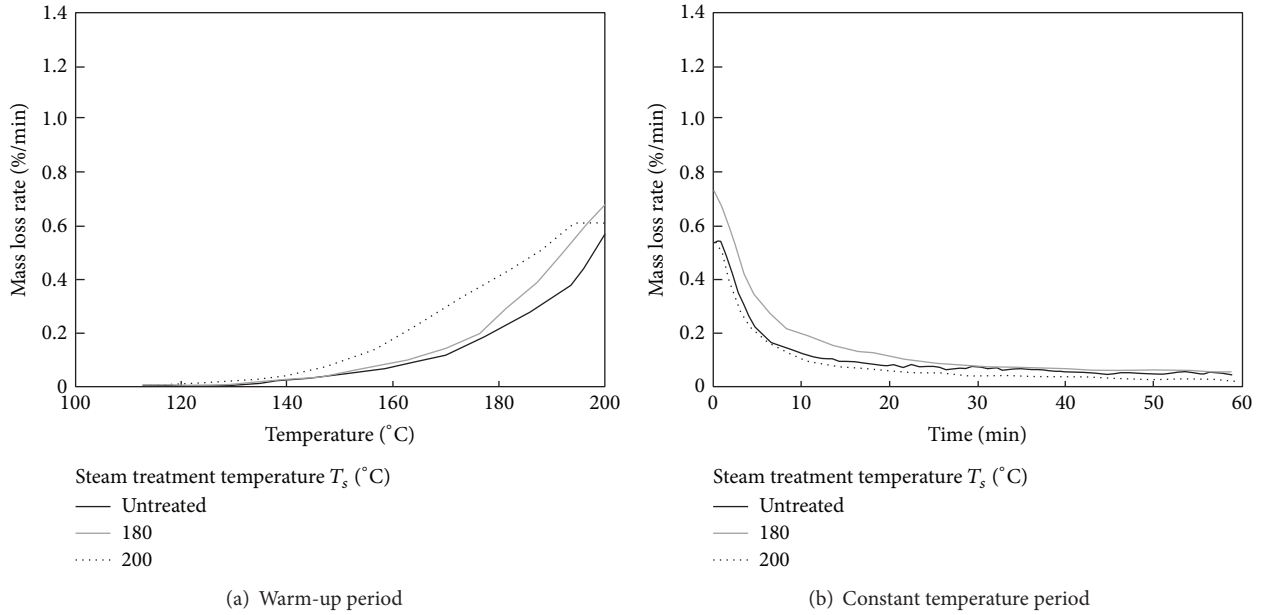


FIGURE 8: Mass change rates of bamboo powder untreated and steam treated with a variable steam treatment temperature T_s . ($t_s = 20$ min).

flow when t_h was over 10 min. The powder temperature did not reach 200°C yet when t_h was only 1 min. Accordingly, powder fluidity at $T_s = 200^\circ\text{C}$, which flowed immediately for $t_h = 1$ min, could have become activated at a temperature under 200°C. These results suggest that untreated powder can be activated by heating under ordinary pressure for a short time. For steam treated powder, it was confirmed that dry-heating has a negative effect on thermal fluidity regardless of steam treatment temperature or time.

3.3. Bamboo Powder Mass Loss during Warm-Up and Constant Temperature Periods. Figure 8 shows the mass loss rate for bamboo powder during the temperature increase to 200°C and when being held constant at 200°C for a variable steam treatment temperature T_s . The steam treatment time t_s of steam treated powder was 20 min. The mass loss rate shows the chemical change intensity because component volatilization occurs from woody material thermal decomposition [21]. As shown in Figure 8(a), mass loss starts when the temperature reaches about 140°C. The amount of mass lost for steam treated powder was higher than that of untreated powder. In particular, the mass loss rate for $T_s = 180^\circ\text{C}$ surpassed that of untreated powder when the temperature reached about 160°C, where it continued to increase until 200°C. This result suggests that chemical changes in powder are activated by a 180°C steam treatment. For $T_s = 200^\circ\text{C}$, the mass loss rate surpassed the untreated powder at about 145°C, and it continued to increase until 190–195°C. This suggests that the chemical changes become active at a lower temperature and the intensity relaxes at 190–200°C. With constant temperature, the mass loss rate of each powder decreases with time and ceases after about 30 min as shown in Figure 8(b). The mass loss rate for $T_s = 180^\circ\text{C}$ powder is comparatively high until 30 min. This result indicates that

chemical changes continued for 30 min after increasing the temperature to 200°C, and $T_s = 180^\circ\text{C}$ powder was the most active at constant temperature.

Figure 9 shows the bamboo powder mass loss rate for $T_s = 200^\circ\text{C}$ during the temperature increase to 200°C and when being held constant at 200°C for a variable steam treatment time t_s . In the warm-up period, as shown in Figure 9(a), the amount of mass lost decreases with increasing t_s . The mass loss rates for $t_s = 10$ and 20 min become constant at 190–195°C, while $t_s = 40$ min becomes constant at about 185°C. This result suggests that the chemical change intensity decreases with an increase in t_s . For constant steam treatment temperature, as shown in Figure 9(b), the mass loss rate for each powder decreases and becomes constant at 30 min.

It was reported that water-soluble components are produced from hemicellulose by steam treatment and some of these components change to volatile components, such as furfural, from high temperature at a prolonged exposure time [11]. Thus, an increase in mass loss from steam treatment could have been due to an increase in volatile water-soluble components. For long t_s , it is possible that powder loses its water-soluble components through dissolving with water or volatilization during steam treatment. For this reason, it was determined that the amount of mass loss decreases with an increase in t_s .

Relationship between thermal fluidity and mass loss during warm-up and constant temperature periods is discussed. As shown in Figures 5 and 8, $T_s = 200^\circ\text{C}$ powder flow starts early compared to the other steam treatment temperatures and mass change begins at a lower rheometer temperature. It was reported that chemical changes associated with component volatilization relate with woody material thermal fluidity [13, 19]. It was determined that $T_s = 200^\circ\text{C}$ powder fluidity was adequately activated during the 5 min dry-heating. For

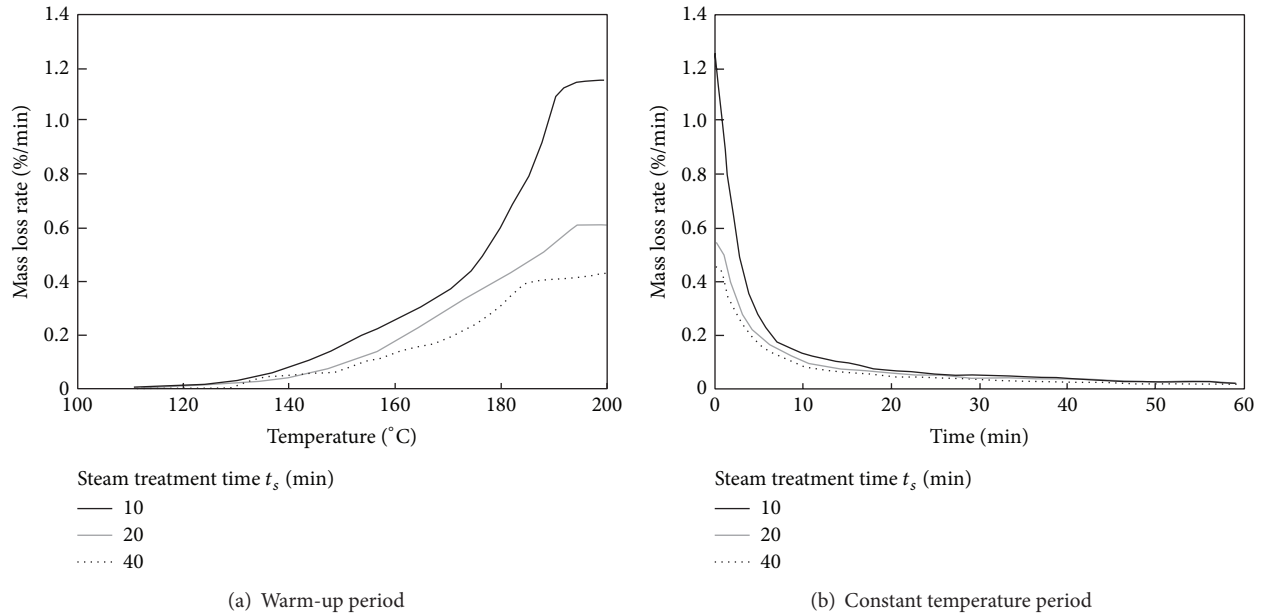


FIGURE 9: Mass loss rate for steam treated bamboo powder with a variable steam treatment time t_s . ($T_s = 200^\circ\text{C}$).

untreated and steam treated powder at 180°C , fluidity was not adequately activated after 5 min of dry-heating. Thus, flow started after about 20 min of pressing time and $T_s = 180^\circ\text{C}$ powder flow start began earlier than the untreated powder because chemical changes at $T_s = 180^\circ\text{C}$ were more active with a constant rheometer temperature. The thermal fluidity changes from t_s , as shown in Figure 6, were also caused by the intensity differences in the chemical changes associated with the component volatilization. $T_s = 200^\circ\text{C}$ powder flow started immediately after pressing because the chemical changes caused by the 5 min dry-heating activated the fluidity, but the chemical change intensity decreases with an increase in t_s as shown in Figure 9(a). Therefore, the flow rate decreases with an increase in t_s .

Next, we discuss the effect of dry-heating time on thermal fluidity in an oven-dry state and the chemical changes during dry-heating. For untreated powder as shown in Figure 7(a), it was determined that the flow started early when t_h increased from 1 to 5 min because the fluidity was activated by a 5 min dry-heating. However, the flow started later with an increase in t_h from 5 to 20 min. It is possible that this is because of component volatilization. It was considered that volatile components have a large effect on thermal fluidity, but the volatile components escape from the powder during dry-heating because dry-heating was conducted under atmospheric pressure. As shown in Figure 8(b), it can be seen that volatilization occurred for 30 min in each powder. Accordingly, the powder fluidity decreases with an increase in t_h because of volatile components escaping from the powder during dry-heating. By contrast, component volatilization could have been inhibited during pressing due to the powder's high pressure state. Thus, fluidity was activated through pressing and heating from occurring chemical changes, while the volatile components remain in the powder.

For steam treated powder, the flow showed a tendency to start later at a slower rate as t_h changed from 1 to 20 min as shown in Figures 7(b)–7(e). The volatilization amount was larger than that of untreated powder until the temperature reached 200°C , as shown in Figures 8(a) and 9(a). Therefore, the fluidity of steam treated powder was activated with ease until the temperature reached 200°C , but the negative effect volatilization has on fluidity was greater than the heating effect for fluidity activation when the temperature reached 200°C .

4. Conclusions

In this study, thermal flow tests of untreated and steam treated bamboo powder were performed using a capillary rheometer to investigate the effect of heating at an oven-dry state on thermal fluidity. The test temperature and dry heating temperature were set at 200°C . Untreated and steam treated bamboo powder at 180°C started to flow several minutes after the start of pressing. Steam treated powder at 200°C flowed immediately after pressing. When the powder dry-heating time increased in an oven-dry state before pressing, the untreated powder flow began earlier with an increase in dry-heating time from 1 to 5 min but started later with an increase in dry-heating time from 5 to 20 min. The flow of the steam treated powder started later with an increase in dry-heating time from 1 to 20 min. From the thermogravimetry results during the increasing and constant temperature periods, it was confirmed that chemical changes associated with component volatilization relate with thermal fluidity. For untreated powder, fluidity is improved from chemical changes during a short dry-heating, but fluidity decreases because the powder loses its fluidity related components from volatilization with a long dry-heating. For steam treated powder, fluidity was

high when the dry-heating was short because of the chemical change intensity associated with volatilization. It was easy to slow fluidity with dry-heating because the powder readily loses its fluidity related components due to the large amount of volatilization.

Conflict of Interests

The authors declare that there is no conflict of interests regarding the publication of this paper.

Acknowledgment

This work was supported by JSPS KAKENHI (Grant nos. 24360309 and 26-9571).

References

- [1] S. Migneault, A. Koubaa, F. Erchiqui et al., "Effect of fiber length on processing and properties of extruded wood-fiber/HDPE composites," *Journal of Applied Polymer Science*, vol. 110, no. 2, pp. 1085–1092, 2008.
- [2] M. Seki, T. Miki, S. Tanaka, I. Shigematsu, and K. Kanayama, "Effect of thermoplastic binder on flow deformation behavior of wood," *Procedia Engineering*, vol. 81, pp. 855–860, 2014.
- [3] N. M. Stark, L. M. Matuana, and C. M. Clemons, "Effect of processing method on surface and weathering characteristics of wood-flour/HDPE composites," *Journal of Applied Polymer Science*, vol. 93, no. 3, pp. 1021–1030, 2004.
- [4] O. Yamashita, Yokochi, H. Imanishi, and K. Kanayama, "Transfer molding of bamboo," *Journal of Materials Processing Technology*, vol. 192–193, pp. 259–264, 2007.
- [5] S. Ellis and L. Paszner, "Activated self-bonding of wood and agricultural residues," *Holzforschung*, vol. 48, pp. 82–90, 1994.
- [6] O. V. Startsev, B. N. Salin, Y. G. Skuridin, R. M. Utemesov, and A. D. Nasonov, "Physical properties and molecular mobility of the new wood composite plastic 'thermobalite,'" *Wood Science and Technology*, vol. 33, no. 1, pp. 73–83, 1999.
- [7] I. Takahashi, Y. Takasu, T. Sugimoto, Y. Kikata, and Y. Sasaki, "Thermoplastic flow behavior of steamed wood flour under heat and compression," *Wood Science and Technology*, vol. 44, no. 4, pp. 607–619, 2010.
- [8] N. Laemsak and M. Okuma, "Development of boards made from oil palm frond II: properties of binderless boards from steam-exploded fibers of oil palm frond," *Journal of Wood Science*, vol. 46, no. 4, pp. 322–326, 2000.
- [9] I. Takahashi, T. Sugimoto, Y. Takasu, M. Yamasaki, Y. Sasaki, and Y. Kikata, "Effect of wood species on thermal flow behavior and physical properties of thermoplastic moldings," *Wood Science and Technology*, vol. 46, no. 1–3, pp. 419–429, 2012.
- [10] W. E. Hillis and A. N. Rozsa, "High temperature and chemical effects on wood stability," *Wood Science and Technology*, vol. 19, no. 1, pp. 57–66, 1985.
- [11] M. Tanahashi, "Characterization and degradation mechanisms of wood components by steam explosion and utilization of exploded wood," *Wood Research*, no. 77, pp. 49–117, 1990.
- [12] B. F. Tjeerdma and H. Militz, "Chemical changes in hydrothermal treated wood: FTIR analysis of combined hydrothermal and dry heat-treated wood," *Holz Als Roh- und Werkstoff*, vol. 63, no. 2, pp. 102–111, 2005.
- [13] S. Kajikawa and T. Iizuka, "Effect of water-soluble components mass on the fluidity of the steam-treated bamboo powder caused by heating and compression," *Journal of the Society of Materials Science, Japan*, vol. 64, no. 5, pp. 381–386, 2015 (Japanese).
- [14] S. Kajikawa and T. Iizuka, "Injection molding using only 200°C steamed bamboo powder by controlling metal mold temperature," *Procedia Engineering*, vol. 81, pp. 1186–1191, 2014.
- [15] S. Kajikawa and T. Iizuka, "Effect of molding temperature on fluidity and injection moldability of oven-dry steam-treated bamboo powder," *Journal of Materials Processing Technology*, vol. 225, pp. 433–438, 2015.
- [16] K. Kojiro, Y. Furuta, and Y. Ishimaru, "Influence of heating history on dynamic viscoelastic properties and dimensions of dry wood," *Journal of Wood Science*, vol. 54, no. 3, pp. 196–201, 2008.
- [17] D. A. I. Goring, "Thermal softening of lignin, hemicellulose and cellulose," *Pulp Paper Magazine of Canada*, vol. 64, no. 12, pp. T517–T527, 1963.
- [18] H. Hiura, T. Arikawa, and D. D. Bahadur, "Risk of sediment related disasters due to the abandoned expanding bamboo stands at the foot of slopes surrounding city area," *Journal of the Japan Landslide Society*, vol. 41, no. 4, pp. 323–334, 2004 (Japanese).
- [19] E. Udaka, T. Miki, H. Sugimoto, and K. Kanayama, "Ryudou seikei ni okeru baiomasu no ryudou mekanizumu no kaimei," *Kagawa Prefectural Industrial Technology Research Center Kenkyu Houkoku*, vol. 9, pp. 11–14, 2009 (Japanese).
- [20] W. Liese, "Research on bamboo," *Wood Science and Technology*, vol. 21, no. 3, pp. 189–209, 1987.
- [21] W. Jim, K. Singh, and J. Zondlo, "Pyrolysis kinetics of physical components of wood-polymers using isoconversion method," *Agriculture*, vol. 3, pp. 12–32, 2013.

Research Article

Effects of Screen Size on Biochemical Conversion of Big Bluestem Biomass for Biofuel Production

Xiaoxu Song,¹ Meng Zhang,¹ Ke Zhang,² Z. J. Pei,¹ and Donghai Wang²

¹Department of Industrial and Manufacturing Systems Engineering, Kansas State University, Manhattan, KS 66506, USA

²Department of Biological and Agricultural Engineering, Kansas State University, Manhattan, KS 66506, USA

Correspondence should be addressed to Meng Zhang; meng@ksu.edu

Received 29 January 2015; Revised 30 May 2015; Accepted 2 June 2015

Academic Editor: Jiang Jianchun

Copyright © 2015 Xiaoxu Song et al. This is an open access article distributed under the Creative Commons Attribution License, which permits unrestricted use, distribution, and reproduction in any medium, provided the original work is properly cited.

Biomass size reduction is the first step for biofuel production from cellulosic biomass through biochemical pathway, and it is usually performed on a mill with screen installed to control the size of the produced particles. The absence of in-depth knowledge about the effects of screen size throughout the biochemical conversion of cellulosic biomass makes it difficult to choose the screen size to conduct biomass size reduction to minimize the energy consumption on mills, maximize the cellulose recovery rate after pretreatment, and maximize the enzymatic hydrolysis efficiency. The objective of this work is to address this issue by generating new knowledge on the effects of screen size in these three processes: size reduction, pretreatment, and enzymatic hydrolysis in conversion of big bluestem biomass for biofuel production. Four screen sizes used in this study were 1, 2, 4, and 8 mm. It was found that using a larger screen size saved energy in biomass size reduction on a knife mill. Moreover, particles produced with larger screen sizes achieved higher cellulose recovery rate after pretreatment, higher enzymatic hydrolysis efficiency, and higher total sugar yield.

1. Introduction

There is a growing need to find alternatives to petroleum-based liquid transportation fuels [1, 2]. Recognized as promising alternatives are biofuels produced from cellulosic biomass (including dedicated energy crops such as big bluestem, forest residues, and agricultural residues) [3–5]. Using cellulosic biomass as the feedstock for biofuel production is advantageous because of its low cost, abundance, and sustainability [6]. An investigation jointly supported by the U.S. Department of Energy and Department of Agriculture shows that land resources in the U.S. are sufficient to sustain production of enough cellulosic biomass (about 1 billion dry tons) annually to replace 30% or more of the nation's current consumption of liquid transportation fuels [3–5].

Conversion of dedicated energy crops such as big bluestem (*Andropogon gerardii*) to biofuels offers major economic and environmental benefits [7]. Big bluestem is a dominant grass in the tallgrass prairies of North America and comprises up to 80% of the prairie biomass in the midwest grassland in the United States [8, 9]. Big bluestem biomass can be converted into ethanol biofuels through

biochemical pathway. Figure 1 illustrates the major steps in the conversion. First, big bluestem biomass size reduction is necessary because current conversion technologies cannot efficiently convert whole stems of big bluestem biomass into ethanol biofuels [10, 11]. The biomass size reduction is usually conducted on a knife mill [12] or hammer mill [13–16] to produce particles with sizes from 0.1 to 10 mm [17]. In knife milling (Figure 2), biomass comes into contact with cutting knives equipped on a rotor in the chamber. Biomass is cut between the knives and the cutting bars. Particles that are smaller than the screen size will pass through the openings on the screen; those larger than the screen size will be recirculated and continue being milled. In hammer milling (Figure 3), hammers are mounted on a rotating drum. Size reduction is performed through impact-induced material fragmentation. Second, pretreatment can make cellulose biomass more accessible to enzymatic hydrolysis through various mechanistic effects including enzyme accessible surface area increases, cellulose decrystallization, hemicellulose removal, lignin removal, and lignin structure alteration [18]. Hydrolysis breaks polysaccharide into component sugars that are convertible to ethanol by fermentation [6]. Finally, the

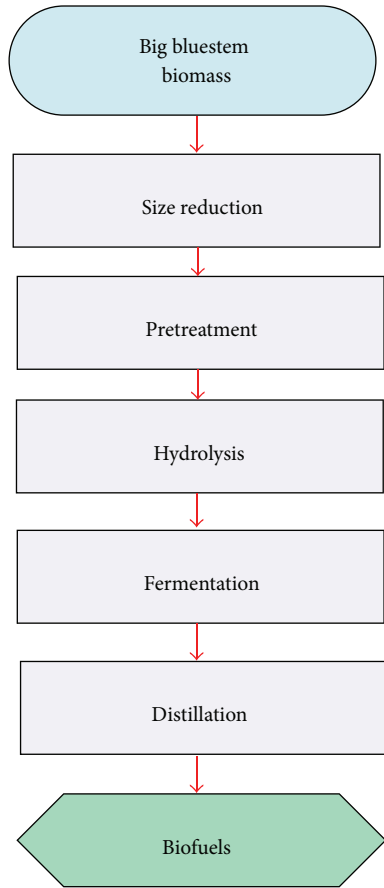


FIGURE 1: Major steps in biochemical conversion of big bluestem biomass into biofuels.

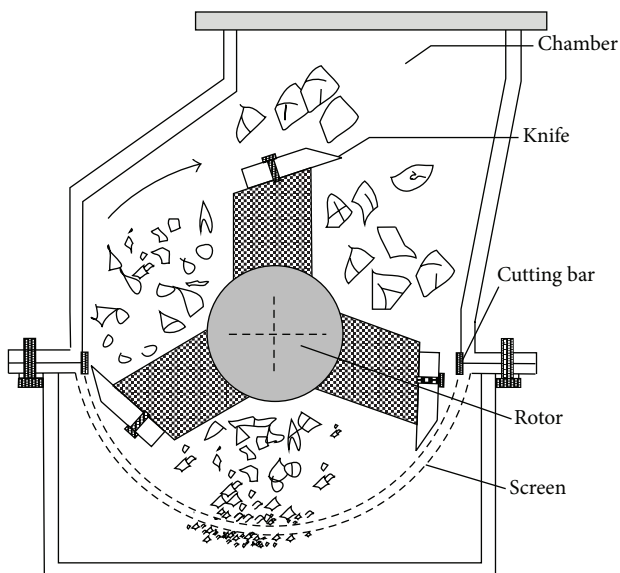


FIGURE 2: Illustration of a knife mill.

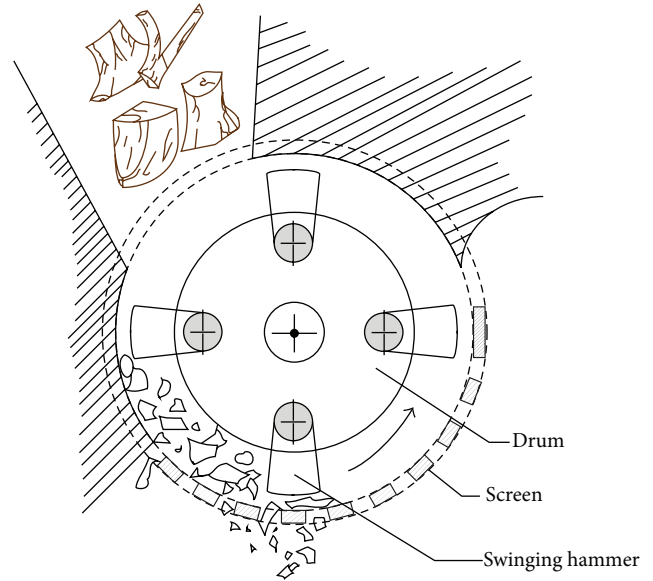


FIGURE 3: Illustration of a hammer mill.

fermented liquid is moved into a distillation system where the liquid is heated to take advantage of the different boiling points of ethanol and water. The difference will enable the extraction of about 95% pure fuel-grade ethanol [6]. It is also known that fermentable sugar yield in hydrolysis is approximately proportional to the biofuel yield in fermentation [19].

The effect of screen size on energy consumption in biomass size reduction has been studied in the literature. It has been consistently observed that energy consumption in biomass size reduction increased greatly when smaller screen sizes were installed [20–22]. Nevertheless, these studies either were not for biofuel production purpose or did not include the biochemical conversion of produced particles to fermentable sugar. Many other reported studies included biomass biochemical conversion to ethanol biofuels with biomass particles produced by size reduction but did not cover energy consumption in biomass size reduction [23–25].

The absence of in-depth knowledge about the effects of screen size throughout the biochemical conversion of cellulosic biomass makes it difficult to choose the screen size to conduct biomass size reduction in order to minimize the energy consumption on mills, maximize the cellulose recovery rate after pretreatment, and maximize the enzymatic hydrolysis efficiency. The objective of this work is to address this issue by generating new knowledge on effects of screen size in these three processes: size reduction, pretreatment, and enzymatic hydrolysis, using big bluestem biomass.

2. Material and Methods

2.1. Material. The material used in this study was big bluestem harvested from the United States Department of Agriculture Plant Material Center (Manhattan, KS, USA). The entire plant except the root was used. The moisture content of the big bluestem was 5%. Biomass moisture content

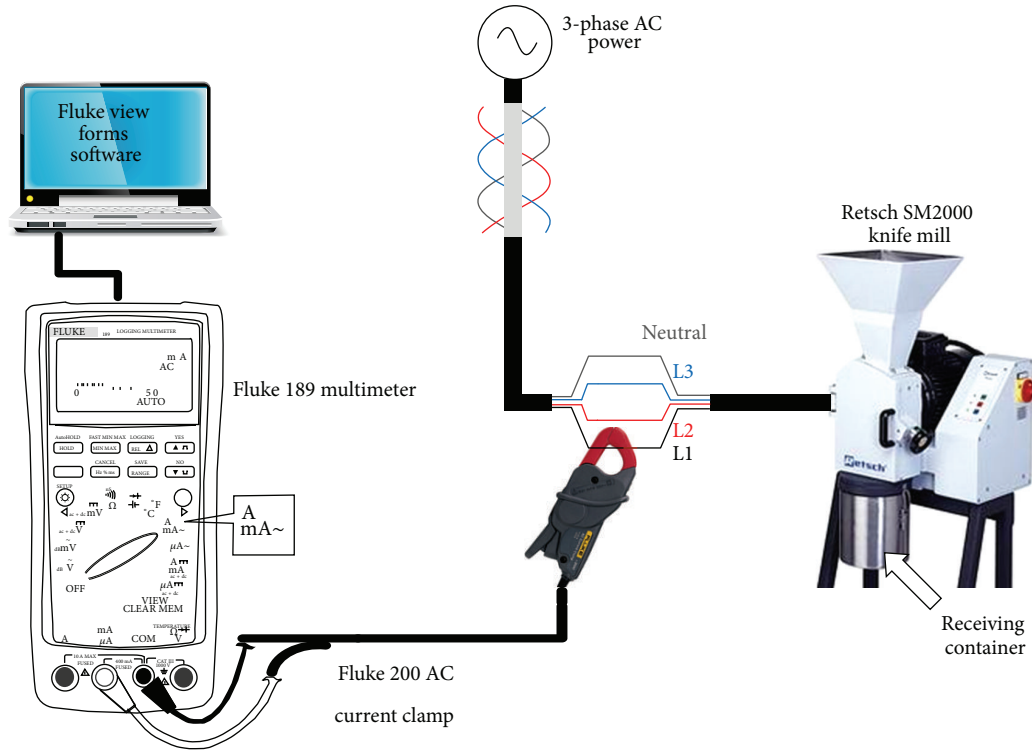


FIGURE 4: Experimental setup.

TABLE 1: Chemical compositions (% dry weight basis) of big bluestem.

Component	Percentage
Cellulose	35.9 (0.4)
Hemicellulose	25.4 (0.5)
Lignin	24.0 (0.7)

was determined by following the laboratory analytical procedures developed by the National Renewable Energy Laboratory [28]. Chemical compositions of cellulose, hemicellulose, and lignin are listed in Table 1 [29].

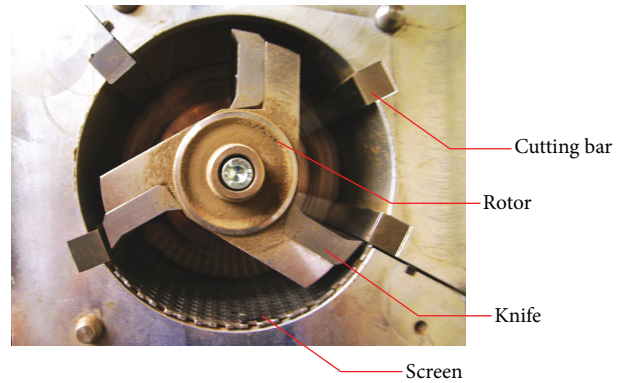


FIGURE 5: Milling chamber of the knife mill.

2.2. Biomass Size Reduction. The experimental setup for size reduction is shown in Figure 4. A knife mill (SM 2000, Retsch GmbH, Haan, Germany) was used. It was powered by a 1.5 kW electric motor. The milling chamber of the mill is pictured in Figure 5. The knife mill is equipped with three knives (95 × 35 mm) on the rotor and four cutting bars mounted on the inside wall of the milling chamber. Big bluestem biomass was cut and sheared into particles between the knives and the cutting bars. A screen (145 × 98 mm) was installed at the bottom of the milling chamber. Four screen sizes (1, 2, 4, and 8 mm) were used in this study. Figure 6 shows a 4 mm screen as an example.

Before starting one size reduction test, the knife mill was run for 10 seconds without loading any biomass to avoid current spikes. Figure 7 shows a typical current chart when the knife mill was running empty. There was a current spike

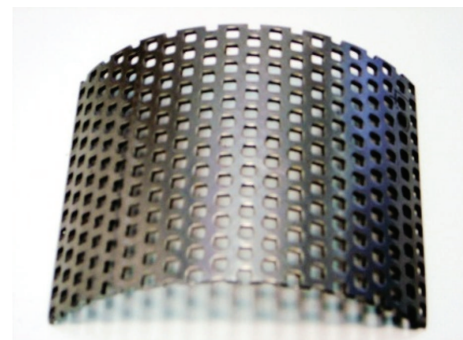


FIGURE 6: Screen used on the knife mill (screen size = 4 mm).

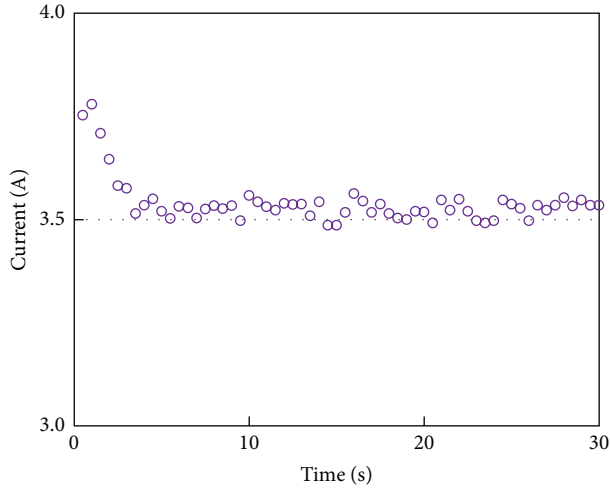


FIGURE 7: A typical current chart for 30 seconds after the knife mill starts without load.

in the first few seconds after the knife mill was turned on. After 10 seconds, the current stayed stable and ten stems of big bluestem were loaded into the milling chamber (one stem is about 50 cm long and 0.5–1 cm wide). During the milling process, more big bluestem stems were loaded into the milling chamber manually by a mill operator at a rate that could keep the milling chamber full. For one size reduction test, the total amount of big bluestem loaded was 400 grams. The mill was turned off after 10 seconds when all the 400 grams of biomass was loaded into the milling chamber. After each test, the weight of the big bluestem particles collected from the receiving container was measured. Not all the 400 grams of biomass could be collected from the receiving container, because there was still biomass retained in the milling chamber when the mill was turned off. Between of two consecutive size reduction tests, the milling chamber was opened to remove any biomass left there, and the chamber was cleaned with compressed air.

2.3. Sugar Conversion. In this study, big bluestem sugar conversion consisted of dilute sulfuric acid pretreatment and enzymatic hydrolysis. In dilute sulfuric acid pretreatment, 10 grams (dry weight) of big bluestem particles produced with each screen size and 200 mL of 2% (w/v) sulfuric acid were loaded in a 600 mL glass liner of a Parr pressure reactor (4760A, Parr Instrument Co., Moline, IL, USA). Pretreatment time was 30 min, and pretreatment temperature was 140°C. This pretreatment condition was selected based on a previous study conducted by the authors using the same type of biomass [30].

After pretreatment, big bluestem particles were washed with 50–60°C distilled water using a suction filtration system with P4 grade filter paper (Fisher Scientific Inc., Waltham, MA, USA) to conduct solid-liquid separation. The solid biomass after filtration was carefully collected from the filter paper using a stainless steel micro spatula. The dry weight of the collected solid biomass was measured; then a small portion of the solid biomass was used for biomass

composition analysis, and the rest was used for subsequent enzymatic hydrolysis. The liquid after filtration was removed, which included dissolved sugars, acid residues, and inhibitors (substances that could decrease enzymes' ability to break cellulose into glucose) formed during pretreatment.

Enzymatic hydrolysis was carried out in eight 125 mL flasks in a water bath shaker (C76, New Brunswick Scientific, Edison, NJ, USA) at 50°C for 48 h. The agitation speed of the water bath shaker was 110 rpm. There were two flasks containing big bluestem particles produced with each of the four screen sizes. Each flask contained 50 mL of hydrolysis slurry. The slurry consisted of 4% (w/v) biomass on dry weight base, sodium acetate buffer (50 mM, pH = 4.8), and 0.02% (w/v) sodium azide to prevent microbial growth during hydrolysis. Accellerase 1500 enzyme complex (Danisco USA, Inc., Rochester, NY, USA) was used. The enzyme loaded was 0.5 mL for each gram of dry biomass.

3. Measurement and Calculation

3.1. Energy Consumption in Biomass Size Reduction. Energy consumption in biomass size reduction was measured as the electricity consumed by the electric motor of the knife mill. As illustrated in Figure 4, electric current to the motor was measured using a Fluke 200 AC current clamp connected to a Fluke 189 multimeter (Fluke Corp., Everett, WA, USA). The 3-phase AC power supply in this study was in a Y configuration with four wires (3 phases: L1, L2, L3, and neutral). Electric current readings were collected by software (FlukeView Forms Basic, Fluke Corp., Everett, WA, USA) with a sampling rate of two readings per second. Data acquisition began after the initial ten stems of big bluestem were loaded into the milling chamber and stopped until the mill was turned off.

The data acquisition software recorded the average current (I_{AVE}). The voltage (V) was 208 V. The energy consumed in one size reduction test (t seconds) (P) was calculated as follows:

$$P = \frac{\sqrt{3} \cdot I_{AVE} \cdot V \cdot t}{3600} \text{ (Wh)}. \quad (1)$$

Dividing P by the weight (w) of the big bluestem particles collected after the test would give energy consumption (E) per unit weight as follows:

$$E = \frac{P}{w} \text{ (Wh/g)}. \quad (2)$$

3.2. Biomass Composition. Carbohydrates (cellulose and hemicellulose) and lignin make up a major portion of cellulosic biomass. Cellulose can be converted to fermentable sugar (glucose) in enzymatic hydrolysis. Hemicellulose is also sugar component; however, almost all of the hemicellulose will be decomposed by dilute sulfuric acid pretreatment. Lignin contains no sugar [31]. Biomass composition analysis is needed for the analyses in Section 4. After measuring the dry weight of biomass before and after pretreatment (W_{BP}

and W_{AP}), biomass weight loss in pretreatment (L) (%) was calculated as follows:

$$L (\%) = \frac{W_{BP} - W_{AP}}{W_{BP}} \times 100\%. \quad (3)$$

In this study, biomass composition after pretreatment was determined according to the laboratory analytical procedures developed by the National Renewable Energy Laboratory [32]. Briefly, after pretreatment, biomass collected for composition analysis was dried in an oven (Isotemp 500 Series, Fisher Scientific Inc., Waltham, MA, USA) at 40°C for 48 h. About 0.3 g of oven-dried biomass sample was soaked in 72% sulfuric acid at 30°C for 1 h with constant stirring. Then, it was diluted to a 4% acid solution and heated at 120°C for another 1 h. After heating, the liquid and solid parts of the biomass sample were separated by suction filtration. The liquid part was adjusted to pH neutral by adding calcium carbonate; then the cellulose and hemicellulose contents in the liquid part were measured by a high-performance liquid chromatography (HPLC) system (Shimadzu, Kyoto, Japan), and the acid-soluble lignin content in the liquid was detected by a UV-visible spectrophotometer (BioMate 3, Thermo Electron Corp., Madison, WI, USA). The solid part was placed in a furnace at 575°C for 24 h. The weight difference between the dry solid and ash residue after furnace heating was reported to be acid-insoluble lignin. The sum of the acid-soluble and acid-insoluble lignin contents was the total lignin content. Two duplications for each biomass sample were measured. Biomass composition reported in this study was the weight percentage of cellulose, hemicellulose, and lignin.

3.3. Sugar Analysis. After 48 h of enzymatic hydrolysis, sugar contents in the biomass samples were determined by analyzing the supernatant from the hydrolysis slurry using an HPLC system (Shimadzu, Kyoto, Japan). HPLC is an analytical tool for separating and quantifying components in complex liquid mixtures. The HPLC system was equipped with an RCM-monosaccharide column (300 × 7.8 mm; Phenomenex, Torrance, CA, USA) and a refractive index detector (RID-10A, Shimadzu, Kyoto, Japan). The column was eluted with double distilled water at a flow rate of 0.6 mL/minute, and the temperature of the column was maintained at 80°C.

Cellulose recovery rate after pretreatment (R_P) is used to evaluate how much cellulose can be recovered in the pretreatment. It is calculated as the ratio of the cellulose weight after pretreatment to the cellulose weight before pretreatment:

$$R_P (\%) = \frac{C_{AP}}{C_{BP}} \times (1 - L), \quad (4)$$

where C_{AP} (%) is the cellulose content in the biomass after pretreatment, C_{BP} (%) is the cellulose content in the biomass before pretreatment, and L (%) is the biomass weight loss in pretreatment. These two cellulose contents were obtained by biomass composition analysis. Higher R_P means that there was less loss in potential sugar (cellulose) during pretreatment.

Enzymatic hydrolysis efficiency (E_H) is expressed in terms of the percentage of cellulose converted to glucose by enzymatic hydrolysis and calculated using the following equation:

$$E_H (\%) = \frac{c \times V}{1.11 \times W_H \times C_{AP}} \times 100\%, \quad (5)$$

where c (g/L) is the concentration of glucose in the flask slurry after 48 h hydrolysis, V (L) is the total volume of the slurry, W_H (g) is the dry weight of the biomass loaded into the flask, and C_{AP} (%) is the cellulose content in the biomass before hydrolysis (after pretreatment). The factor 1.11 is the cellulose-to-glucose conversion factor, which reflects the weight gain in converting cellulose to glucose in hydrolysis.

Total cellulose conversion rate (R_T) is used to evaluate the overall efficiency of pretreatment and enzymatic hydrolysis in converting cellulose to glucose. It is the percentage of cellulose in unpretreated biomass that is converted to glucose after enzymatic hydrolysis. It is the product of enzymatic hydrolysis efficiency (E_H) and cellulose recovery rate after pretreatment (R_P):

$$R_T (\%) = \frac{E_H \times R_P}{100\%}. \quad (6)$$

In this study, total sugar yield (Y_T) provides a straightforward interpretation about how much glucose a unit dry weight of biomass (before pretreatment) can yield through biochemical conversion. Its calculation is described as follows:

$$Y_T \left(\frac{\text{g glucose}}{\text{g biomass}} \right) = \frac{c \times V \times W_{AP}}{W_H \times W_{BP}}. \quad (7)$$

3.4. Statistical Analysis. Chemical compositions in Tables 1 and 3 are reported as the means with standard deviations in brackets. Multiple comparisons using one-way analysis of variance (ANOVA) were conducted using Minitab software (Version 16, Minitab Inc., State College, PA, USA) to check the existence of significant differences within the means. Error bars in figures are drawn using standard deviations. Different letters (a, b, c, and d) indicate that the means are significantly different in the order of $a > b > c > d$ based on Fisher LSD test at level of $\alpha = 0.05$. The same letters indicate that means have statistically no difference.

4. Results and Discussion

4.1. Effects of Screen Size on Energy Consumption in Biomass Size Reduction. Figure 8 shows that screen size had a significant effect on energy consumption in size reduction of big bluestem. Energy consumption decreased greatly as screen size increased. Energy consumption was as high as 0.13 and 0.12 Wh/g for screen sizes of 1 and 2 mm, respectively. When using 4 and 8 mm screens, energy consumption decreased to 0.09 and 0.08 Wh/g, respectively. It was observed that a major factor that caused the high energy consumption when using a smaller screen size was that it took longer time to produce the same weight of particles than using larger screen sizes.

TABLE 2: Energy consumption in biomass size reduction using Retsch SM2000 knife mill.

Biomass material	Moisture content (% dry weight basis)	Screen size (mm)	Energy consumption (Wh/g)	Reference
Big bluestem (whole stems)	5	1	0.13	This study
		2	0.12	
		4	0.09	
		8	0.07	
<i>Miscanthus</i> (segments)	7–10	1	0.28	[20, 21]
		2	0.10	
		4	0.06	
		8	0.04	
Switchgrass (segments)	7–10	1	0.27	[20, 21]
		2	0.12	
		4	0.06	
		8	0.03	
Wheat straw (whole stems)	12	1	0.16	[26]
		2	0.12	
		8	0.06	
Sorghum stalk (whole stems)	9	1.5	0.09	[27]
		8	0.04	
<i>Kochia</i> (whole stems)	10	1.5	0.07	[27]

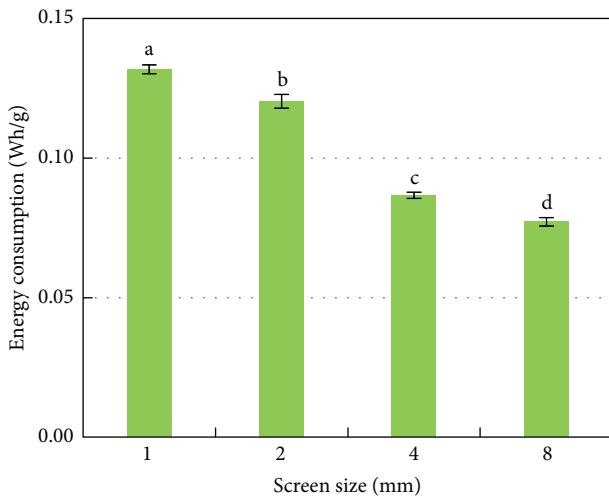


FIGURE 8: Effects of screen size on energy consumption in size reduction of big bluestem.

TABLE 3: Chemical compositions (% dry weight basis) of big bluestem after pretreatment.

Component	Screen size (mm)			
	1	2	4	8
Cellulose	56.4 (1.2) ^a	58.6 (0.9) ^a	58.4 (0.5) ^a	58.9 (0.6) ^a
Hemicellulose	5.7 (0.6) ^b	5.2 (0.3) ^b	4.9 (0.7) ^b	4.6 (0.2) ^b
Lignin	28.6 (0.7) ^c	28.0 (1.3) ^c	29.8 (0.2) ^c	29.6 (1.0) ^c

The same letters indicate that means have statistically no difference based on Fisher LSD test at level of $\alpha = 0.05$.

In the literature, there are no reports on energy consumption in size reduction of big bluestem. There are some reports

on energy consumption about size reduction of other types of herbaceous biomass using the Retsch SM 2000 knife mill. Energy consumption data when using different screen sizes on the knife mill were summarized in Table 2. As indicated in the table, using smaller screen size would consume more energy to produce the same amount of biomass particles. It was noticed that, in previous studies reported by Miao et al. [19, 20], herbaceous biomass loaded into the knife mill was biomass segments prepared by a chopping machine before knife milling, whereas other studies in Table 2 used whole stem of herbaceous biomass as input materials to the knife mill.

4.2. Effects of Screen Size on Cellulose Recovery Rate after Pretreatment. Table 3 lists big bluestem chemical composition after pretreatment. It was noticed that chemical compositions of particles produced with different screen sizes are approximately the same.

Figure 9 shows that there was more biomass weight loss in pretreatment for particles produced with a smaller screen size. The major weight loss in pretreatment was caused by the decomposition of hemicellulose. The primary objective of dilute sulfuric acid pretreatment is to break down the shield formed by highly associated lignin and hemicellulose by decomposing hemicellulose to acid-soluble products (i.e., xylose), so that cellulose can be released and become more accessible to enzymes in enzymatic hydrolysis [33]. However, a side effect is that a small amount of cellulose may be degraded to hydroxymethyl-furfural (HMF) [33]. HMF is soluble in the pretreatment liquid and will be separated from the solid biomass after pretreatment. Only the solid biomass collected after pretreatment goes into enzymatic hydrolysis. The degradation of cellulose to HMF results in potential sugar (cellulose) loss and leads to decreasing total sugar yield [27].

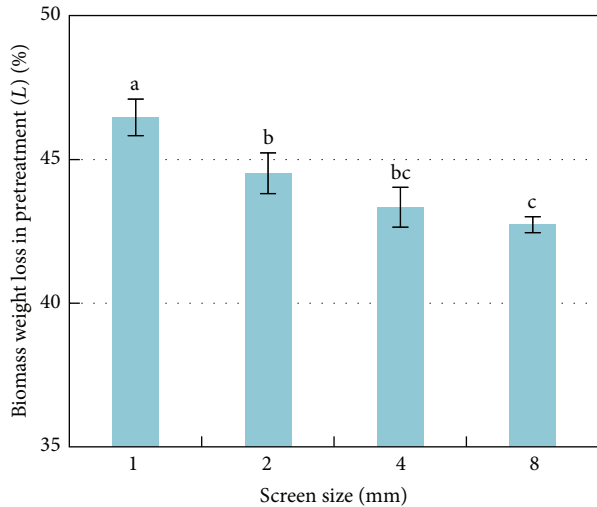


FIGURE 9: Effects of screen size on biomass weight loss in pretreatment.

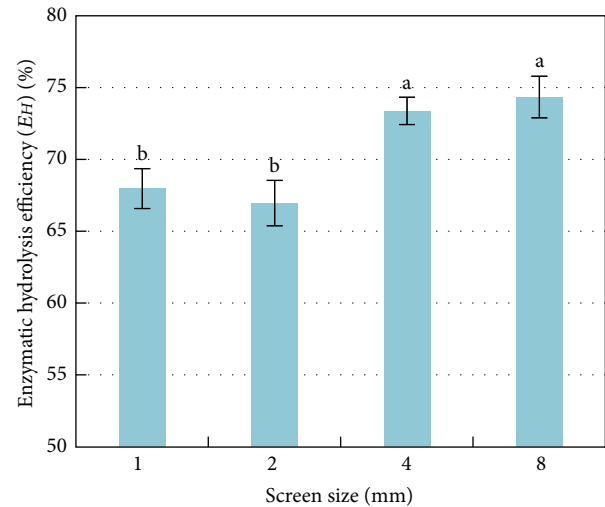


FIGURE 11: Effects of screen size on enzymatic hydrolysis efficiency.

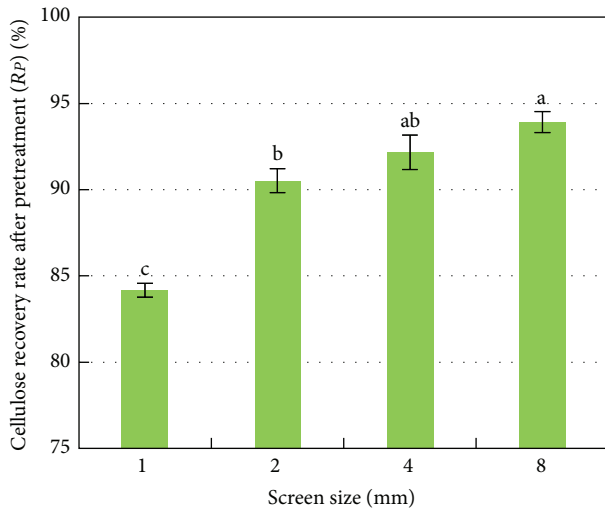


FIGURE 10: Effects of screen size on cellulose recovery rate after pretreatment.

Figure 10 shows that cellulose recovery rate after pretreatment was higher for big bluestem particles produced with a larger screen size. It is believed that biomass with a smaller particle size will be more amenable to pretreatment; as a result, higher cellulose degradation and hemicellulose decomposition will happen for smaller particles comparing to larger ones under the same severe pretreatment. Ballesteros et al. [34] reported the same trend from a similar study. They used softwood chips of three size levels (2–5, 5–8, and 8–12 mm) treated with steam-explosion pretreatment. They observed that chip size had a significant influence on cellulose recovery rate after pretreatment. As chip size increased, cellulose recovery rate after pretreatment increased.

As lignin has a complex three-dimensional aromatic structure and heterogeneity, its structural properties might be altered differently by experiencing different degree of

mechanical comminution when using three screen sizes in size reduction and later by dilute acid pretreatment. As a future research question, these structural property changes can be further investigated by conducting FTIR spectroscopy of lignin processed with different screen sizes before and after pretreatment [35].

4.3. Effects of Screen Size on Enzymatic Hydrolysis Efficiency.

As shown in Figure 11, big bluestem particles produced with 4 or 8 mm screen sizes had higher enzymatic hydrolysis efficiency than the particles produced with 1 or 2 mm screen sizes. The difference in enzymatic hydrolysis efficiency between particles produced with 4 and 8 mm or between those produced with 1 and 2 mm screen sizes was insignificant. One possible explanation given by Sarkar et al. [16] is that fine biomass particles may impose negative effects on the subsequent processing. They may cause the generation of clumps during enzymatic hydrolysis. Theerarattananoon et al. [30] reported similar results. Three types of biomass materials (big bluestem, corn stover, and wheat straw) were size reduced on a hammer mill with screen sizes of 3.2 and 6.5 mm. Particles produced with screen size of 6.5 mm had higher enzymatic hydrolysis efficiency than those produced with screen size of 3.2 mm. In their experiments, there was a pelleting process (the agglomeration of small particles into firm, uniformly shaped granules by the means of mechanical processes) between size reduction and pretreatment.

4.4. Effects of Screen Size on Total Cellulose Conversion Rate and Total Sugar Yield.

As shown in Figure 12, big bluestem particles produced with larger screen sizes achieved higher total cellulose conversion rate. Nearly 70% of the cellulose in particles produced with the 8 mm screen size was converted to glucose, which was about 20% higher than that produced with the 1 mm screen size.

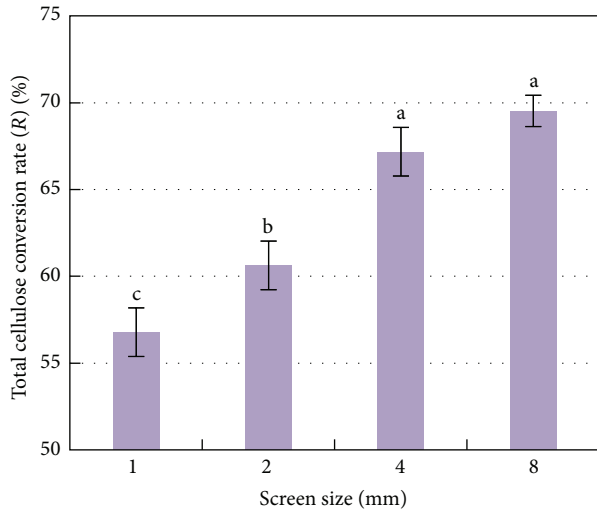


FIGURE 12: Effects of screen size on total cellulose conversion rate.

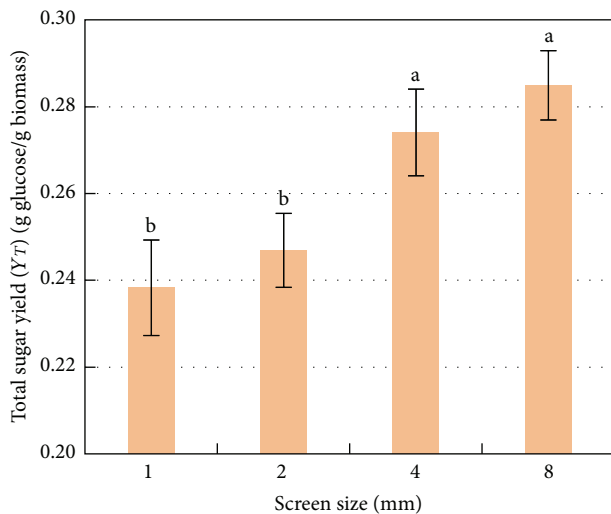


FIGURE 13: Effects of screen size on total sugar yield.

Figure 13 shows total sugar yield results. As screen size used in size reduction increased, total sugar yield of the produced particles increased. Big bluestem particles produced with 8 mm screen size yielded 20% more sugar than those produced with 1 mm screen size.

5. Conclusions

This study presents the first effort in investigating the effects of screen size used in biomass size reduction throughout the biochemical conversion of big bluestem to fermentable sugar. Major conclusions are as follows:

- (1) Energy consumption in biomass size reduction increased greatly as screen size became smaller (from 8 to 1 mm).

- (2) Big bluestem particles produced with a larger screen size had higher cellulose recovery rate after pretreatment.
- (3) Big bluestem particles produced with larger screen sizes (4 and 8 mm) had higher enzymatic hydrolysis efficiency, higher total cellulose conversion rate, and higher total sugar yield than those produced with smaller screen sizes (1 and 2 mm).

Conflict of Interests

The authors declare that there is no conflict of interests regarding the publication of this paper.

Acknowledgments

This study is supported by the U.S. National Science Foundation through Award 0970112. Publication of this paper was funded in part by the Kansas State University Open Access Publishing Fund.

References

- [1] J. Fargione, J. Hill, D. Tilman, S. Polasky, and P. Hawthorne, "Land clearing and the biofuel carbon debt," *Science*, vol. 319, no. 5867, pp. 1235–1238, 2008.
- [2] Energy Information Administration, "Annual energy review 2011," Report No. DOE/EIA-0384, 2011, <http://www.eia.gov/totalenergy/data/annual/pdf/aer.pdf>.
- [3] U.S. Department of Energy, "Biomass as feedstocks for a bioenergy and byproducts industry: the technical feasibility of a billion-ton annual supply," http://feedstockreview.ornl.gov/pdf/billion_ton_vision.pdf.
- [4] U.S. Department of Energy, "U.S. billion-ton update: biomass supply for a bioenergy and bioproducts industry," http://www1.eere.energy.gov/biomass/pdfs/billion_ton_update.pdf.
- [5] P. Moriarty and D. Honnery, "Low-mobility: the future of transport," *Futures*, vol. 40, no. 10, pp. 865–872, 2008.
- [6] E. M. Rubin, "Genomics of cellulosic biofuels," *Nature*, vol. 454, no. 7206, pp. 841–845, 2008.
- [7] J. Gan, W. Yuan, L. Johnson, D. Wang, R. Nelson, and K. Zhang, "Hydrothermal conversion of big bluestem for bio-oil production: the effect of ecotype and planting location," *Bioresource Technology*, vol. 116, pp. 413–420, 2012.
- [8] F. Gould and R. Shaw, *Grass Systematics*, Texas A&M University Press, College Station, Tex, USA, 2nd edition, 1963.
- [9] A. K. Knapp, J. M. Briggs, D. C. Hartnett, and S. L. Collins, *Grassland Dynamics: Long-Term Ecological Research in Tallgrass Prairie*, Oxford University Press, New York, NY, USA, 1998.
- [10] L. Wei, L. O. Pordesimo, C. Igathinathane, and W. D. Batchelor, "Process engineering evaluation of ethanol production from wood through bioprocessing and chemical catalysis," *Biomass and Bioenergy*, vol. 33, no. 2, pp. 255–266, 2009.
- [11] P. Kumar, D. M. Barrett, M. J. Delwiche, and P. Stroeve, "Methods of pretreatment of lignocellulosic biomass for efficient hydrolysis and biofuel production," *Industrial & Engineering Chemistry Research*, vol. 48, pp. 3713–3729, 2009.
- [12] S. Paulrud, J. E. Mattsson, and C. Nilsson, "Particle and handling characteristics of wood fuel powder: effects of different mills," *Fuel Processing Technology*, vol. 76, no. 1, pp. 23–39, 2002.

- [13] M. T. Holtzapple, A. E. Humphrey, and J. D. Taylor, "Energy requirements for the size reduction of poplar and aspen wood," *Biotechnology and Bioengineering*, vol. 33, no. 2, pp. 207–210, 1989.
- [14] L. Cadoche and G. D. López, "Assessment of size reduction as a preliminary step in the production of ethanol from lignocellulosic wastes," *Biological Wastes*, vol. 30, no. 2, pp. 153–157, 1989.
- [15] V. S. P. Bitra, A. R. Womac, N. Chevanan et al., "Direct mechanical energy measures of hammer mill comminution of switchgrass, wheat straw, and corn stover and analysis of their particle size distributions," *Powder Technology*, vol. 193, no. 1, pp. 32–45, 2009.
- [16] N. Sarkar, S. K. Ghosh, S. Bannerjee, and K. Aikat, "Bioethanol production from agricultural wastes: an overview," *Renewable Energy*, vol. 37, no. 1, pp. 19–27, 2012.
- [17] L. Tabil, P. Adapa, and M. Kashaninejad, "Biomass feedstock pre-processing-part 1: pre-treatment," in *Biofuel's Engineering Process Technology*, M. A. S. Bernardes, Ed., pp. 411–438, InTech, Rijeka, Croatia, 2011.
- [18] N. Mosier, C. Wyman, B. Dale et al., "Features of promising technologies for pretreatment of lignocellulosic biomass," *Biore-source Technology*, vol. 96, no. 6, pp. 673–686, 2005.
- [19] A. Pandey, C. Larroche, S. C. Ricke, C. Dussap, and E. Gnansounou, *Biofuels: Alternative Feedstocks and Conversion Processes*, Academic Press, San Diego, Calif, USA, 2011.
- [20] Z. Miao, T. E. Grift, A. C. Hansen, and K. C. Ting, "Specific energy consumption of biomass particle production and particle physical property," in *Proceedings of the American Society of Agricultural and Biological Engineers Annual International Meeting (ASABE' 10)*, pp. 584–604, Pittsburgh, Pa, USA, June 2010.
- [21] Z. Miao, T. E. Grift, A. C. Hansen, and K. C. Ting, "Energy requirement for comminution of biomass in relation to particle physical properties," *Industrial Crops and Products*, vol. 33, no. 2, pp. 504–513, 2011.
- [22] B. C. Vidal Jr., B. S. Dien, K. C. Ting, and V. Singh, "Influence of feedstock particle size on lignocellulose conversion—a review," *Applied Biochemistry and Biotechnology*, vol. 164, no. 8, pp. 1405–1421, 2011.
- [23] S. G. Allen, D. Schulman, J. Lichwa, M. J. Antal Jr., E. Jennings, and R. Elander, "A comparison of aqueous and dilute-acid single-temperature pretreatment of yellow poplar sawdust," *Industrial and Engineering Chemistry Research*, vol. 40, no. 10, pp. 2352–2361, 2001.
- [24] Q. A. Nguyen, M. P. Tucker, F. A. Keller, and F. P. Eddy, "Two-stage dilute-acid pretreatment of softwoods," *Applied Biochemistry and Biotechnology*, vol. 84–86, pp. 561–576, 2000.
- [25] C. Karunanithy and K. Muthukumarappan, "Optimization of alkali, big bluestem particle size, and extruder parameters for maximum enzymatic sugar recovery using response surface methodology," *BioResources*, vol. 6, no. 1, pp. 762–790, 2011.
- [26] T. W. Deines and Z. J. Pei, "Power consumption study in knife milling of wheat straw," *Transactions of the North American Manufacturing Research Institute of SME*, vol. 38, pp. 38–191, 2010.
- [27] T. W. Deines, D. Nottingham, and Z. J. Pei, "Effects of biomass type and sieve size on power consumption in knife milling," in *Proceedings of the IIE Annual Conference and Expo*, Cancun, Mexico, June 2010.
- [28] A. Sluiter, B. Hames, D. Hyman et al., "Determination of total solids in biomass and total dissolved solids in liquid process samples," Tech. Rep. NREL/TP-510-42621, National Renewable Energy Laboratory, 2008, <http://www.nrel.gov/biomass/pdfs/42621.pdf>.
- [29] K. Zhang, L. Johnson, R. Nelson, W. Yuan, Z. Pei, and D. Wang, "Chemical and elemental composition of big bluestem as affected by ecotype and planting location along the precipitation gradient of the Great Plains," *Industrial Crops and Products*, vol. 40, no. 1, pp. 210–218, 2012.
- [30] K. Theerarattananoon, F. Xu, J. Wilson et al., "Effects of the pelleting conditions on chemical composition and sugar yield of corn stover, big bluestem, wheat straw, and sorghum stalk pellets," *Bioprocess and Biosystems Engineering*, vol. 35, no. 4, pp. 615–623, 2012.
- [31] R. Kumar, S. Singh, and O. V. Singh, "Bioconversion of lignocellulosic biomass: biochemical and molecular perspectives," *Journal of Industrial Microbiology & Biotechnology*, vol. 35, no. 5, pp. 377–391, 2008.
- [32] A. Sluiter, B. Hames, R. Ruiz et al., "Determination of structural carbohydrates and lignin in biomass," Tech. Rep. NREL/TP-510-42618, 2011, <http://www.nrel.gov/biomass/pdfs/42618.pdf>.
- [33] G. Hu, J. A. Heitmann, and O. J. Rojas, "Feedstock pretreatment strategies for producing ethanol from wood, bark, and forest residues," *BioResources*, vol. 3, no. 1, pp. 270–294, 2008.
- [34] I. Ballesteros, J. M. Oliva, A. A. Navarro, A. González, J. Carasco, and M. Ballesteros, "Effect of chip size on steam explosion pretreatment of softwood," *Applied Biochemistry and Biotechnology—Part A: Enzyme Engineering and Biotechnology*, vol. 84–86, pp. 97–110, 2000.
- [35] H. Li and A. G. McDonald, "Fraction and characterization of industrial lignins," *Industrial Crops and Products*, vol. 62, pp. 67–76, 2014.